

# University of Southampton Research Repository ePrints Soton

Copyright © and Moral Rights for this thesis are retained by the author and/or other copyright owners. A copy can be downloaded for personal non-commercial research or study, without prior permission or charge. This thesis cannot be reproduced or quoted extensively from without first obtaining permission in writing from the copyright holder/s. The content must not be changed in any way or sold commercially in any format or medium without the formal permission of the copyright holders.

When referring to this work, full bibliographic details including the author, title, awarding institution and date of the thesis must be given e.g.

AUTHOR (year of submission) "Full thesis title", University of Southampton, name of the University School or Department, PhD Thesis, pagination

#### UNIVERSITY OF SOUTHAMPTON

## 

On the Prospect of Resonance Energy Transfer for Hybrid Optoelectronics

by

Jan Junis Rindermann

Thesis for the degree of Doctor of Philosophy

December 2012

#### UNIVERSITY OF SOUTHAMPTON

#### ABSTRACT

# FACULTY OF PHYSICAL AND APPLIED SCIENCES Physics and Astronomy

Doctor of Philosophy

# ON THE PROSPECT OF RESONANCE ENERGY TRANSFER FOR HYBRID OPTOELECTRONICS

by Jan Junis Rindermann

This work focuses on resonance energy transfer from excitons in QWs to absorptive media in the form of organic polymers or colloidal QDs. In view of the use of the latter as colour converters in LEDs it is demonstrated that the combination of the green-emitting polymer F8BT with blue-emitting InGaN/GaN QWs in a modified, commercially used LED wafer enables efficient energy transfer and achieves the desired emission of white light from the composite device. However, commercialisation of the scheme is prevented by the drastically degraded device performance. A detailed study of a GaN/AlGaN QW covered with F8BT reveals that the energy transfer dynamics in this material are dominated by point-like localised exciton states at temperatures up to 50 K and energetically higher lying free exciton states at room temperature. A model is presented to quantitatively explain the observation of the peak energy transfer efficiency at 43 K where localised and free excitons contribute equally to the thermalised exciton ensemble. The non-monotonous temperature dependence is directly related to the non-monotonous dependence of the energy transfer rate on the exciton wave vector which allows for some optimisation of the mechanism by creating increased populations of excitons with suitable wave vectors. These excitons achieve efficient energy transfer with capping layers that are tenfold thicker than the 4 nm thin capping layer studied here. This could be implemented by adjustment of the material purity or the density of states for specific wave vectors by the use of an imprinted grating. In an attempt to study the wave vector dependence explicitly transient grating spectroscopy is performed on a GaAs QW covered with an absorptive layer of PbS QDs. An effect of energy transfer on the diffracted signal is not observed because of the nearly instantaneous thermalisation of the exciton ensemble. Finally, energy transfer is simulated in the reverse configuration, i.e. from PbS QDs to a slab of bulk silicon separated by a spacer layer of variable thickness. In agreement with recent experimental results on this material combination, energy transfer breakes down for spacer layers as thin as 10 nm. Thus, the energy transfer scheme is neither viable for LEDs nor sensitised silicon solar cells.

## **Declaration of Authorship**

I, Jan Junis Rindermann, declare that the thesis entitled On the Prospect of Resonance Energy Transfer for Hybrid Optoelectronics and the work presented in the thesis are both my own, and have been generated by me as the result of my own original research. I confirm that:

- this work was done wholly or mainly while in candidature for a research degree at this University;
- where any part of this thesis has previously been submitted for a degree or any other qualification at this University or any other institution, this has been clearly stated;
- where I have consulted the published work of others, this is always clearly attributed;
- where I have quoted from the work of others, the source is always given. With the exception of such quotations, this thesis is entirely my own work;
- I have acknowledged all main sources of help;
- where the thesis is based on work done by myself jointly with others, I have made clear exactly what was done by others and what I have contributed myself;
- parts of this work have been published as: [1] and [2]

Signed:	 	 
Doto		

# List of Publications

#### Publications within the scope of this work

- J. J. RINDERMANN, G. POZINA, B. MONEMAR, L. HULTMAN, H. AMANO, AND P. G. LAGOUDAKIS, Dependence of resonance energy transfer on exciton dimensionality, *Physical Review Letters* **107**, 236805 (2011).
- J. J. Rindermann, G. Pozina, B. Monemar, L. Hultman, H. Amano, and P. G. Lagoudakis, The effect of exciton dimensionality on resonance energy transfer: advances for organic color converters in hybrid inorganic/organic LEDs, in: B. Witzigmann, M. Osinski, F. Henneberger, and Y. Arakawa (editors), *Proc. Spie, Physics and Simulation of Optoelectronic Devices XX*, volume 8255, Spie-Int. Soc. Optical Engineering, Bellingham (2012).

## Publications beyond the scope of this work

- J. J. RINDERMANN, Y. AKHTMAN, J. RICHARDSON, T. BROWN, AND P. G. LAGOUDAKIS, Gauging the flexibility of fluorescent markers for the interpretation of fluorescence resonance energy transfer, *Journal of the American Chemical Society* 133, 279 (2011).
- J. J. RINDERMANN, M. HENINI, AND P. G. LAGOUDAKIS, In-situ electrical characterisation of a photodiode during nano-structuring with a focussed ion beam, *Applied Physics A* **110**, 935 (2012).

#### Acknowledgements

I am indebted to the Reiner Lemoine Stiftung which has generously funded my postgraduate studies. At the same time, I am thankful for the support that I received from my supervisor Prof. Pavlos Lagoudakis who has given me access to the excellent facilities in the Laboratories of Hybrid Optoelectronics and who has enabled me to present my research at numerous conferences. From him I have learnt to advertise the results of my work. Over the years, but especially during the intensive work on the transient grating experiment, my colleague Dr. Chunyong Li has shown me that delicate and challenging experiments will eventually progress when they are approached with seemingly endless patience. Similarly, my friend and colleague Peristera Andreakou demonstrated that endurance together with tolerance can overcome the greatest obstacles. Among the many collaborators that I had the benefit to work with Prof. Bo Monemar stands out with the ability to provide immediate and razor-sharp feedback from afar, sometimes within minutes. In and outside the labs I have spent a great time with my colleagues and friends from the LHO group and I am thankful for that. Over the years, I could always be sure of the unconditional support from my family, and from Elena.

# Contents

A	bstra	act Control of the Co	j
$\mathbf{D}$	eclar	ation of Authorship	ii
Li	st of	Publications	iii
A	ckno	wledgements	iv
1	Inti	roduction	1
	1.1	Motivation	1
	1.2	Energy savings with LEDs	2
	1.3	Hybrid optoelectronics for efficient white LEDs	4
	1.4	Structure of this thesis	5
2	The	eoretical Background	7
	2.1	Bulk inorganic semiconductors	7
	2.2	Optical transitions	9
	2.3	Organic semiconductors	10
	2.4	Low dimensional semiconductors	11
		2.4.1 Quantum wells	11
		2.4.2 Colloidal quantum dots	12
	2.5	Excitons	13
		2.5.1 Wannier Mott excitons	13
		2.5.2 Frenkel excitons	13
	2.6	Resonance energy transfer	14
		2.6.1 Definition	14
		2.6.2 Resonance energy transfer between point dipoles	14
		2.6.3 Resonance energy transfer in arbitrary geometries	15
	2.7	Light emitting diodes	16
	2.8	Photovoltaic cells	18
3	Hyl	orid InGaN/F8BT light emitting diodes	20
	3.1	Previous work	20
	3.2	Materials and methods	21
		3.2.1 Different generations of GaN/InGaN multiple quantum well wafers	21

**Contents** Contents

		3.2.2	The polyfluorene F8BT	23
		3.2.3	Optical characterisation	
		3.2.4	Electrical characterisation	
	3.3	Result	ts and discussion	
		3.3.1	Effect of etching and surface passivation on the photoluminescence	
			lifetime	30
		3.3.2	Quenching of energy transfer at high excitation densities	
		3.3.3	Increased colour conversion due to resonance energy transfer	
		3.3.4	White light emission	
		3.3.5	Shortcomings of the third generation of LED wafers	
	3.4	Concl	usions	
4	Der	oenden	ace of Resonance Energy Transfer on Exciton Dimensionality	40
	4.1		rials and methods	
		4.1.1	Material system	
		4.1.2	Characterisation of energy transfer with time resolved spectroscopy	
	4.2	Reson	ance energy transfer dynamics of quantum well excitons	
		4.2.1	Free excitons	
		4.2.2	Localized excitons	
		4.2.3	Energy transfer in the exciton ensemble	
		4.2.4	Comparison between experiment and simulation	
		4.2.5	Comparison of radiative and non-radiative energy transfer	
	4.3	Optin	nization of resonance energy transfer	
	4.4	_	usions	
	4.5	The a	uthor's contribution	55
5	Dep	oenden	ace of Resonance Energy Transfer on Exciton Wave Vector	56
	5.1		rials and methods	56
		5.1.1	Single AlGaAs/GaAs quantum well	56
		5.1.2	PbS quantum dots	57
		5.1.3	Pump-probe reflection technique	57
		5.1.4	Transient grating spectroscopy	59
		5.1.5	Effect of energy transfer on the FWM signal	62
		5.1.6	Wave vector and time resolved photoluminescence	63
		5.1.7	Angle resolved pump probe technique	63
		5.1.8	Comparison of the different techniques	64
	5.2	Result	ts and discussion	66
		5.2.1	Evidence for energy transfer in the exciton ensemble	66
		5.2.2	Determination of the ambipolar diffusion coefficient	68
		5.2.3	FWM signal with and without energy transfer for different grating	
			periods	70
		5.2.4	Wave vector resolved photoluminescence	73
	5.3	Concl	usions	76
	5.4	The a	uthor's contribution	76
6	Res	onanc	e Energy Transfer from PbS Quantum Dots to Silicon	77
	6.1		ground	
		6.1.1	An earlier paper by Dexter	78

**Contents** Contents

		2 Quenching of a dipole in close vicinity of a semiconductor 78		
	6.1.3 Experimental demonstrations of energy transfer to a semiconducto			
		6.1.4 Work towards a sensitised silicon solar cell	81	
6.2 Methods			82	
		6.2.1 Definition of the problem	82	
		6.2.2 Finite element analysis	83	
	6.3	Results and discussion	84	
	6.4	Conclusions	85	
7 Conclusions and Future Work		nclusions and Future Work	87	
	7.1	Conclusions	87	
	7.2	Future work	89	
$\mathbf{R}$	efere	nces	90	

# List of Figures

1.1	Atmospheric concentrations and effects of important long-lived greenhouse gases	2
1.2	Development of the luminous flux per package and lamp purchase price per lumen of LEDs in comparison with incandescent tungsten-filament	
	light bulbs.	4
2.1	Electronic band structure of Si and GaAs	8
2.2	Chemical formula of benzene and two variants of F8BT	10
2.3	Density of states in semiconductors with different degrees of freedom for electron motion.	12
2.4	Emission spectrum of a LED with a bulk junction	17
2.5	Efficiency increase in multi junction solar cells	19
3.1	Schematics of the shallow and deep etched LEDs with QDs in the holes of the photonic crystal	21
3.2	Comparison of the different hole patterns on different generations of LED wafers	22
3.3	Spectral overlap between LED emission and F8BT absorption	24
3.4	Screenshot of the ColorimetryLab program written in Igor Pro	25
3.5		28
3.6	Colour filtered images of the LED wafer covered with F8BT	29
3.7	Effect of surface passivation and deep etching on the photoluminescence decay of the QWs	30
3.8	Power dependence of the time resolved photoluminescence of the QW before and after addition of F8BT.	33
3.9	Colour conversion in the deep and shallow etched LED covered with the	96
3.9		34
3.10	Back transfer of electrons from the polyfluorene to the InGaN QW	36
3.11	White light emission from the shallow and deep etched LEDs covered with a layer of F8BT in a PMMA matrix	37
3.12		38
4.1	Hybrid inorganic-organic material system for a hybrid LED employing resonance energy transfer	41
4.2	Evidence for resonance energy transfer in the photoluminescence from the	
		43

List of Figures List of Figures

4.3	Dependence of the energy transfer rate on the exciton wave vector	46
4.4	Schematic of the potential landscape experienced by excitons in an im-	
	perfect QW	47
4.5	Dependence of the energy transfer rate on the exciton localisation length.	47
4.6	Distribution of excitonic states in the imperfect QW	48
4.7	Förster radii of QW excitons	52
4.8	Optimisation of resonance energy transfer through variation of the poten-	
	tial landscape	54
5.1	Pump probe reflection setup.	58
5.2	Transient grating setup	60
5.3	FWM vector diagram	61
5.4	Wave vector resolved photoluminescence setup with a streak camera	64
5.5	Range of exciton wave vectors accessible by different spectroscopy tech-	
	niques	65
5.6	Evidence for resonance energy transfer from excitons in the GaAs QW to	
	an overlayer of PbS QDs	66
5.7	Different contributions to the model function for the FWM signal	68
5.8	Determination of the ambipolar diffusion coefficient from transient grating	
	experiments	69
5.9	One exemplary full dataset used to determine the amplitude of the FWM	71
F 10	signal for different grating periods	71
5.10	Amplitude of the FWM signal for different resonant wave vectors	72
5.11	Time and wave vector resolved photoluminescence of the QW	74
	Time resolved photoluminescence of the QW	74
5.13	Photoluminescence decay rate of the QW exciton for different wave vectors.	75
6.1	Geometry of the scheme for energy transfer from a PbS QD to a silicon	
	slab	83
6.2	Simulated energy transfer rate for different thicknesses of the spacing layer.	84

# List of Tables



# Introduction

#### 1.1 Motivation

Over the last 250 years human activities have resulted in an ever increasing emission of green house gases into the earth's atmosphere where they cause substantial global warming. This is one of the conclusions from the Fourth Assessment Report of the International Panel on Climate Change (IPCC) from 2007 [3-6]. Two figures are presented therein to quantify this effect in terms of the increased heat uptake by the earth: the first, shown in Fig. 1.1(a), shows the sudden increase of the concentration of the major greenhouse gases carbon dioxide, methane and nitrous oxide in the atmosphere coinciding with the beginning of the industrial revolution. To parry any cynic conclusion about the short timespan covered on this graph it should be added that in the year 2005 the atmospheric concentrations of carbon dioxide and methane exceeded by far the range found over the last 650,000 years. The other figure, presented in Fig. 1.1(b), provides a detailed breakdown of the most important components contributing to radiative forcing between the years 1750 and 2005. Radiative forcing is the change in net irradiance by the entire planet, measured in W/m<sup>2</sup>. If the value is positive, the planet warms up. The production of green house gases in large quantities results in the net warming effect of all human activities since 1750 because in the atmosphere these gases absorb and reemit infrared radiation back to the earth. This contribution is driven by the burning of fossil fuels to generate electricity and heat and to serve transportation. Also agriculture and deforestation contribute substantially to radiative forcing. Consequently, the IPCC projected a rise of the mean global surface temperature during the 21st century between 1.1 and 2.9 °C for their lowest and between 2.4 and 6.4 °C for their highest green house gas emission scenario [6]. An analysis of the severe effects of global warming on our lives and ecosystems which are expected over the coming decades can be found in the publications of the IPCC. Among them are climate extremes which threaten substantial parts of the global population, their harvest and livestock [7]. A systemic analysis also reveals

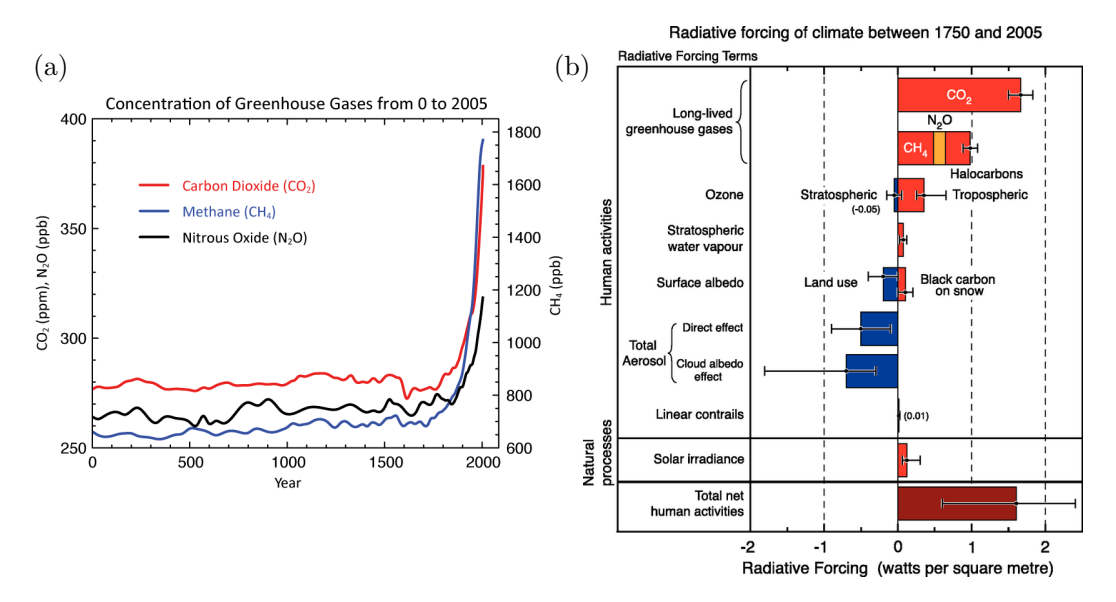


**Figure 1.1** – Atmospheric concentrations and effects of important long-lived greenhouse gases. (a) Atmospheric concentration over the last 2000 years. (b) Summary of the principal components of the radiative forcing of climate change due to human activities since 1750. Both figures from the FAQ section of Ref. [3].

feedback effects that have to be considered [5, 7]. Naturally, the reduction of green house gas emission is among the most important initiatives for the mitigation of climate change. The Kyoto Protocol from 1997 to the United Nations Framework Convention on Climate Change sets binding obligations on the industrialised nations to reduce their emission of greenhouse gases. To date, the US is the only industrialised nation which has not ratified the protocol, while Canada has renounced it in 2011. In its current form the protocol terminated in 2012. A discussion of the future and effectiveness of the protocol is beyond the scope of this thesis and can be found elsewhere.

## 1.2 Energy savings with LEDs

This work relates to energy saving in the field of lighting by the use of light emitting diodes (LEDs) instead of other established light sources, for example incandescent light bulbs. Roughly one third of the global energy consumption is spent for the generation of electricity, which to 68 % is generated by burning of fossil fuels [8, 9]. Currently, lighting alone consumes 20 % of that electricity. Brown estimates a saving potential of 65 % for the global lighting sector by 2020 [10]. This can potentially be achieved by the use of efficient light sources such as fluorescent sources, high intensity discharge sources and LEDs as well as energy efficient lighting schedules. The US Ministry of Energy expects more moderate savings for the US [11]. For the lighting sector they estimate electricity savings of nearly one half by 2030 with the use of the increasingly efficient solid state lighting (SSL) technology in comparison with a scenario without SSL. The authors employed an econometric logit model that predicts the acceptance and market

penetration of energy saving lighting technologies based on the value that customers receive. The currently projected industry goals for the performance of future generation of LEDs by far exceed the potential of the already established light sources. Not only does their study show what substantial energy savings can be achieved in the lighting sector. The key finding is that consumers will likely choose LEDs in favour of other alternatives because they are more energy efficient and provide high quality of light at the same time. The high efficiency of LEDs is indicated in table 1.1. By consideration of

**Table 1.1** – Luminous efficiencies of different light sources. (a) Incandescent sources. (b) Fluorescent sources. (c) High-intensity discharge (HID) sources. (d) LED sources. The luminous efficiency is an important figure of merit for visible-spectrum sources. It measures the *perceived* light power normalised to the electrical power expended to operate the light source. Table from Ref. [12]. \*World R&D performance record as of April 2012 [13].

Light source		Luminous efficiency
Edison's first light bulb (with C filament)	(a)	1.4  lm/W
Tungsten filament light bulbs	(a)	15-20  lm/W
Quartz halogen light bulbs	(a)	20-25  lm/W
Fluorescent light tubes and compact bulbs	(b)	50-80  lm/W
Mercury vapor light bulbs	(c)	50-60  lm/W
Metal halide light bulbs	(c)	80-125  lm/W
High-pressure sodium vapour light bulbs	(c)	$100-140 \; \text{lm/W}$
Current world record white LED*	(d)	254  lm/W

the light sources at his own home the reader may convince himself that the second criteria is indeed crucial and limits the acceptance of energy efficient light sources despite their evident economical advantage. Under no circumstances can the predictions for the US lighting sector be generalised for the whole world. One in three people obtain light from burning kerosene or other fuels and the associated primary energy costs represent 20% of the global costs for lighting [14]. However, it could be argued that the predictions for the US market can be transferred to the European Union, if not other regions with large markets and a high development index. The European Union's favour for regulative influence might lead to an even faster development. Legislations in many countries around the world have scheduled a phase out of incandescent light bulbs or have banned them already because of their inferior performance in comparison with energy saving technologies. This certainly accelerates the market penetration of new LED technologies.

Modern, high efficiency LEDs have now entered the general daylight illumination market and the market for packaged LED has surpassed \$10 bn in 2012 [15, 16]. They are rightfully marketed as the technologically prime energy saving alternative to conventional incandescent light sources. Among the advantages of LEDs are their lower power consumption and longevity (see again Tab. 1.1). Because of their high efficiency they are already an economical alternative to incandescent light bulbs, despite their

currently higher manufacturing costs. The promising development of LED pricing and performance can be seen in Fig. 1.2.

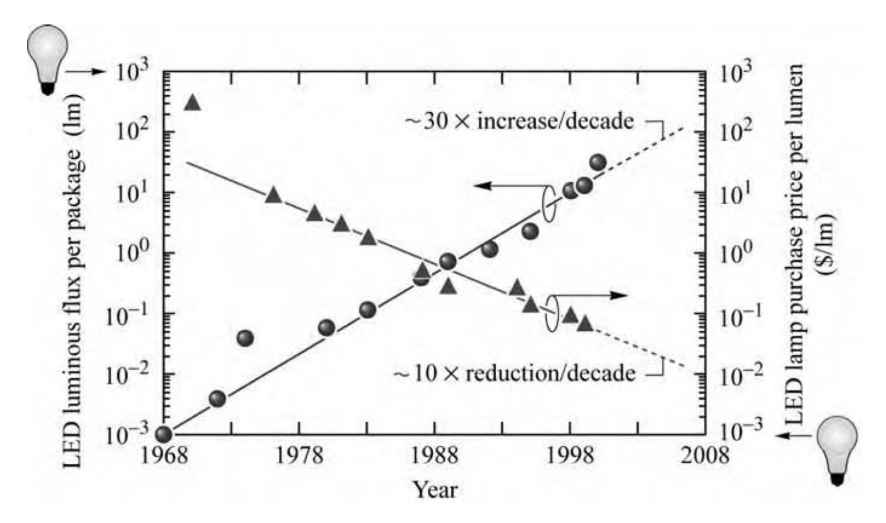


Figure 1.2 – Development of the luminous flux per package and lamp purchase price per lumen of LEDs in comparison with an incandescent tungsten-filament light bulb of 60 W. The graph shows the evolution over more than 4 decades. The reference light bulb has a luminous efficiency of 17 lm/W and a luminous flux of 1000 lm. Source: Ref. [12].

## 1.3 Hybrid optoelectronics for efficient white LEDs

LEDs are inherently monochromatic light sources, thus white light emission from LEDs is a technical challenge. Several approaches to white light illumination with LEDs exist [12]: multi coloured emission can be achieved from an epitaxially grown stack of multiple LEDs of different band gaps. Similarly, colour tuned semiconductors can be stacked on a LED as colour converters. However, the required epitaxial growth is not cost effective for mass production, and current state of the art white LEDs follow a different route: they utilise a layer of yttrium aluminum garnets doped with rare-earth compounds as a colour converter for high energy photons emitted by a quantum well (QW) LED based on group III nitrides. The rare-earth compounds are optically active in the visible region and absorb (partly) the light from the underlying LED. They feature broad emission spectra which yield white emission when combined with an appropriate blue or UV pump LED. Advances in the field of organic LEDs, organic photovoltaics and in the chemical synthesis of colloidal inorganic nano-particles resulted in new materials like fluorescent polymers and colloidal quantum dots (QDs) with tuneable emission properties throughout the visible region of the spectrum. In contrast to the rare-earth materials, which are becoming increasingly scarce, fluorescent polymers and QDs can easily be mass produced at low costs [17–19]. A new generation of hybrid optoelectronic devices combines inorganic semiconductors with organic materials or colloidal QDs. They merge the superior electrical properties of inorganic crystals with the high photoluminescence Chapter 1 Structure of this thesis

yield across the visible spectrum that can be found in organic materials or QDs. It has been demonstrated that in principal these materials can be employed as highly efficient colour converters on top of UV or blue-emitting LEDs, similar to the rare-earth doped YAGs [1, 20–26]. However, the use of organic materials and quantum dots for hybrid optoelectronics beyond colour conversion is fundamentally limited by their low charge injection and transport in comparison with their inorganic counterparts. Based on theoretical considerations, Agranovich proposed to transfer electronic excitations from an inorganic QW to an absorptive organic material in close proximity without the need for electrical connectivity and without optical pumping [27–31]. Accordingly, electron-hole excitations are transferred via dipolar coupling from one material to the other, effectively converting the nature of the exciton. This resonant energy transfer (RET) from inorganic QWs to organic layers (or layers of QDs) has been demonstrated for a wide range of material combinations, many of which are relevant for the application of this scheme to pump the colour converter in a hybrid LED that embeds organic materials for colour conversion [1, 20-26, 32, 33]. In one study it was demonstrated that the characteristic absorption and emission properties of J-aggregates and QDs can be arbitrarily combined in a hybrid material stack when excitations are efficiently transferred from one species to the other via RET [34]. Agranovich recently prepared a complete review of all applications of RET for hybrid optoelectronics [35].

Given the combination of great optical properties and poor electrical properties of QDs and organic layers, is resonance energy transfer the key to integrate these materials into optoelectronics devices like LEDs and solar cells? Especially in closely packed planar geometries, like they are found in LEDs, non-radiative RET has been demonstrated to be orders of magnitude more efficient than the commonly employed radiative energy transfer, i.e. absorption and re-emission of light by the colour converter [1, 20, 25]. An answer will be given in the following.

#### 1.4 Structure of this thesis

This thesis presents a detailed study of the resonant transfer of excitons from inorganic QWs to organic layers and layers of QDs. In chapter 2 the most relevant principles and mechanisms in hybrid inorganic-organic structures will be explained as part of an extended introduction. The work from chapter 3 is application driven and deals with an exemplary implementation of an organic colour converter in combination with the resonant energy transfer scheme on a LED wafer supplied by a LED manufacturer. In chapter 4 the theory of energy transfer from QW excitons will be reviewed and extended for thermalised ensembles of excitons. The considerations made therein in combination with the presented experimental evidence allows to make conclusions about the optimisation of energy transfer in such planar geometries. What follows in chapter 5 is a very thorough attempt to provide direct experimental evidence for the theoretically

Chapter 1 Structure of this thesis

expected non-monotonous dependence of resonance energy transfer on the wave vector of the QW exciton. This chapter will likely appeal to a reader with an interest in spectroscopy techniques because the experiments follow closely the work on transient grating spectroscopy from the 1980s while benefitting from modern femtosecond laser sources. The last chapter (6) is devoted to an old idea by Dexter (1979) who proposed to bring into play a strongly absorbing organic dye to sensitise a silicon solar cell by the use of energy transfer from the former to the latter [36]. A review of the existing experimental evidence in this field is followed by the discussion of the results from a finite element simulation of the scheme and recent experiments on the subject. The thesis closes with conclusions about the potential of optoelectronics based on resonance energy transfer.



# Theoretical Background

#### 2.1 Bulk inorganic semiconductors

The central topic of study in this thesis is resonance energy transfer, a process which occurs via the coupling between dipole transition moments in different semiconducting materials. Hence, the natural starting point for the introduction to the mechanism is the origin of optical transitions in semiconductors. When individual atoms are combined to form a crystalline solid the resulting material can be generally classified to be either an insulator, conductor or semiconductor. The two former are characterised by their property to be either inhibiting or promoting the transport of electrons, whereas the conductivity of semiconductors can be manipulated to vary over several orders of magnitude by doping their crystalline structure with impurity atoms or by variation of the temperature. This is a consequence of their characteristic band gap, a range of energies for which no electronic states exist in the material. In the case of semiconductors this energy gap lies between the filled and unfilled states constituting the valence and conduction band. These bands describe the energy-momentum relation for electrons inside the crystalline semiconductor and they are the equivalent of the dispersion relation for a free electron in vacuum. The existence of continuous bands can be understood by considering the hybridisation of electronic states when two atoms are brought in close proximity: two equivalent electronic states hybridise into a bonding and anti-bonding state. Similarly, when a (nearly) infinite number of atoms is brought together to form a crystal their discrete energy levels hybridise into two energy bands which might or might not overlap and which determine the electronic properties of the material. Moreover, the lattice can be purposely or unintentionally doped by atoms that contribute more or less electrons than the atoms of the host lattice. In this case the semiconductor becomes n or p doped, respectively. Additional (or absent) electrons may contribute substantially to charge transport in the semiconductor and effectively render it a conductor. The motion of electrons through the semiconductor is described by their momentum  $\mathbf{p} = \hbar \mathbf{k}$ ,

where  ${\bf k}$  is the wave vector. As a consequence of the periodicity of the crystal lattice the energy-wave vector dispersion relation is periodical in the wave vector and can be folded back into the so called Brillouin zone, the wave vector equivalent of a primitive cell in the crystal lattice. More specifically, the *Bloch Theorem* states that the wavefunction of the electron is periodic in space and wave vector and can be separated into a products of two parts, one that accounts for the crystal potential and one in the form of a propagating wave. It can be shown that for many problems it suffices to consider only an envelope function composed of plane waves, and neglect the fast oscillating part of the wave function that accounts for the crystal potential. Different approximate approaches to calculate the band structure of semiconductors lead to the result that near the extrema of the energy bands the dependence of the energy on the wave vector is quadratic like it is the case for a free electron in vacuum. The curvature of the dispersion then defines an important parameter of the semiconductor, the *effective mass* of the electron. Figure 2.1 shows the band structure of GaAs and Si, two of the best studied semiconductors. The figure also shows the degeneracy of the valence bands at  ${\bf k}=0$  that is

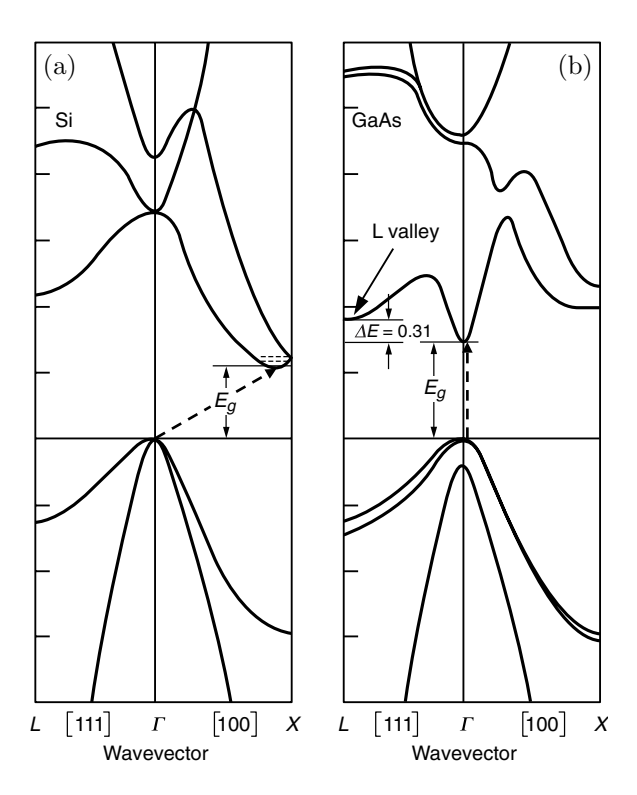


Figure 2.1 – Electronic band structure of Si (a) and GaAs (b). The dashed arrows indicate optical interband transitions. In the case of a non-vertical transition in the indirect semiconductor Si a phonon contributes or absorbs the required momentum. Figure modified from Ref. 37.

found in most semiconducting materials. It originates from the predominantly triplet nature of the  $sp^3$  atomic orbitals that form the valence band. The different curvature of the bands results in different effective masses. In a *bulk* semiconductor the density of states (DOS), including different spin states, along the parabolic part of the dispersion

Chapter 2 Optical transitions

is given by

$$DOS_{3D}(E) = \frac{V}{2\pi^2} \left(\frac{2m_c}{\hbar^2}\right)^{\frac{3}{2}} \sqrt{E - E_c},$$
(2.1)

where V is the volume of the crystal,  $m_c$  the effective mass of the electron in the conduction band and  $E_c$  the energy at the edge of the conduction band. A more thorough introduction to solid states physics can be found in Refs. 38, 39.

## 2.2 Optical transitions

The existence of a band gap implies that in a semiconductor electrons have to acquire at least the energy corresponding to the band gap  $E_{gap}$  in order to be promoted from the valence to the conduction band. At elevated temperatures this energy can be supplied during thermal collisions with other carriers, but more relevant for this study are transitions where the interaction with a photon causes an interband transition. Interactions with photons can also result in transitions within one band, intraband transitions. These will not be discussed here. Because the photon's wave vector  $|\mathbf{k}_{opt}| = \hbar/2\pi$  is so small in comparison with the electron's wave vector optical transitions occur effectively at constant  $\mathbf{k}$ . We will now constrain the discussion to interband transitions in direct semiconductors, i.e. materials where the maximum of the valence band aligns at  $\mathbf{k} = 0$  with the minimum of the conduction band. The coupling between the photon and the electron can be described in terms of a transition dipole moment which is a measure for the probability that an electron subject to an electromagnetic wave is promoted to another band. The matrix element for the dipolar interaction is given by

$$W_{v,c}(\mathbf{k}) = -q\mathbf{E} \cdot \mathbf{r}_{v,c} \delta(\mathbf{k}' - \mathbf{k}_{opt} - \mathbf{k}), \tag{2.2}$$

where q is the charge of the electron,  $\mathbf{E}$  the electric field of the electromagnetic wave,  $\mathbf{k}$  and  $\mathbf{k}'$  are the wave vector before and after the interaction. The factor  $\mathbf{r}_{v,c}$  is defined as  $\mathbf{r}_{v,c} = \langle u_{c,\mathbf{k}} | \mathbf{r} | u_{v,\mathbf{k}} \rangle$ , where u denotes the fast oscillating part of the wavefunction for a specific band and wave vector. In indirect semiconductors the band extrema do not align at the same wave vector and a transition at the band edge requires the interaction with a phonon, a quantised vibration of the crystal lattice, to compensate the difference in wave vector. Direct and indirect transitions are indicated as dashed arrows in the band structures shown in Fig. 2.1. Kane's  $\mathbf{k} \cdot \mathbf{p}$  method is a theoretical procedure to calculate the band structure of semiconductors from parameters that can be obtained in optical experiments. Accordingly, the dipole matrix element is to first order in  $\mathbf{k}$  constant and the factor  $\mathbf{r}_{v,c}$  can be approximated and expressed using the Kane energy  $E_{\mathbf{P}}[37, 40]$ :

$$|\mathbf{r}_{\text{v,c}}| = \frac{\hbar}{E_{\text{gap}}} \sqrt{\frac{E_{\text{P}}}{2m_0}},\tag{2.3}$$

where  $m_0$  is the free electron mass and  $E_{gap}$  is the band gap. This relation is used in chapter 4 to quantitatively calculate the rate of resonance energy transfer for a given material system. The underlying theory of resonance energy transfer will be briefly outlined at the end of this chapter.

When an electron undergoes a transition from the valence to the conduction band it leaves behind an unoccupied electronic state. It can be shown that all remaining electrons in the valence band collectively behave as if they were a single charge carrier of opposite spin, opposite charge and opposite momentum to the deficient electron and with a new effective mass. The result is the description of the vacant state in terms of the quasi particle named *hole*. When an electron undergoes a transition back from the conduction to the valence band where it fills a vacant state it is said that it recombines with a hole.

## 2.3 Organic semiconductors

In conjugated organic molecules the constituting carbon atoms promote one of their 6 electrons from the 2s-shell to the otherwise unfilled  $2p_z$ -shell and subsequently hybridisation between the remaining 2s-shell and the now filled 2p-shell occurs. The resulting  $sp_1$ ,  $sp_2$  or  $sp_3$  hybrid orbitals contribute in total 4 electrons to bind with other atoms. Possible binding combinations are a strong  $\sigma$ -bond when two sp-orbitals overlap or a  $\pi$ -bond when two remaining p-orbitals overlap. When both types of binding orbitals overlap together the resulting carbon double bond is rather weak and yields one delocalised electron. A typical example is found in the benzene ring ( $C_6H_6$ , shown in Fig. 2.2(a)) where it is not possible to assign a particular location to the  $\pi$ -electrons constituting the double bonds. In some conjugated molecules this delocalisation bears

(a) (b) (C) 
$$H_3C$$
 (C)  $H_3C$  (C

Figure 2.2 – Chemical formula of benzene and two variants of the polyfluorene F8BT. (a) The two possible conformations of the benzene ring with delocalised electrons from the  $\pi$ -bonds. (b) F8BT variant that absorbs around 460 nm: Poly(9,9-dioctylfluorene-alt-benzothiadiazole). (c) F8BT variant that absorbs around 375 nm: Poly(9,9-dioctylfluorene-co-benzothiadiazole). Both variants feature a broad emission spectrum in the green-yellow spectral region.

similarities with the delocalisation of electrons in the crystal lattice of a semiconductor. Accordingly, the highest occupied molecular orbital (HOMO) is filled up by electrons from strong  $\sigma$ -bonds whereas the lowest unoccupied molecular orbital (LUMO) is a delocalised electronic state from a  $\pi$ -electron cloud. Similar to their inorganic counterparts, conjugated molecules are considered to be *semiconducting* when their band gap, i.e. the difference between the HOMO and LUMO levels, corresponds to a photon from the visible range of the electromagnetic spectrum. This is the case for the polymer Poly(9,9dioctylfluorene-benzothiadiazole) (F8BT) that is used in two studies for this thesis as an acceptor in excitonic energy transfer for the purpose of colour conversion in hybrid inorganic-organic LEDs. The chemical formulae of two variations of the F8BT polymer are shown in Fig. 2.2. Below the HOMO and above the LUMO levels the energy states remain discrete in contrast to the continuous states in an inorganic semiconductor and in some molecules it is possible to assign the electronic levels to specific subgroups. Discrete vibrational states contribute further to the discrete character of the energy levels in organic semiconductors and effectively broaden their emission and absorption spectrum around a particular electronic transition.

#### 2.4 Low dimensional semiconductors

So far our considerations on semiconductors covered bulk crystals where the ordered assembly of atoms approaches infinite dimensions in comparison with all relevant length scales. However, it is possible to grow crystals with heterojunctions between different semiconductors. When doing so the main concern is the matching of the lattice constants, otherwise the crystal will be strained where the two materials merge, resulting in dislocations in the lattice. At the heterojunction the band edges of the two materials align depending on their electron affinity. In the case of a straddling heterojunction the energy gap of one material lies within the energy gap of the other and electrons as well as holes experience a potential barrier relative to the material with the lower band gap.

#### 2.4.1 Quantum wells

In quantum wells (QWs) electrons and holes are trapped between two straddling heterojunctions. When the thickness of the inner material is only a few nanometres and on the order of the de Broglie wavelength of the electron,  $\lambda = h/\sqrt{2m_cE}$  with the effective mass  $m_c$ , the problem resembles that of a particle in a box, where quantised energy states evolve as a consequence of quantum confinement in one direction. Exact and approximate solutions to the problem can be found in Refs. [37, 39, 41]. The motion of the electron in the other two directions remains unchanged and subbands emerge for each quantised energy level. Within each subband the density of states is constant and

the joint density of states has a step-like shape which is given by

$$DOS_{2D}(E) = \frac{Am_c}{\pi\hbar} \sum_n \Theta(E - E_n), \qquad (2.4)$$

where  $m_c$  denotes the effective mass in the well material, A the considered area of the QW,  $E_n$  the energy of the n-th subband and  $\Theta$  the unit step function. The same arguments apply to the hole states in the valence band. As a consequence of the quantum confinement the lowest interband transition in QWs lies at an energy above that of the bulk material. This offset can be adjusted by the bandgaps of the constituting materials and more importantly by the width of the QW. This tunability of the emission wavelength is one of the reasons why QWs are commonly used in LEDs, semiconductor lasers and other optoelectronic devices. It should be noted that due to the orthogonality of the wave functions for different subbands optical transitions are only allowed between electron and hole states with the same subband index.

#### 2.4.2 Colloidal quantum dots

When electrons and holes become confined in three dimensions one obtains so called quantum dots (QDs). This can be achieved by the application of an electrostatic potential in the plane of a QW, by epitaxially growing small islands of a semiconductor on a planar interface or by the wet-chemical synthesis of semiconductor nanocrystals which contain only a few hundred atoms and vary in size between a few nanometres and tens of nanometres. All these systems are called artificial atoms because of the delta function-like peaks in their density of states. Figure 2.3 shows the shape of the joint density of states in semiconductors with different degrees of quantum confinement. Evidence for the sharp spikes in the DOS for QDs can be found in low temperature absorption spectra.

Colloidal QDs have been successfully implemented as colour converters with size tuneable emission properties for light emitting diodes [1, 21, 24–26]. In chapters 3, 5 and 6 they are used as energy transfer acceptors and donors.

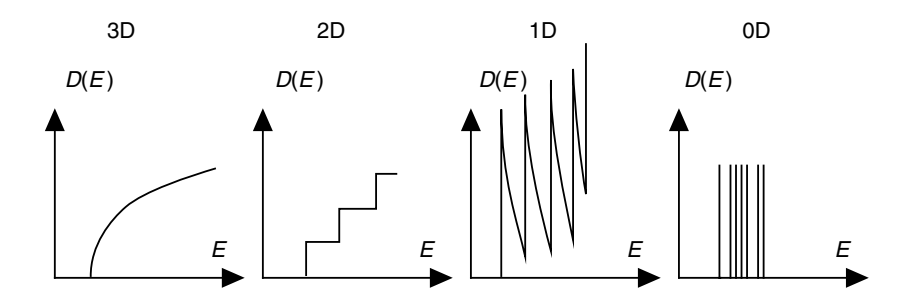


Figure 2.3 – Density of states in semiconductors with different degrees of freedom for electron motion. Units for DOS are  $eV^{-1}cm^{-D}$ , where D is the number of unconstrained dimensions.

Chapter 2 Excitons

#### 2.5 Excitons

#### 2.5.1 Wannier Mott excitons

A negatively charged electron in the conduction band and a positively charged hole in the valence band attract each other via coulombic interaction, analogue to the interaction of the electron and nucleus in the hydrogen atom. The interaction is reduced by the screening of the electric fields due to the high dielectric constant and large number of atoms in the crystal. As a consequence the bound two particle state extends over several lattice sites and propagates without allocation to a specific site freely through the crystal lattice. The resulting quasi particle is referred to as an Wannier Mott exciton [42]. As long as the temperature (measured in  $k_{\rm B}T$ ) is lower than the binding energy excitons contribute substantially to the electronic and optical properties of semiconductors because they constitute the lowest lying electronic excitation of the semiconductor. Excitons have a stronger dipole moment for the interaction with light because of the enhanced overlap of the electron and hole wavefunction. The underlying two body problem is conveniently solved in analogy with the hydrogen atom, yielding an exciton binding energy of

$$E_{\rm X,bind} = \frac{m_{\rm r}}{m_0} \frac{\epsilon_0^2}{\epsilon^2} E_{\rm Ryd}$$
 (2.5)

and an exciton Bohr radius of

$$a_{\rm X,B} = \frac{m_0}{m_{\rm r}} \frac{\epsilon_0}{\epsilon} a_{\rm B},\tag{2.6}$$

where  $m_{\rm r}^{-1} = m_{\rm e}^{-1} + m_{\rm h}^{-1}$  is the reduced mass determined from the effective electron and hole masses,  $m_0$  the free electron mass,  $\epsilon$  the relative permittivity of the semiconductor,  $\epsilon_0$  the vacuum permittivity,  $a_{\rm B}$  the Bohr radius and  $E_{\rm Ryd}$  the Rydberg energy with a value of 13.6 eV. In GaAs the exciton binding energy is 5.6 meV and the Bohr radius 10.6 nm. When the thickness of a quantum well becomes smaller than the exciton Bohr radius these expression need to be recomputed. Numerical methods can be found in Ref. [43]. In the limiting case of an infinitely thin QW the exciton becomes purely two-dimensional and the binding energy and Bohr radius are given by:

$$E_{X,\text{bind,2D}} = 4 \cdot E_{X,\text{bind}}$$
 (2.7)

$$a_{X,B,2D} = a_{X,B}/2$$
 (2.8)

#### 2.5.2 Frenkel excitons

In organic semiconductors or organic crystals the dielectric constant is small and an electron-hole excitation may occur on one individual molecule. In this case the binding energy is at least one order of magnitude larger than for Wannier Mott excitons and the Bohr radius does not exceed the size of the unit cell or the sub group of the molecule.

These strongly localised excitons are referred to as *Frenkel excitons* [44]. Due to the substantial spacial overlap of the electron and hole wave functions they posses a very high oscillator strength close to the molecular oscillator strength. This is the reason why organic semiconductors are desired building blocks for photonic devices like lasers, light emitting diodes or solar cells.

## 2.6 Resonance energy transfer

#### 2.6.1 Definition

The non-radiative, resonant transfer of electronic excitation energy between a donor and acceptor that is studied throughout this thesis originates from an interaction of the form

$$H_{\text{RET}} = -\mathbf{E} \cdot \mathbf{P}_{\mathbf{a}},\tag{2.9}$$

where  $\mathbf{E}$  denotes the electrostatic field produced by the oscillations of the electronic dipole polarisation of the donor and  $\mathbf{P}_{\rm a}$  is the polarisation of the acceptor. Because the process relies on the energetic alignment of electronic states in the donor and acceptor it is commonly called resonance energy transfer or, shorter, RET. The dipole-dipole coupling is the electrodynamic analogue of the coupling between two mechanical oscillators with similar frequencies connected by a spring. RET is a near field effect where the donor-acceptor distance is much smaller than the wavelength and retardation effects can be neglected. However, on the scale of the electronic wave functions we consider relatively long separations where the electronic wave functions do not overlap and RET is to be distinguished from another from of resonant energy transfer, namely Dexter energy transfer [45].

#### 2.6.2 Resonance energy transfer between point dipoles

Förster was the first who presented a quantitative description of the underlying process for the case of dipolar coupling as it can be found between pairs of molecules with broadened and overlapping emission and absorption spectra [46, 47]. The polarisation of the acceptor is subject to the well known electric field produced by the polarisation of the donor

$$\mathbf{E}(\mathbf{R}) = \frac{1}{4\pi\epsilon_0} \frac{1}{R^3} \left[ 3 \frac{(\mathbf{P}_d \cdot \mathbf{R}) \mathbf{R}}{R^2} - \mathbf{P}_d \right], \tag{2.10}$$

where  $\mathbf{R}$  is the vector connecting the two molecules and R is its magnitude. The rate of energy transfer is then given by

$$\Gamma_{\text{RET,d-d}}(R) = \Gamma_{\text{rad}} \left(\frac{R_0}{R}\right)^6,$$
(2.11)

where  $\Gamma_{\rm rad} = \frac{1}{\tau}$  is the radiative decay rate (the inverse of the fluorescence lifetime) of the donor molecule and  $R_0$  the so called Förster radius, a material parameter including the spectral overlap and donor quantum yield. It is usually on the order of a few nanometres.

The expression for the energy transfer rate between two point dipoles can be generalised to the case of energy transfer from one point dipole to an array of acceptor dipoles. In this case one obtains by spatial integration over the acceptor array

$$\Gamma_{\text{RET}}/\Gamma_{\text{r,vac}} = (R_0/d)^n$$
, (2.12)

where the power n is a function of the dimensionality of the array [48]. A line of acceptor yields n = 5, while a thin layer yields n = 4, and a volume of acceptors gives n = 3. It is important to keep in mind that Förster's theory and this subsequent consideration only holds for the interaction between *point-like* dipoles which are well enough approximated by the electronic excitation found in ions, dye molecules or (sufficiently small) QDs. Lunz et al. found good agreement between the theory and the results from their experimental realisation of energy transfer between QDs arranged in thin layers [49]. In chapter 4 it will be argued that an exciton in a QW cannot be represented as a point-like dipole and hence the distance dependence of the rate of energy transfer to an adjacent layer of organic material does not follow a power law like it was initially proposed [20].

#### 2.6.3 Resonance energy transfer in arbitrary geometries

The approach outlined above to calculate the energy transfer rate between two dipoles is invalid in the case of excitations that are spatially extended like Wannier Mott excitons in QWs. Theoretical work led by Agranovich and Basko has shown that the rate of resonance energy transfer in the weak coupling regime can nevertheless be calculated for arbitrary geometries equivalently either by treating excitonic energy transfer as Joule losses or by the fully quantum mechanical treatment of all electronic states in the system [28, 29, 31]. The criteria for the weak coupling regime are a fast acceptor relaxation time and a broad acceptor spectrum at the spectral region of the resonance. Here, we will reproduce the semi classical approach.

The electric field created by oscillations of the QW polarisation penetrates into an absorbing medium and dissipates energy by the excitation of electronic states. In the first step we note that the total transition dipole moment is replaced by the spatially dependent excitonic polarisation  $\mathbf{P}(\mathbf{r})$  that can be computed from the exciton wavefunction [39, 50]. The corresponding charge density is then given by

$$\rho(\mathbf{r}) = -\nabla \cdot \mathbf{P}(\mathbf{r}). \tag{2.13}$$

This step effectively reduces the problem to a typical electrostatic problem, where the Poisson equation can be employed to solve for the electric potential  $\phi(\mathbf{r})$  in the standard

formulation:

$$\mathbf{E}(\mathbf{r}) = -\nabla \phi(\mathbf{r}) \tag{2.14}$$

$$\nabla \cdot (\epsilon(\mathbf{r}) \nabla \phi(\mathbf{r})) = -\rho(\mathbf{r}) \tag{2.15}$$

Here,  $\epsilon(\mathbf{r})$  is the position dependent dielectric function that along with the exciton wavefunction accounts for the geometry of the configuration. In view of the chapters 3, 4 and 5 the reader may consider already a planar geometry where a QW is covered with some type of absorbing material. Now the problem can be be solved taking into consideration the appropriate boundary conditions for  $\phi(\mathbf{r})$  at all interfaces and at infinity. The result is the position dependent electric field  $\mathbf{E}(\mathbf{r})$  that is required to determine the Joule losses [51]. We only reproduce the expression for the power dissipated in an non-conducting, isotropic and absorbing medium with the dielectric function  $\epsilon(\omega) = \epsilon'(\omega) + i\epsilon''(\omega)$  [35]:

$$Q(\omega) = \frac{\omega \epsilon_0}{2} \int \epsilon''(\omega) |\mathbf{E}(\mathbf{r})|^2 d\mathbf{r}.$$
 (2.16)

This semiclassical approach conveniently allows to compute the energy transfer rate when only the macroscopic dielectric function (or tensor) of the absorbing medium is known. The equivalency of the semiclassical and microscopical quantum mechanical derivations are discussed in Ref. [29]. This reference also presents the explicit solution to the Poisson equation in the case of a planar geometry. The transfer time for an exciton of energy  $\hbar\omega_X$  in the QW to the absorbing medium is then given by the relationship:

$$\tau_{\text{RET}} = \frac{\hbar \omega_{\text{X}}}{Q(\omega_{\text{X}})}.$$
 (2.17)

## 2.7 Light emitting diodes

Light emitting diodes, short LEDs, are optoelectronic devices that emit light by electroluminescence when they are driven by an electric current. The colour of the emitted light
is mainly determined by the band gap of the optically active material in them. It can be
tuned to some extent by the use of QWs or doping with optically active impurities [12].
Since their first implementation in the 1960s as dim, red emitting indicators material
science and fabrication techniques have evolved further such that emission from LEDs
can now cover the spectrum from ultraviolet to infrared [12]. Especially their use as a
replacement for incandescent light sources allows huge energy savings along with costs
savings due to their high luminous efficiency., i.e. the ability to convert electrical power
into light that we can actually perceive. The performance of light sources is measured
taking into account the sensitivity curve of the human eye which peaks around 555 nm.
In the most basic configuration a LED consists of a pn-junction, i.e. a crystalline junction between a p and n-doped region of a semiconductor. When electrons and holes

are injected into the p and n-region by the use of metallic contacts they can recombine radiatively in the junction region, giving rise to electroluminescence. This process can be enhanced when QWs are incorporated into the junction region. Typical materials are GaAs, InGaN or GaN. The emission spectrum of a LED is governed by the density and occupation of electron and hole states in the conduction and valence bands. Under standard conditions the excess carrier density in a LED is low and the carrier distribution is well approximated with a Boltzmann distribution. Then we obtain the emission spectrum as the product between the density of states and the Boltzmann factor. In the case of a LED based on a bulk pn-junction we obtain  $I(E) \propto \sqrt{E - E_{gap}} \cdot e^{-E/(k_{\rm B}T)}$  as indicated in Fig. 2.4. The FWHM of the resulting spectrum is then

$$\Delta E = 1.8k_{\rm B}T$$
 or  $\Delta \lambda = \frac{1.8k_{\rm B}T\lambda^2}{hc}$ . (2.18)

When the active material is a QW, as it is commonly the case in commercial devices, the emission spectrum becomes narrower due to the step-like shape of the density of states. For the application in general lighting, where white light emission is desired,

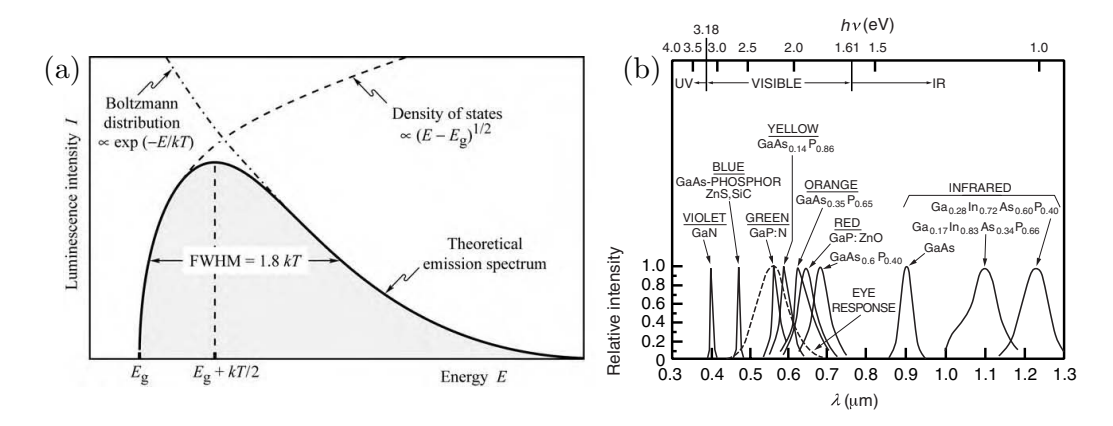


**Figure 2.4** – Emission spectrum of a LED with a bulk junction. (a) Theoretical spectrum. (b) Spectra from LEDs fabricated from different materials. Figures from Ref. 41.

LEDs bring inherent advantages and disadvantages in comparison with incandescent light sources: the spectrum of an incandescent light bulb resembles by definition very well that of a black body emitter. Thus, its correlated colour temperature (CRT), i.e. the temperature of the blackbody emitter that has the most similar emission colour, can easily be adjusted to yield the desired similarity with natural sun light. Due to the band gap specific emission wavelength a single LED cannot yield white light. Nevertheless, this can be achieved by the combination of several different LED chips in one device or in a monolithic implementation of a multi-chromatic device which embeds different QW stacks and a colour converting semiconductor layer. The third and economically most viable option is a ultraviolet or blue emitting LED which is covered with a colour converting, rare-earth doped garnet, most commonly in the form of a yttrium aluminium garnet (YAG). The material is deposited on top of the LED and (partially) absorbs the emitted ultraviolet or blue photons. Due to the complex energy structure of the rare

Chapter 2 Photovoltaic cells

earth ions the phosphor features a very broad emission spectra that in combination with the light from the LED yields "white" light. A brief introduction to the field of colorimetry, the methodology used to describe the colour of a light source, will be given in the next chapter. At last, it should be noted that the the external quantum efficiency of modern LEDs, i.e. the ratio between the injected electrons and the photons emitted into free space, regularly exceeds 70 %, thus allowing for noticeably higher power efficiencies (wall plug efficiencies) in comparison with incandescent light bulbs [17].

#### 2.8 Photovoltaic cells

Photovoltaic cells, also called solar cells, absorb incoming light and convert the photon energy to drive a current without being subject to a voltage. The simplest device constitutes again a single pn-junction with electrical contacts. When a photon is absorbed in the junction region the created electron and hole pair is separated by the electric field that is produced by the built-in potential between the differently doped regions. The charge separation on the opposite sides of the pn-junction is the driving force for an electrical current when the terminals of the device are connected to an electric load. Due to the absorption mechanism in the semiconductor the band gap of the chosen material determines the fraction of the (sun) light's spectrum that the device can possibly absorb. A material with a too small band gap, however, will absorb most of the incoming light, but at the price of a reduced built-in potential and a large amount of excess heat that is produced when highly energetic photons produce electrons and holes with energies high above the band gap. The band gap of silicon,  $E_{\rm gap,Si} = 1.1$  eV, is very close to the optimum value. For this reason and due to its abundance it is the most commonly employed material for large scale photovoltaic installations, despite its poor absorption coefficient originating from its indirect band gap. The theoretical upper boundary for the energy conversion efficiency of a pn-junction cell is determined by the Shockley-Queisser limit, the result of a detailed consideration of Blackbody radiation, carrier recombination and spectral losses in such a device subject to the sun's radiation [52]. The state of the art, best performing mono-crystalline silicon solar cell has an efficiency of 27.6 % under laboratory conditions in comparison with the Shockley-Queisser limit of 33.7 % [53]. More complex configurations employ up to three stacked junctions on top of each other and yield efficiencies of 43.5 %. For triple junction cells the Shockley-Queisser limit is 49 % and for an imaginary cell with an infinitely high number of stacked junctions with gradually changing band gaps it is 68 %. This trend is indicated in Fig. 2.5. Due to the abundance of silicon on the surface of the earth it seems to be the material of choice for the large scale employment of photovoltaic power as a means to reduce carbon emissions from burning fossil energies or to reduce nuclear waste. In addition to the aforementioned mono-crystalline silicon cell other, amorphous, or thin film, architectures have been demonstrated [55]. The major difficulty connected with the use of silicon is the low

Chapter 2 Photovoltaic cells

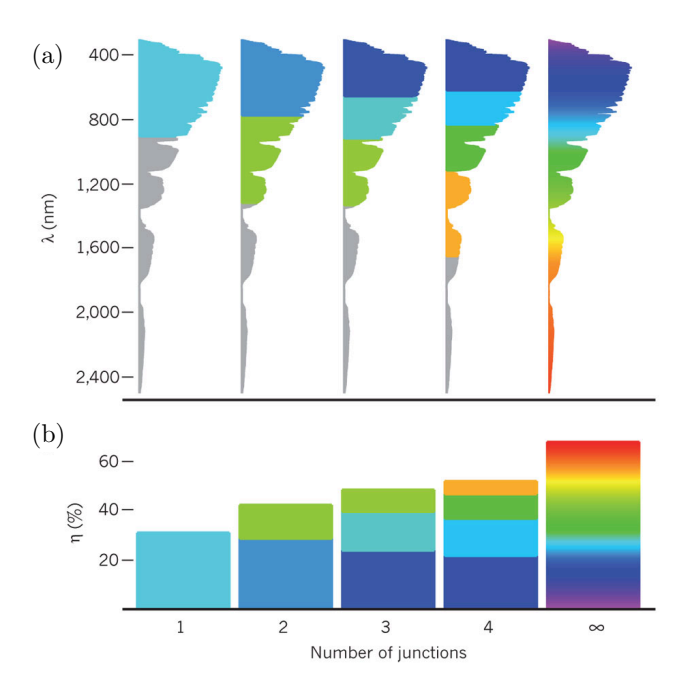


**Figure 2.5** – Efficiency increase in multi junction solar cells. (a) Fraction of the solar spectrum that is harvested by junctions of different band gaps. (b) Theoretical efficiency of multi junction devices. Figure from 54.

absorption coefficient. As indicated in the introduction it has been proposed to equip poorly absorbing silicon cells with a layer of a highly absorbing organic dye [36]. The dye molecule (or colloidal QD) absorbs photons more efficiently and can transfer the electronic excitation energy to the underlying silicon cell by virtue of resonance energy transfer. The exciton created in the silicon in this way is subsequently separated by the electric field in the junction region and converted into electrical energy. In chapter 6 we will present the results of a computational study on the characteristic distance at which resonance energy transfer from colloidal QDs to silicon breaks down due to the near field nature of the process.

Currently, the largest contribution to the material costs of a silicon solar cells results from the silicon itself. The cells have a thickness of several hundred micrometers because of the long absorption length in the material. New concepts of thin film devices, only a few hundred nanometers thin and made of amorphous silicon or other materials, will employ nanoplasmonics and better antireflection coatings to increase the absorption of light [55]. Such devices might also benefit from energy transfer pumping because by virtue of being thin a sensitising layer on the top moves closer to the depletion zone of the cell, increasing the effectiveness of energy transfer. A similar argument holds for organic photovoltaic cells, where the entire solar cell is composed of p and n-doped organic polymers and energy transfer between light absorbing and current conducting species could be essential.



# Hybrid InGaN/F8BT light emitting diodes

#### 3.1 Previous work

A few examples for the application of resonance energy transfer in hybrid LEDs, including the work by my predecessor Dr. Soontorn Chanyawadee, were mentioned in the introduction. He studied energy transfer from a InGaN-based MQW LED to a layer of QDs deposited into the holes of a photonic crystal fabricated on the top surface of the LED [21, 56]. The sample for the study was a wafer for blue emitting LEDs (peak wavelength around 460 nm) provided by LuxtalTek, Taiwan. The LEDs' surface was nanostructured with a photonic crystal to enhance the outcoupling of emitted light that otherwise would predominantly remain trapped inside the wafer due to the high refractive index of GaN. In the previous study two designs were compared: an LED with a hole pattern etched with the standard depth, and an LED where the hole pattern is etched deeper than it is usual for the production of such devices. In this case the etching goes through the MQW layers. Both LEDs were covered with a thin layer of QDs which absorb part of the blue light from the LED and re-emit light at a lower energy. Thus, they act as much as colour converters as the traditionally used rare earth doped phosphors. The two samples, which are schematically depicted in Fig. 3.1, were operated at currents which yield the same amount of blue light from the LEDs before the addition of QDs. It was found that the emission from the QDs is enhanced in the deep-etched LED due to additional transfer of excitations from the QWs to adjacent QDs at the revealed interfaces of the deep etched holes. In this process excitons are transferred via non-radiative resonance energy transfer without the transfer of net charge. The presence of energy transfer was concluded from the enhanced QD emission and the characteristic photoluminescence decay curves of the MQW and the QDs, which both were in agreement with

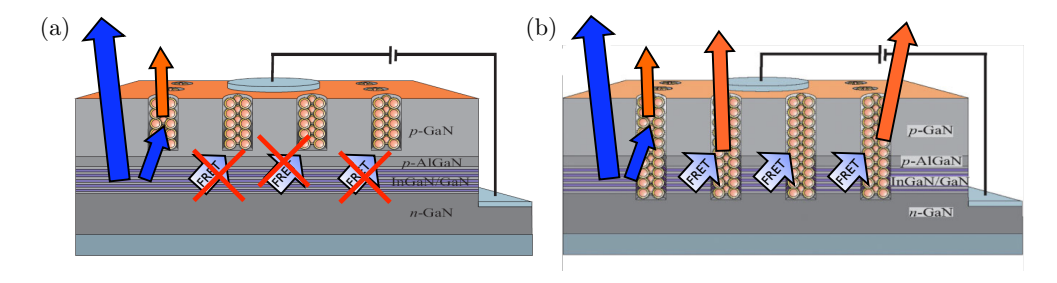


**Figure 3.1** – Schematics of the shallow (a) and deep (b) etched LEDs with QDs in the holes of the photonic crystal. The unlabelled arrows indicate emission of blue and yellow light by the LED and QDs, whereas the arrows labelled with "FRET" indicate resonance energy transfer. The schematic of the heterostructure is reproduced with permission by the creator Dr. Soontorn Chanyawadee.

the model rate equations for the energy transfer process. The work is described in detail in Refs. [21, 56].

This chapter will give an overview of the experiments performed with never samples since the studies of my predecessor. Here, different LED wafers are covered with the polyfluorene F8BT and resonance energy transfer from the QWs to the F8BT is characterised. Focus is given in particular to the emission of white light from the hybrid LED.

#### 3.2 Materials and methods

#### 3.2.1 Different generations of GaN/InGaN multiple quantum well wafers

#### 3.2.1.1 First generation of LED wafers

All generations of InGaN/GaN LED wafers for the studies in this chapter were fabricated and supplied by LuxtalTek, Taiwan. For the first generation of wafers that were studied in Refs. [21, 56] LuxtalTek provided wafers that are usually manufactured into LED devices. These samples were only briefly used in the context of this work to compare them to newer sample generations. Nevertheless, they are still discussed here because their epitaxial structure is identical to the one found in later generations. Moreover, knowledge about the first iteration of samples facilitates placing the work from this chapter in the context of the previous work. The epitaxial growth for these samples starts with 2  $\mu$ m of undoped GaN as a buffer layer on a sapphire substrate. This is followed by a 2  $\mu$ m thick layer of n-doped GaN. The active layer of the LED wafer consists of five In-GaN/GaN QWs which are slightly offset in energy to yield a broader emission spectrum. On top of the QWs a 50 nm thick p-doped AlGaN layer is grown before the structure is terminated with a 0.2  $\mu$ m thick p-doped GaN layer. The doped GaN layers allow the electrical injection of carriers into the QWs when metal probes are placed onto the

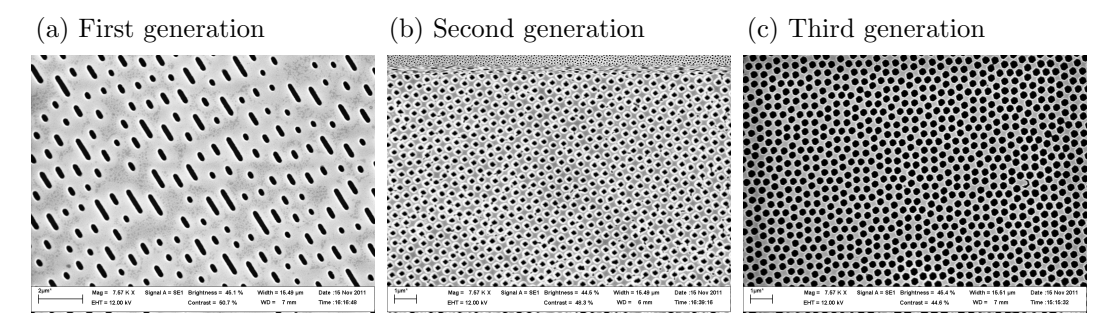


**Figure 3.2** – Comparison of the different hole patterns on different generations of LED wafers. Figures (a)-(c) show images obtained with a scanning electron microscope at the same magnification. It can be seen that the filling factor and hole shape varies between different sample generations.

top surface and onto the buried n-doped layer which is revealed by purposely scratching the surface. Dr. Martin Charlton from the School of Engineering and Computer Science at the University of Southampton developed the required nanoimprint lithography and etching processes to produce the photonic crystal hole pattern on the wafers. The motivation to fabricate a pattern onto the LED wafer originates from the dramatically enhanced outcoupling of light from the high refractive index material with the help of a photonic crystal. It should be noted, that in this first sample generation the fabricated hole pattern was not a computed and optimised photonic crystal, but a random part of the bit pattern of a DVD. The resulting pattern along with the patterns used for later sample generations is shown in Fig. 3.2. The hole patterns can be etched into the surface of the wafer with two different depths. While in the shallow etched sample the holes do not reach the QWs, in the deep etched sample they penetrate through the QW layers, enabling resonance energy transfer from the QWs to a colour converter deposited into the holes. The details about the previous experiments as well as the nanoimprint and reactive ion etching process can be found in Refs. [21, 56]. References 57, 58 present recent results from the group of Dr. Martin Charlton on fabrication techniques and real world performance of photonic crystal LEDs based on the same material system as the one studied here. Although strongly related in terms of their content, these projects were unrelated to the work presented in this chapter.

# 3.2.1.2 Second generation of LED wafers featuring a photonic crystal and surface passivation

Another direct consequence of etching the holes deep into the LED surface is the decrease of the quantum yield and photoluminescence lifetime of the QW excitons. Non-radiative carrier recombination occurs at the lateral surfaces of the revealed QWs. Also, a longer and more aggressive etching process produces more cracks and defects in the crystal structure which also result in a loss of quantum efficiency. Evidence for these detrimental effects will be given in the results section. To compensate for the detrimental effects of

the etching some of the second generation wafers were treated with a surface passivation procedure directly after the etching process. (The etching procedure itself is confidential information and is not known to the author.) An effective surface passivation was achieved by exposing the samples to phosphoric acid (H<sub>3</sub>PO<sub>4</sub>). The effect of the surface passivation will be discussed in the results section. The second wafer generation also features an actual photonic crystal pattern on the surface. This pattern was designed by Dr. Martin Charlton, but fabricated in the production facilities at LuxtalTek. As it will be seen in the results section, the reliable electrical characterisation of this second generation of wafers remains a challenge because of the lack of metal contacts.

#### 3.2.1.3 Third generation of LED wafers featuring individual LEDs

Difficulties with the electrical characterisation were finally resolved in the third generation of wafers. In contrast to the previous two generations these wafers feature individual LED chips which are equipped with dedicated areas to make electrical contact. The buried n-doped GaN layer is revealed over a dedicated area and the upper contact is made via a few nanometres thin metallic overlayer to enhance the current spreading over the top surface. This wafer generation again featured a modified photonic crystal (Fig. 3.2(c)). Unfortunately, this third generation of wafer is only available with an unknown depth of the etched holes, making a comparative study of any kind is impossible.

#### 3.2.2 The polyfluorene F8BT

Preliminary considerations lead to the conclusion that the blue emission of the LED wafer in combination with the yellow emission of the polyfluorene Poly(9,9-dioctylfluorene-altbenzothiadiazole) (F8BT) end-capped with 2,5-dimethylphenyl result in white light (the molecular structure of the polyfluorene is depicted in Fig. 2.2). For the purpose of general lighting applications this is desirable and the combination of these two constituents also has the potential to be a good pair for resonance energy transfer. The emission spectra of the LED and F8BT as well as the absorption spectrum of F8BT are shown in Fig. 3.3. Here, a variant of F8BT is used that absorbs strongly at the emission wavelength of the LED in the spectral region around 460 nm. In chapter 4 we study another variant of F8BT that has very similar emission properties, but absorbs around 375 nm. For sample preparation the polymer is dissolved in toluene and equal amounts of the solution are deposited as droplets onto the different samples. After evaporation of the solvent this yields circular patches of approximately 8 mm diameter.

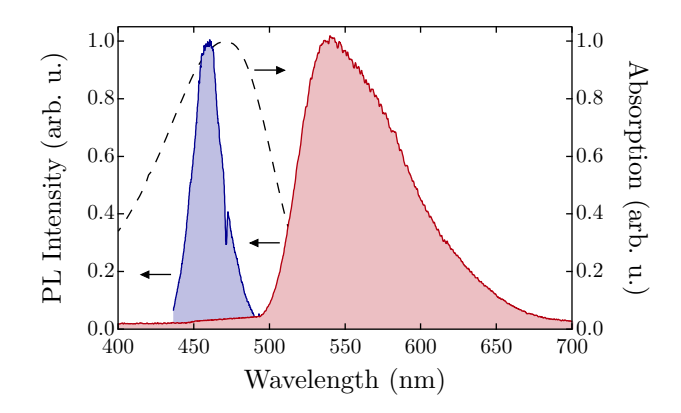


**Figure 3.3** – Spectral overlap between LED emission (blue filled graph) and F8BT absorption (black interrupted line). The red filled curve shows the emission spectrum of F8BT.

#### 3.2.3 Optical characterisation

#### 3.2.3.1 Colorimetry

In continuation of the previous work with the InGaN/GaN-based MQW LED wafers this work aims for white light emission from hybrid LEDs that exploit resonance energy transfer. The design of LEDs which are perceived as "white" requires careful consideration of the spectral properties of the colour converters. To date, the technical characterisation of colours and light sources bases mainly on the standards set by CIE, the International Commission on Illumination (Commission internationale de l'éclairage) in 1931. The 1931 CIE XYZ colour space is a standard to describe the brightness and chromaticity of any colour. The left part of Fig. 3.4 shows the 1931 colour space chromaticity diagram which contains all colours at their maximal brightness (the representation on a computer screen or a printed page is necessarily limited by the primary colours of the device). The 1931 CIE colour space is accompanied by the 1931 CIE RGB colour space which is distinguished by a particular choice of monochromatic primary colours (Red, Green, and Blue) and a specific white point. Later, other colour spaces for specific purposes were suggested. However, their use is generally limited to a certain field and the 1931 CIE XYZ colour space is still most commonly used to describe colours. For computer graphics RGB colour spaces are more convenient than the CIE XYZ space. For consumer grade digital cameras and displays the sRGB colour space is widely used.

I have developed a program to facilitate the process of identifying colour converters which are appropriate to yield white light in combination with the blue LED emission. The program loads several experimentally determined emission spectra from different sources like the LED wafer, colloidal QDs or organic polymers and calculates the effective CIE coordinates for the sum of these emitters. In order to test if a specified white point in the 1931 CIE XYZ colour space can be reached with a given combination of emitters their relative contributions can be adjusted. "Live" visual feedback accelerates the process of finding the appropriate relative contributions of the emitters and enables fast testing of

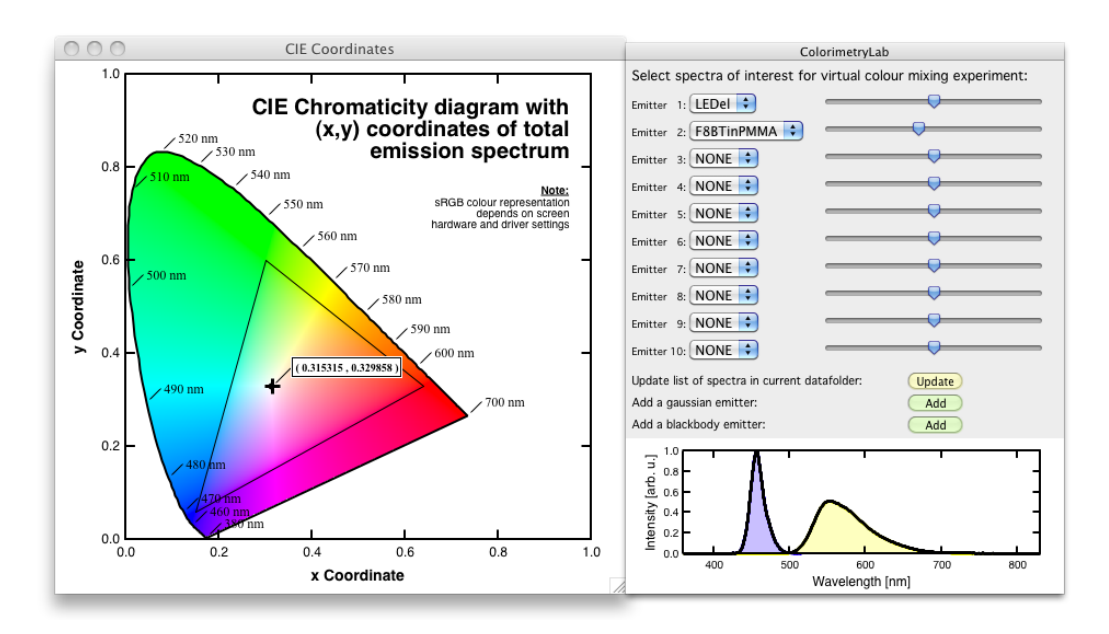


Figure 3.4 – Screenshot of the ColorimetryLab program written in Igor Pro. Left part: chromaticity diagram of the 1931 CIE colour space. The triangle shows the gamut of sRGB, a common standard for the use on monitors, printers, and the Internet. The black cross and black dot (partly covered by the cross) represent the CIE coordinates of the spectra shown on the right and the white point of the sRGB standard, respectively. Right part: the user interface which allows to predict the colour resulting from a combination of different emission spectra. The blue and yellow spectra are the emission spectra of the LED wafer and a layer of F8BT in Poly(methyl methacrylate) (PMMA), respectively.

different emitter combinations. Also, any electroluminescence spectrum can be loaded into the program to determine the colour it represents. A screenshot of the program is presented in Fig. 3.4.

In a later stage the program could be updated such that it computes the colour rendering index (CRI) and correlated colour temperature (CCT).

"The color rendering index (CRI)..., is a quantitative measure of the ability of a light source to reproduce the colours of various objects faithfully in comparison with an ideal or natural light source." <sup>1</sup>

Evidently, the CRI of a white light source is an important parameter to compare the performance of different white light sources. The CCT is another important quantity to characterise a white light source. The CCT is the temperature of a planckian black-body radiator whose colour is closest to the colour of the white light source. Note, that proximity between different colours is well defined within a colour space. Natural daylight resembles to a good approximation a Planckian spectrum and has a CCT of approx. 5500 °K. While a "cold" Planckian light source is more orange-tinted, a "hot" source is blue-tinted. The calculation of the CCT and CRI is cumbersome because it

<sup>&</sup>lt;sup>1</sup>From wikipedia.org, Color rendering index, http://en.wikipedia.org/wiki/Color\_rendering\_index (as of Nov. 13, 2010, 21:26 GMT).

requires the numerical integration of the sample spectrum convoluted with 14 tabulated reference spectra describing the reflectance of objects with typical colours like "leaf of tree" or "skin colour" as well as a number of non-linear coordinate transformations [12]. For this reason the programming of this functionality has been withheld until the actual necessity for this step arises and the available functionality in commercial programs has been reviewed.

#### 3.2.3.2 Measurement of time resolved photoluminescence with a streak camera

Resonance energy transfer is routinely identified and quantified on the basis of time resolved photoluminescence measurements [1, 21, 59]. Here, the photoluminescence decay dynamics of the QWs in the LED wafers are recorded with a streak camera (Hamamatsu C5680). This is a device which in conjunction with a spectrometer and a pulsed light source for excitation allows the simultaneous measurement of the temporal and spectral characteristics of a photoluminescence signal. It is usually operated in a repetitive fashion using a pulsed laser source to excite the sample, but also single shot operation has been demonstrated [60]. Recently, a streak camera has been used to perform femto photography [61]. For the non-resonant excitation of photoluminescence the wafers are excited at 400 nm with the frequency doubled output beam of a Ti:saphhire regenerative amplifier operating at 250 kHz. The amplifier is seeded from a mode locked Ti:sapphire oscillator with a repetition rate of 80 MHz. This yields amplified pulses with a temporal width of  $\sim 250$  fs at 800 nm and a bandwidth corresponding to 14 meV. Frequency doubling tends to shorten the pulses and reduce their bandwidth because of the nonlinear nature of the process, but this effect is irrelevant for the non-resonant excitation scheme. These experiments are performed at a range of excitation energy densities per pulse covering 50 μJcm<sup>-2</sup>, 250 μJcm<sup>-2</sup>, 1250 μJcm<sup>-2</sup> and 6250 μJcm<sup>-2</sup>. The lower end of the range was chosen to ensure excitonic recombination in contrast to free carrier recombination which may be found at higher excitation densities. This aspect is discussed further in section 3.3.2. For the operation of the streak camera light emitted from the sample is collected with a lens and passes through a spectrometer before it is guided onto a photocathode which in turns emits a number of photoelectrons proportional to the number of photons. The electrons are accelerated by an electric field and pass a vertical electric field between two sweep electrodes. The vertical electric field increases and collapses ("sweeps") once per excitation pulse and hence the vertical deflection of the electrons depends on when they pass through the vertical field. Early electrons are deflected less than later electrons. After passing the sweeping field the electrons hit a multichannel plate for their multiplication and reach a phosphor screen which undergoes phosphorescence when hit by the electrons. Finally, light from the phosphor screen is detected with a CCD (charge coupled device) camera that is mounted directly behind it. The resulting image shows the photoluminescence resolved in time and wavelength along the two axes. The time range covered by the sweeps of the streak camera depends

on the installed sweep unit which in turn is matched with the repetition rate of the excitation source in use. Whereas the slow sweep unit used in this experiment allows to cover time windows between 5 ns and 10 ms and can be triggered at the repetition rate of the regenerative amplifier at 250 kHz or slower, the fast sweep unit operates only at the fixed repetition rate of the main oscillator (80 MHz) and covers time windows between 200 ps and 2000 ps. The temporal resolution, defined as the width of the instrument response function, is obtained from the time profile of the laser pulse as it is measured by the camera. In this particular experiment with the slow sweep unit it is 200 ps, but it varies with the settings and time range of the measurement. The fast sweep unit yields a resolution of 25 ps or better, depending on the chosen time window.

#### 3.2.4 Electrical characterisation

The electrical characterisation of the LED wafers requires great care because the samples, as explained above, are lacking sound electrical contacts in the form of highly conductive metallic layers. On the first and second generation of wafers the surface is scratched thoroughly with a diamond scribe such that the buried n-doped layer is revealed. The wafer is connected to a current supply via one spring loaded metallic needle which is positioned onto the scratched area and a second blunt probe that is carefully touching the top surface. Micropositioners and a far field microscope are used to accurately position the probes on the sample surface. This scheme does allow for electrical carrier injection into the wafers, but the contact to the material is poor and there is a permanent risk to shorten the device when the needle in the scratched groove touches the buried contact and the top layer at the same time. At the required currents, which are of the order of a few mA, the material tends to heat up too much at the point of contact and as a consequence the circuit is often shortened, leaving behind a black, burned spot. Evidently, this hinders an accurate comparative study of the amount of light emitted from the wafer under standardised conditions. Nevertheless, an attempt is made.

In order to conclude whether non-radiative energy transfer from the QWs in the wafer to the polyfluorene material in the holes of the photonic crystal enhances the colour conversion, electroluminescence from the wafer and secondary luminescence from the polyfluorene layer has to be accurately measured. This requires a detector with a high dynamic range because the intensity of the electroluminescence and the secondary luminescence is measured over a large range of injection currents. Moreover, the optics collecting the light and guiding it to the detector have to be accurately positioned and refocussed for the different colours. The system has to be well aligned and reproducably operated, otherwise misalignment would be falsely interpreted as a reduction in the intensity of the emitted light. Therefore a high dynamic range CCD array was chosen to record standard images of the wafer area around the top electrode where the majority of light is being emitted from. Figure 3.5 shows a false colour representation of the top

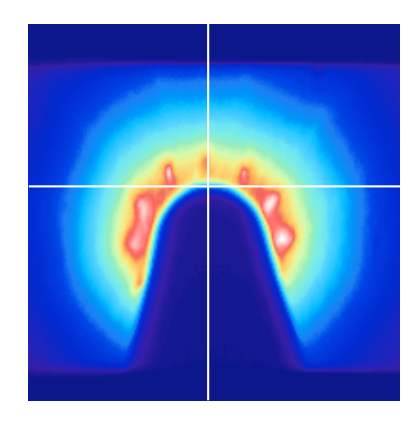


**Figure 3.5** – False colour image of the electroluminescence from the LED wafer. The superimposed crosshair was used to align images from different measurements repeatably on the detector. Evidence for the non-isotropic emission due to the photonic crystal can be found in the angular emission pattern.

view under standard conditions onto the LED wafer under electrical carrier injection. It can be seen that light is emitted around the top contacting electrode. The image shows an area of approx.  $4 \text{ mm} \times 4 \text{ mm}$  and does not show the needle shaped probe contacting the buried n-contact. The needle probe is approximately 1.5 cm away from the imaged area. Due to poor current spreading in the top contact light emission is confined to a few mm around the point of the contact and naturally the area with the brightest emission is shadowed by the probe itself (see again Fig. 3.5). This image of the electroluminescence also shows the non-isotropic emission pattern due to the photonic crystal. Due to a lack of knowledge about the proprietary geometry of the photonic crystal a quantitative analysis of this emission pattern is omitted here. It is evident from the regular intensity features shown in Fig. 3.2 that the positioning of the etched holes does indeed follow some systematic pattern. When the wafer is covered with F8BT the QW emission and F8BT emission are recorded separately by the use of short and long pass filters. The appropriate correction procedure is undertaken to account for any light that is unintentionally leaking through the filters. The effectiveness of the filters and the correction procedure is checked once before the recording of the data by spectrally resolving the light that goes onto the CCD. In addition to the quantitative and comparative measurement of the emission intensities also RGB images of the wafer covered with the polyfluorene are taken with a CMOS camera. These images are not analysed in any particular way but they do indicate that the emission from the QWs and the F8BT can be successfully separated by the use of colour filters. The are shown for reference in Fig. 3.6.

A self written LabView program is employed to automatically acquire the images of the LED wafers with the CCD detector for a range of currents. The current is supplied by a Keithley 236 Source-Measure unit. Data acquisition for the electrical characterisation of the second generation LED wafers follows these steps:

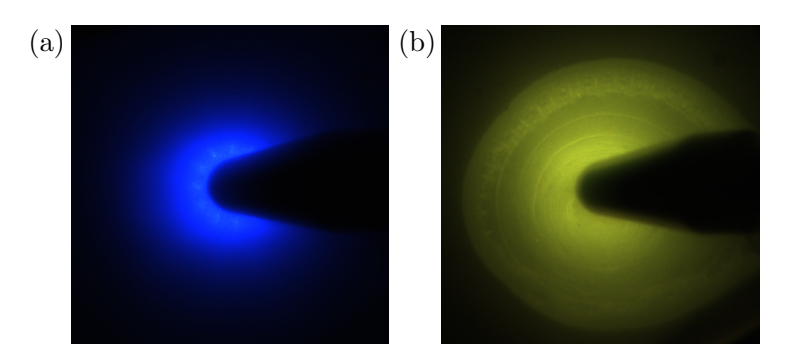


**Figure 3.6** – Colour filtered images of the LED wafer covered with F8BT. (a) Recorded with the use of a 500 nm short pass filter. (b) Recorded with the use of a 550 nm long pass filter. The edges of the droplet of the F8BT solution can be seen in (b).

- 1. Bring the needle probe into a suitable position on the scratched area and turn on the power supply with a low current setting.
- 2. Position the upper electrode with the help of the CCD image and contact the sample surface such that electroluminescence is observed.
- 3. Slowly ramp up the current and check whether the current contact spot can sustain higher currents. If the contact heats up excessively and the circuit is shortened move the sample marginally and restart from step 1.
- 4. If the spot is suitable start the program. The program ramps up the current from zero to 12 mA in steps of 0.25 mA. For each step one image with the CCD array is taken to record the QW emission through the appropriate filters. If during the ramping of the current the electrical contact to the wafer is lost the measurement is aborted and restarted from step 1.
- 5. If the current sample is coated with the polyfluorene, replace the short pass filter in the collection path with the long pass filter and repeat the current ramping to measure the emission from the polyfluorene in the same way as the LED emission. If during the ramping of the current the electrical contact to the wafer is lost the measurement is aborted and restarted from step 1.

For the second generation of LED wafers the complete procedure was performed ten times each for the shallow and deep etched samples and before and after the deposition of the polyfluorene.

#### 3.3 Results and discussion

## 3.3.1 Effect of etching and surface passivation on the photoluminescence lifetime

To study the detrimental effect of the deep-etching process on the quantum efficiency as well as the effectiveness of the subsequent surface passivation time resolved photoluminescence measurements are performed with the streak camera. Two pieces of the LED wafers are studied where the photonic crystal is shallow and deep-etched into the surface. Additionally, each sample was partially subject to the surface passivation procedure after the etching process (see sample description). In order to check whether energy transfer is enabled in each sample the photoluminescence decay of all samples is measured before and after coating with F8BT. Figure 3.7 shows the experimental data measured at an excitation energy density per pulse of  $E = 50 \,\mu\mathrm{Jcm^{-2}}$ , which is sufficiently low to guarantee excitonic recombination. Before the effect of resonance energy transfer will be discussed, focus is given to the effect of the surface passivation on the photoluminescence decay dynamics. Both, the shallow and deep etched samples with surface passivation show slower photoluminescence decays than their unpassivated counterparts, indicating a successful passivation. When comparing the unpassivated shallow and deep etched samples it is evident, that the latter shows strongly quenched photoluminescence due to non-radiative exciton recombination at the surfaces of the laterally

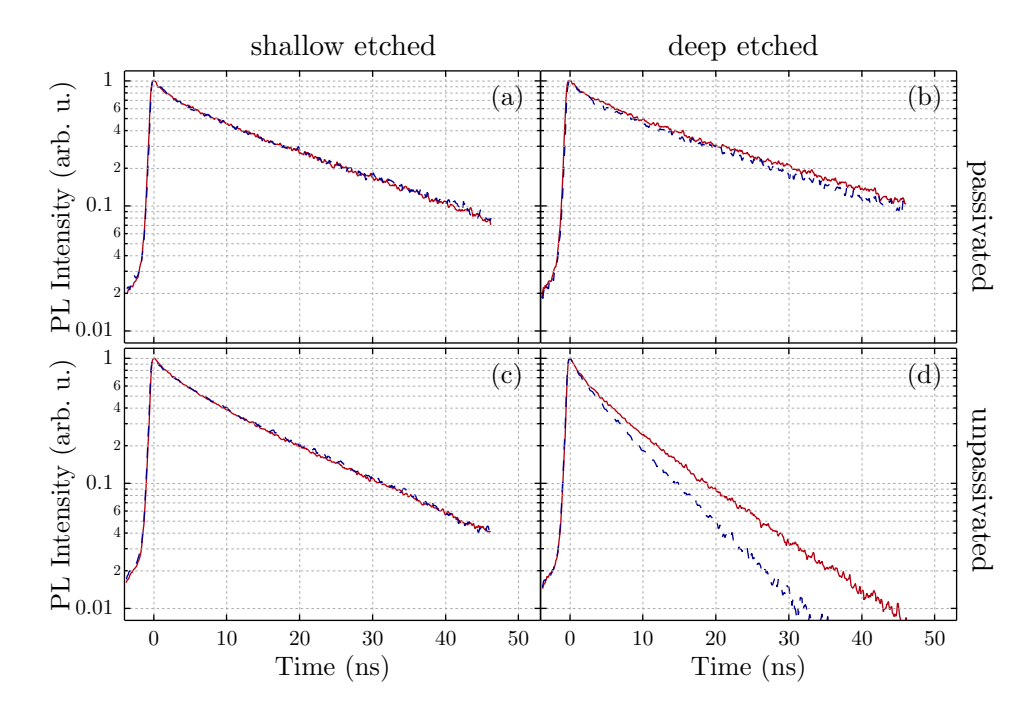


**Figure 3.7** – Effect of surface passivation and deep etching on the photoluminescence decay of the QWs. The photoluminescence decay of the QWs in absence and presence of the F8BT is indicated by solid red and interrupted blue curves.

revealed QWs. As a result the photoluminescence decay time is shorter and the deep etched LED wafer emits less light for the same density of injected carriers. The successful passivation of the disturbed QWs is proven by the increase of the photoluminescence decay time for both the shallow and deep etched sample. In the deep etched wafer the passivation "heals" the undesired carrier recombination at the QW cross sections and the photoluminescence of the shallow etched and passivated sample is recovered. But also the shallow etched sample benefits from the passivation step because the etching process introduces microscopic cracks in the crystal that apparently penetrate through the QWs. These also contribute to undesired defects and non-radiative recombination in the QWs and are successfully healed by the application of the passivation step. From the studies of my predecessor it is well known that the deep etched holes are a requirement to enable resonance energy transfer in these samples, but that this comes at the cost of a reduced quantum efficiency of the QWs. Is the passivation then the key to the successful application of energy transfer in such structures? An answer will be given shortly.

As expected, both the unpassivated and passivated shallow etched samples show absolutely no quenching after the deposition of F8BT (see Fig. 3.7). Non-radiative resonance energy transfer plays no role in the shallow etched samples and can only be observed on the deep etched samples. The unpassivated deep etched sample shows a substantial quenching upon addition of the F8BT (bottom right graph in Fig. 3.7). The efficiency of the quenching is 28 % and significantly exceeds the previously reported value of a few percent for the first generation sample [21]. This is attributed to two factors: a) The fill factor of the hole pattern has increased from 12 % to 40 % such that the mean free path for carriers before arrival at an etched hole has reduced noticeably (see SEM images from Fig. 3.2). b) The spectral overlap between the QW emission and polyfluorene absorption is optimal and the material combination seems to be a perfect match that promises high energy transfer rates and high colour conversion efficiencies. This result is a very encouraging first step and it is hoped that resonance energy transfer noticeably enhances the emission from the F8BT under electrical operation of the hybrid device.

Finally, consider the passivated deep etched and shallow etched samples (3.7). As expected, the shallow etched sample with surface passivation does not show any quenching after the addition of the F8BT. The deep etched passivated sample does show some photoluminescence quenching upon addition of the polyfluorene, although the efficiency of the quenching does not exceed 1 %, which is more than one order of magnitude less than what is observed for the unpassivated deep etched sample. Apparently, the surface passivation introduces an insulating layer on the sidewalls of the holes which is so thick that excitons do not reach close proximity within approximately ten nanometres with the F8BT molecules on the sidewalls. This does indeed prohibit undesired non-radiative carrier recombination, but it also prevents the transfer of excitation energy from the QW to the polyfluorene via near field dipole-dipole coupling. Consequently, the passivated

samples have very limited use for the study of energy transfer. Successful passivation comes at the cost of preventing the desired resonance energy transfer process.

#### 3.3.2 Quenching of energy transfer at high excitation densities

In the previous section the quenching of the QW photoluminescence due to energy transfer to the F8BT layer was discussed. What has been omitted from the discussion is the observation that the quenching does depend on the excitation density. This is clearly seen in Fig. 3.8 where photoluminescence data for a range of excitation energy densities is shown. With increasing excitation density an accelerating fast component can be identified (red interrupted lines in Figs. 3.8(a)-(d)) and the quenching due to energy transfer is vanishing. This is typical for the high carrier density regime where excitons begin to ionise and free carriers participate in Auger recombination of excitons or unbound electron-hole pairs [62, 63]. The exciton density  $n_{\rm Mott}$  at the Mott transition can be approximated for a QW by the relation

$$n_{\text{Mott}} \times a_{\text{X.B.2D}}^2 = 1, \tag{3.1}$$

where  $a_{\rm X,B,2D}$  is the 2D exciton Bohr radius. This yields a value of  $n_{\rm Mott}=1.7$  ×  $10^{17}$  m<sup>-2</sup>. At the lowest excitation density,  $E_0$ , the density of photons incident on the wafer is  $N_{\rm ph,0} = 10^{14} \, \mathrm{m}^{-2}$ , while it is  $N_{\rm ph,max} = 1.25 \times 10^{16} \, \mathrm{m}^{-2}$  for the highest excitation density corresponding to  $E_{\text{max}} = 125 \times E_0$ . Because of the commercial interests of the manufacturer LuxtalTek the actual composition of the multiple QWs as well as the in and out coupling efficiencies for light of different wavelengths into the wafer are not known to the author. Hence, only a rough estimate about the number of excited electron-hole pairs in the QWs can be provided. In eq. 3.1 the Bohr radius of a strictly two dimensional exciton was used. This value is two times smaller than the 3D exciton Bohr radius, and thus eq. 3.1 overestimates the exciton density at the Mott transition when a QW with a thickness greater than the 3D Bohr radius (3.4 nm for InGaN) is considered. At the excitation energy density  $E_{\text{max}}$ , the pronounced bi-exponential decay and the lack of any quenching upon addition of the F8BT indicate that the carrier density lies well above that of the Mott transition. The pronounced energy transfer quenching and a nearly exponential photoluminescence decay at  $E_0$  support the hypothesis that here the exciton density lies well below the Mott density. The probability of Auger recombination increases with the density of free carriers and becomes more pronounced at high excitation densities. From the photoluminescence decay curves it can be seen that only the fast component of the decay accelerates with increasing excitation densities. The tails of the decays follow similar dynamics for all measurements, except for the first curve at the lowest excitation density where possibly a substantial fraction of localised excitons with a characteristic recombination time is contributing to the observed photoluminescence. The decrease of energy transfer quenching with

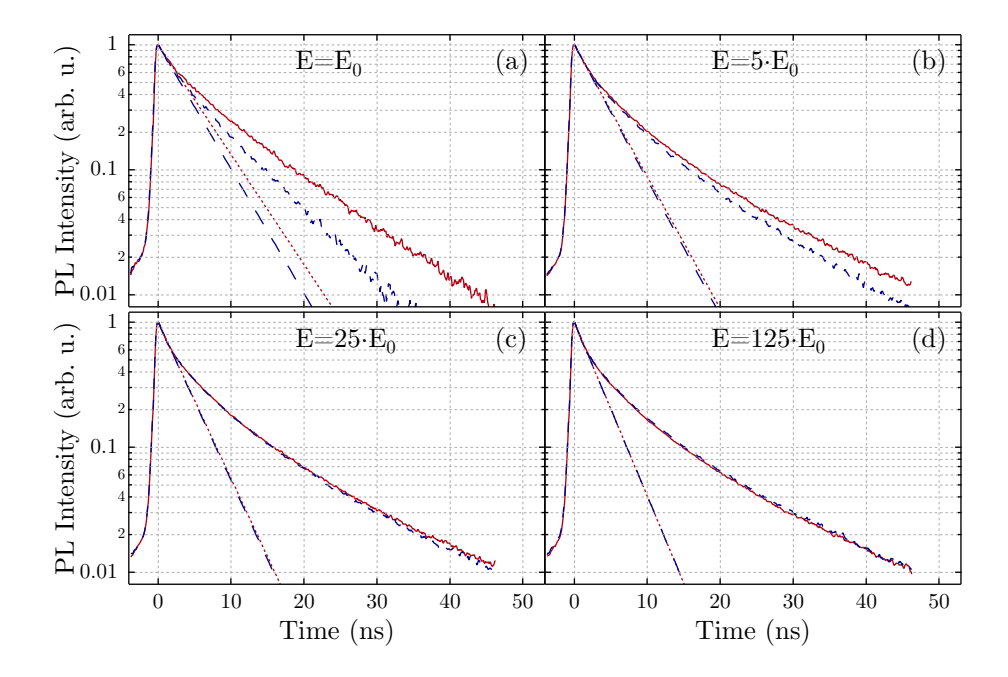


Figure 3.8 – Power dependence of the time resolved photoluminescence of the QW before (red curves) and after addition of F8BT (interrupted blue curves).  $E_0 = 49 \,\mu\text{Jcm}^{-2}$  is the energy density of the excitation pulse on the sample. The interrupted lines with corresponding colour are exponential decays fitted to match the first 2 ns of the decays.

increasing excitation density can be understood from the theoretical considerations by Basko et al. [29] which show that resonance energy transfer from free electron-hole pairs is very slow compared to the exciton recombination time and is not expected to contribute substantially to the recombination dynamics at all as long as a considerable exciton population is present [64]. Accordingly, only when the entire carrier population is dominated by free carriers, the slow energy transfer time for free carriers can become comparable with the slow radiative recombination time for free carriers and energy transfer can potentially play a role in their dynamics. In the three measurements with the higher excitation densities the majority of carriers recombine quickly via Auger recombination such that only a small population of excitons is remaining and energy transfer from these has a negligible effect on the photoluminescence of the entire carrier ensemble.

#### 3.3.3 Increased colour conversion due to resonance energy transfer

So far we have collected evidence for resonance energy transfer from photoluminescence measurements. It remains to be seen whether the pronounced photoluminescence quenching that is interpreted as energy transfer leads to measurable enhancements of the colour conversion in the device under electrical carrier injection. Due to the described difficulties associated with making electrical contact to the samples ten independent measurements of the electroluminescence are combined to yield the intensity vs current

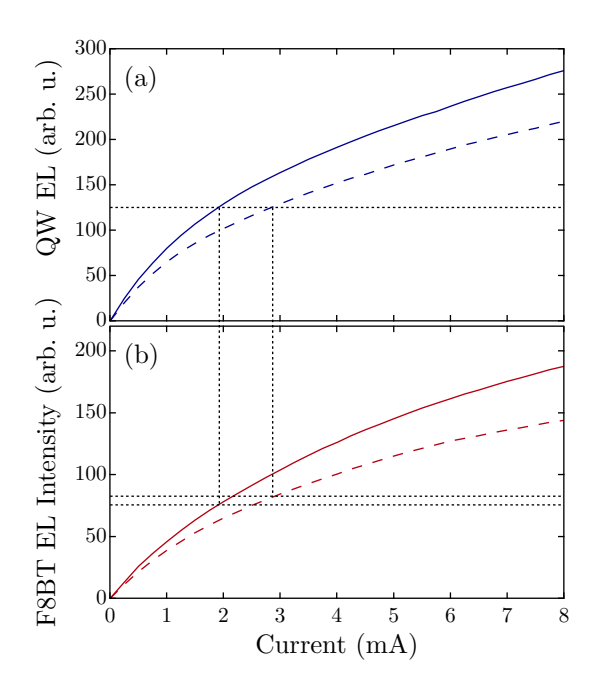


Figure 3.9 – Colour conversion in the deep and shallow etched LED covered with the polymer F8BT. (a) Electroluminescence of the shallow and deep etched QWs without F8BT vs injection current. Shallow etched: solid curve. Deep etched: interrupted curve. (b) Secondary luminescence of the F8BT layer vs injection current for the shallow (solid curve) and deep etched QWs (interrupted curve). It can be seen that for a comparable QW emission the polymer emission is enhanced in the deep etched device.

curves discussed in this section. Both, the QW electroluminescence (in absence and presence of the F8BT) as well as the secondary luminescence from the F8BT is measured. The resulting averages of these measurements are shown in Fig. 3.9. In the upper graph it is seen that the emission intensity increases with the injection current, but that the increase slows down for larger injection currents. This effect is characteristically referred to as efficiency droop and is fundamentally limiting the performance of solid state light sources at the high injection currents required for their efficient operation in single chip LED or laser diodes. To date its origin remains unknown and only speculative explanations and hints have been provided, some of which are summarised, rejected and refined in Ref. 65. Accordingly, neither the junction temperature nor the carrier density in the QW cause the efficiency drop off because it occurs only under electrical pumping conditions, but not under optical carrier injection. The authors propose that under electrical operation polarisation fields in the MQW allow the escape of electrons from the QWs and thus quench the electroluminescence. The discussion of the origin continues and a very recent attempt for an explanation can be found in Ref. 66.

The luminescence from the F8BT is referred to as "secondary luminescence" because it is not directly caused by the electrical injection of carriers into the polymer, but rather by the absorption of photons and excitation energy originating from the QW which in turn is electrically driven. The deposition procedure for the F8BT layer ensures that

different samples feature comparable layers of the polymer. Moreover, the measurement of the luminescence is not a point measurement but instead it measures luminescence from an area such that inhomogeneities in the layer thickness are averaged out. In both samples the F8BT layer absorbs a considerable fraction of the blue photons emitted from the QW and re-emits. Hence, the emission intensity follows a trend proportional to the emission of the QW itself, including the efficiency droop effect. However, a closer examination reveals that the deep etched sample yields stronger luminescence from the F8BT layer, indicating enhanced colour conversion in this sample. The enhancement can be determined graphically from Fig. 3.9. The upper figure shows the QW emission intensity for different injection currents before the addition of F8BT. For any value of the emission intensity, for example the one chosen in Fig. 3.9(a), the injection currents that yield this level of intensity for the shallow and deep etched sample can be determined. Then, the F8BT emission for these currents can be compared, and it is found that the secondary F8BT luminescence is enhanced by approx. 10 % in the deep etched sample in comparison to the shallow etched sample. It could be argued, that this effect stems from the photonic crystal which couples out the light from the structure with different efficiencies depending on whether they are deep or shallow etched. But here the normalisation is performed for equal amounts of blue light that escape from the structure and in both cases the F8BT fills the shallow and deep etched holes of the photonic crystal. After ruling out optical effects for the enhanced emission, and in view of the photoluminescence quenching in the deep etched sample upon addition of the polymer layer, we propose that it originates from resonance energy transfer. However, the observed increase in the colour conversion efficiency of approx. 10 % is low compared to the efficient photoluminescence quenching of 28 % for the low excitation density regime. This value is also lower than the previously observed colour conversion enhancement of 43 % from Ref. 21. A possible explanation can be found in the particular band alignment between the polyfluorene and the InGaN QW (shown in Fig. 3.10). With direct contact, electrons will quickly transfer back to the semiconductor if they do not diffuse further into the polyfluorene or recombine with a hole. This is because the electron affinity of the polyfluorene is 1.8 eV lower than that of the InGaN. The electron affinity of organic polymers is generally lower than that of inorganic semiconductors and this type of detrimental back transfer can only be prevented by the inclusion of an insulating layer which is thick enough to prevent the back transfer, but thin enough to enable efficient non-radiative energy transfer. This leaves little margin for the thickness of the insulating layer which has to be on the order of only a few nanometres, a thickness that is hard to achieve reliably for devices. Alternatively, colloidal QDs, which themselves are generally not conductive could be used, or the electron conducting organic polymer F8BT could be embedded into an insulating matrix like PMMA. As it will be detailed in the next section, this was indeed necessary for another reason: to achieve a sufficient thicknesses of the F8BT on the surface of the wafer. However, another study of energy transfer between the two conjugated polymers Poly(9,9-dioctyl fluorene) (F8) and

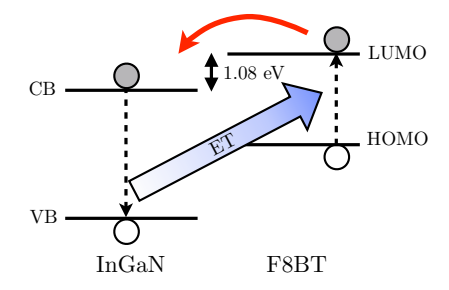


Figure 3.10 – Back transfer of electrons from the polyfluorene to the InGaN QW. Energy offsets not drawn to scale.

F8BT in a ternary blend containing the polymer PMMA showed a strong suppression of excitonic energy transfer [67]. The authors argue that the PMMA effectively "dilutes" the polyfluorenes and thus limits energy transfer and exciton diffusion. They conclude that adding a third chemically dissimilar polymer to a binary conjugated-polymer blend alters the electronic properties and can be used to suppress excitonic energy transfer.

Finally, for the application in real world devices it is important to know whether it is worth sacrificing the quantum efficiency of the device in order to employ resonance energy transfer in the deep etched sample for an enhanced colour conversion. In order to answer this question one would need to compare the electrical power that is need to drive the shallow and deep etched LEDs. Although both the current and voltage is recorded in these measurements, only the injection current can be seen as a meaningful number. Due to the poor electrical contact between the two probes and the wafer material the voltage required to drive the same current through the same sample but under different contact conditions can be orders of magnitude apart. This makes it effectively impossible to draw conclusions about the *total colour conversion efficiency* which considers how much electrical power is needed to obtain emission from the device.

#### 3.3.4 White light emission

Preliminary considerations lead to the conclusion that the F8BT layer on the LEDs studied in the previous sections is by far not thick enough to yield white emission as the result of an appropriate balance between the blue QW emission and the yellow emission from the F8BT. Additionally, overloading the samples with the pure polymer from highly concentrated solutions does not yield stable films of F8BT. Instead, the polymer can easily be scratched of by the probes. Therefore another approach is taken: the F8BT can easily be implemented into a PMMA (Poly(methyl 2-methylpropenoate)) matrix by adding some PMMA to the solvent containing the F8BT. By adjusting the ratio of the two constituents the required thickness of the F8BT containing colour conversion layer can be reached. It should be noted that the emission wavelength of F8BT shifts from 540 nm to 550 nm when it is embedded in PMMA. The shifted spectrum is still perfectly suited to mix white light in combination with the blue LED emission and it

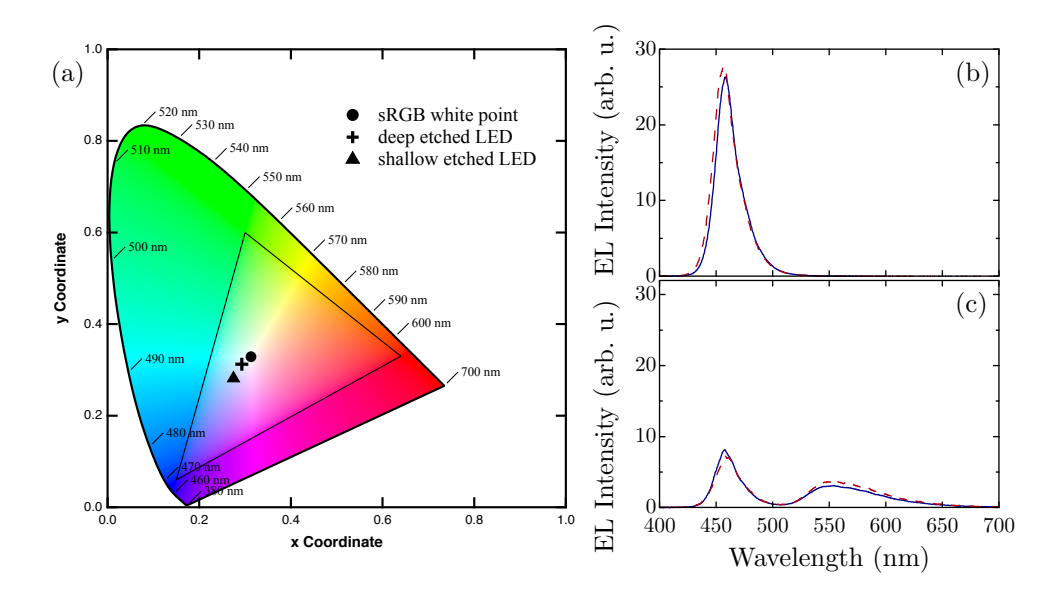
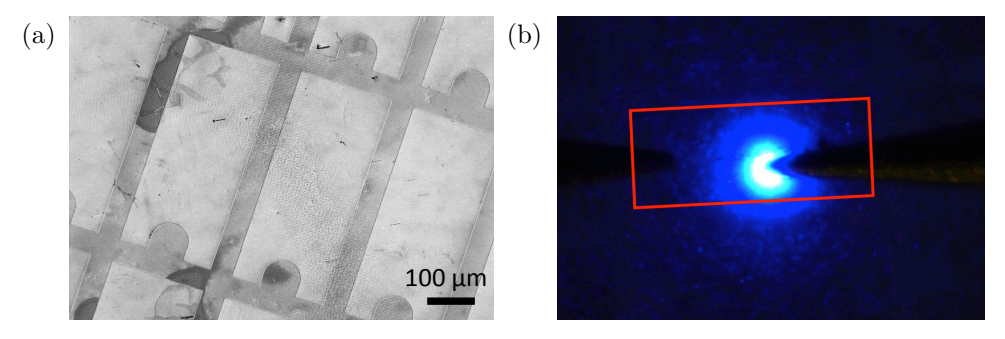


Figure 3.11 – White light emission from the shallow and deep etched LEDs covered with a layer of F8BT in a PMMA matrix. (a) CIE diagram showing the sRGB white point (circle) in relation to the white emission from the shallow etched and deep etched LEDs (triangle and cross respectively). (b) and (c) show the electroluminescence spectra of the shallow and deep etched LED before and after coating with the F8BT/PMMA layer, respectively. Red interrupted curves: shallow etched LED. Blue solid curvesdeep etched LED.

took only two iterations to find the correct thickness of the F8BT/PMMA layer which yields white light emission from the samples. Figure 3.11(a) shows how the white light emission from the shallow and deep etched sample relates to the sRGB white point. While the amounts of colour converting material is the same for both samples, the deep etched LED shows, as expected, stronger emission from the F8BT and as a consequence the white emission moves closer from the blue side of the CIE diagram towards the white point in its centre. The enhancement of the colour conversion can also be seen directly in the emission spectra of the shallow and deep-etched LED covered with the F8BT/PMMA blend. These are shown in Fig. 3.11(b) and (c). In the deep etched sample the emission from the F8BT layer is slightly enhanced and thus leads to a better balanced, more "white" emission than from the shallow etched sample. The fact that the enhancement is only small could be explained by the presence of PMMA. In the blend it separates the F8BT molecules further from the QW and in Ref. 67 it was found that it can prevent excitonic energy transfer. The combination of these two detrimental side effects cannot be compensated for by the advantageous insulation that the PMMA matrix offers between the InGaN and the F8BT.

#### 3.3.5 Shortcomings of the third generation of LED wafers

The third generation wafer, made for electrical characterisation, features a metal layer on the top surface that is only tens of nanometres thin and insufficient to make good contact to the underlying LED. It is suspected that it was accidentally removed from larger parts Chapter 3 Conclusions



**Figure 3.12** – Single LED chips on the third generation wafer. (a) SEM image of the wafer. (b) Electroluminescence from a single LED chip.

of the wafer in other processing steps and thus this sample generation does not resolve the difficulties related to making electrical contact to the wafer. This iteration of the sample finally features individually separated LED chips which can be contacted and operated separately. Figure 3.12 shows the individual LED chips on the wafer. In the SEM image on the left the photonic crystal pattern cannot be resolved clearly. Instead only a disturbance in the centre of the image indicates the presence of a periodic hole pattern on the surface. The hole pattern is successfully resolved on the corresponding high magnification image in Fig. 3.2(c).

The experiments with this sample did not lead to any meaningful conclusions because only one sample was supplied and it is unknown whether it features surface passivation and if the holes were deep or shallow etched into the surface. This prohibits any comparative studies, and due to the poor electrical connectivity an absolute quantification of the total colour conversion efficiency can still not be performed.

#### 3.4 Conclusions

The study of hybrid LEDs constituting blue emitting InGaN/GaN QWs and F8BT as a yellow emitting colour converting layer lead to a series of results that together justify further research on organic polymers for real world white light emitting LEDs. However, these devices will likely rely solely on radiative pumping of the colour converter because the short range nature of resonance energy transfer does not seem to be compatible with the constraints of manufacturing energy transfer efficient devices that suffer only marginally from unwanted non-radiative carrier recombination at their interfaces. It could be shown that a deep etched photonic crystal on the LED wafer enables efficient resonance energy transfer, especially when the holes of the photonic crystal are densely packed and the spectral overlap between energy donor and acceptor material is good. However, enabling resonance energy transfer and thus more efficient pumping of the colour converting layer comes at the cost of a decreased quantum yield. A comparative study revealed that a surface passivation step with H<sub>3</sub>PO<sub>4</sub> after etching the photonic crystal does indeed heal the sample and prevents undesired non-radiative recombination

Chapter 3 Conclusions

of carriers. However, this step also nearly completely disables the energy transfer process, likely as a consequence of the introduction of an insulating layer on the sample surface which is too thick to support the near field energy transfer process. The unpassivated deep etched samples show strong photoluminescence quenching after addition of F8BT as an energy transfer acceptor to the system. The effect of energy transfer is also confirmed in electroluminescence measurements where the colour conversion of the deep etched LED is 10 % higher than that of the shallow etched counterpart. The accuracy of these measurements is fundamentally limited due to the poor conditions for electrical contact with the samples and it is hoped that future iterations of the samples will finally feature metallic contacts. Further electroluminescence measurements with F8BT in a PMMA matrix as a colour converting layer prove that this material in combination with a blue emitting LED wafer can indeed yield white light emission and is thus technologically relevant. A direct comparison of the emission from the shallow etched and deep etched sample showes that colour conversion is enhanced in the latter. It it is also found, that PMMA is not a suitable host matrix for the polymer F8BT if resonance energy transfer is to be employed, as it tends to hinder excitonic energy transfer and exciton diffusion.

In terms of applications in devices, the ultimate evidence for an enhancement of the total colour conversion efficiency (electrical to optical power) remains to be presented. This is due to a lack of suitable samples that allow electrical measurements under standard conditions. Given the multiple iterations through different sample generations the persisting lack of suitable samples for accurate electrical measurements is seen as an unfortunate outcome to this series of experiments which were leading to an electrically operated, resonance energy transfer enabled hybrid LED. Altogether, the study shows that the detrimental effects caused by enabling resonance energy transfer by far overweight the increased efficiency of pumping the first few nanometres of the colour converting layer. It is the near field nature of the process that sets fundamental limits to its application. The next chapter is dedicated to an investigation on how to increase the characteristic range for resonance energy transfer from QW excitons.



# Dependence of Resonance Energy Transfer on Exciton Dimensionality

In this chapter we study the mechanism that governs resonance energy transfer from excitons in a QW to an organic overlayer. Energy transfer can be employed in hybrid inorganic-organic LEDs to efficiently pump a colour converter in the form of a colourtuned mixture of different organic dyes and/or colloidal QDs [22, 23, 26]. The work presented here makes use of the theoretical framework presented by Basko et al. [29] to calculate the dynamics of resonance energy transfer from QW excitons. According to Basko et al. so called free excitons and localised excitons have to be considered separately, the latter being a consequence of the imperfections in a real world QW. From our experiments it is evident that in this geometry resonance energy transfer features a distinct non-monotonous temperature dependence. We argue that this dependence stems from a temperature dependent balance between localised and free excitons in the QW. Our theoretical model [1, 2] provides a quantitative explanation for the experimentally observed data and allows us to draw conclusions on how to exploit the underlying mechanism for the optimisation of energy transfer in LEDs. In view of this application we study a material system that has the potential to be used in the commercial fabrication of such devices.

#### 4.1 Materials and methods

#### 4.1.1 Material system

The hybrid configuration studied here consists of a single GaN QW between Al<sub>0.16</sub>Ga<sub>0.84</sub>N barriers which is covered by an overlayer of the green emitting polyfluorene Poly(9,9-dioctylfluorene-co-benzothiadiazole) (F8BT) end-capped with 2,5-dimethylphenyl. The

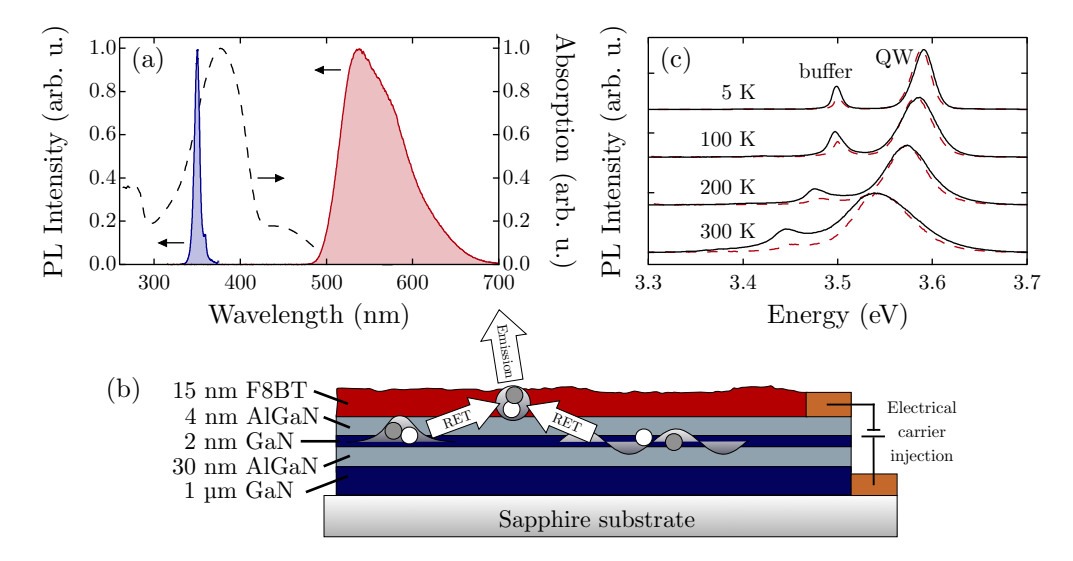


Figure 4.1 – Hybrid inorganic-organic material system for a hybrid LED employing resonance energy transfer. (a) Spectral overlap between the QW emission (blue line) and the polyfluorene absorption (black interrupted line). Red dotted line: polyfluorene emission spectrum. (b) Schematic of a hybrid LED consisting of a GaN QW and an organic colour converter. The actual sample studied here does not feature electrical contacts and excitons are injected into the QW by means of optical excitation. (c) Spectral broadening and shift of the QW emission spectrum with increasing temperature. Black solid line: without polyfluorene; red interrupted line: with polyfluorene. The emission spectra show a contribution from the 1  $\mu$ m thick GaN buffer layer.

thickness of the QW and the capping layer is  $L_{\rm w}=2$  nm and  $L_{\rm b}=4$  nm, respectively. This variant of F8BT was purchased from American Dye Company, Canada under the product code ADS233YE. Non-radiative resonance energy transfer from the QW to the polyfluorene layer is enabled by the combination of a thin capping layer and a good spectral overlap between the QW emission and the polyfluorene absorption (see Fig. 1(a)). As a reminder, a good spectral overlap is not only a requirement for radiative energy transfer, but also for non-radiative resonance energy transfer (see also the discussion in chapter 2.6). A schematic of the hybrid material system studied here is shown in Fig. 4.1(b). Note, that the electrical contacts shown in the schematic were not fabricated, but they are included to illustrate the electrical operation of a hybrid LED. Our study also covers control samples which feature thicker capping layers of  $L_{\rm b}=6~{\rm nm}$ and 9 nm width. As it will be discussed later, this thickness is sufficient to prohibit resonance energy transfer from the QW to the polyfluorene layer. The GaN QWs were grown on sapphire substrates by means of metal organic chemical vapour deposition at a temperature of 1050 °C using trimethyl gallium, trimethyl alluminum and ammonia as precursors. The polyfluorene was dissolved in toluene at a concentration of 20 mg/ml and spin cast onto the QW. This yields a 15 nm thin film as estimated by a contact profilometer measurement.

#### 4.1.2 Characterisation of energy transfer with time resolved spectroscopy

Due to the undoped, non-conducting AlGaN top barriers and the lack of electrical contacts our samples do not allow the observation of energy transfer under electrical carrier injection. The process can only be studied by using optical spectroscopy where excitons are injected into the QW by laser excitation and the evolution of the exciton population is probed with an optical technique. We use the third harmonics from a Ti:sapphire femto second pulsed laser (average power density ca. 50 W/cm<sup>2</sup> at  $\lambda_{\text{Pulse}} = 266 \text{ nm}$ ) with a repetition rate of 75 MHz to excite the QW. The time and energy resolved photoluminescence was recorded with a Hamamatsu synchroscan streak camera with  $\sim 2$  ps resolution to characterise resonance energy transfer from the QW at various temperatures between 5 K and room temperature. (The operation principle of a streak camera is explained in chapter 3.2.3.2.) The time integrated QW emission spectrum in the bare (QW only) and hybrid (QW-polyfluorene) configuration at different temperatures is shown Fig. 4.1(c). It can be seen that at low temperatures the linewidth is inhomogeneously broadened with a full width at half maximum (FWHM) of 25 meV at 5 K. With increasing temperature similar thermal broadening is observed for both the bare and hybrid configuration, leading to 90 and 71 meV FWHM, respectively, at room temperature. The associated shift in emission energy is 50 meV. In presence of the polyfluorene the exciton population is quenched by resonance energy transfer. The rate of energy transfer is revealed by a time resolved measurement of the QW's photoluminescence. Figure 4.2(a) shows the PL decay of the QW before and after deposition of the polyfluorene overlayer for a few selected temperatures. Such measurements are performed over an extensive range of temperatures between 5 K and room temperature. The decay rates obtained from an exponential fit to the PL decays are summarised in Fig. 4.2(b). Above 50 K the PL decay is noticeably accelerated in presence of the polyfluorene while the most pronounced quenching is found between 100 and 170 K. It should be noted that the PL decay fully recovers after removal of the polyfluorene layer, indicating that the QW PL is not quenched due damage to the surface. The 4 nm thick undoped capping layer between the QW and the organic effectively prohibits charge transfer between them and, hence, cannot account for the observed PL quenching. The two lowermost graphs in Fig. 4.2(a) show the PL decay of the QW control sample with the thicker capping layer (6 nm). The decay remains unaltered after the deposition of the polyfluorene layer. Therefore, the accelerated PL decay is attributed to resonance energy transfer mediated via the near field dipolar coupling between the excitonic dipole moment and the polarisability of the organic material. Evidence for resonance energy transfer can also be found in the PL decay of the polyfluorene, the energy transfer acceptor: energy transfer acts as an additional pumping source that can be identified and quantified from the rise time of the polyfluorene's PL dynamics. A detailed application of the respective rate equations can be found in Refs. [21, 68, 69]. Because the polyfluorene absorbs strongly at the wavelength of the laser pulse used to excite the QW ( $\lambda_{\text{Pulse}} = 266 \text{ nm}$ , see Fig. 4.1(a))

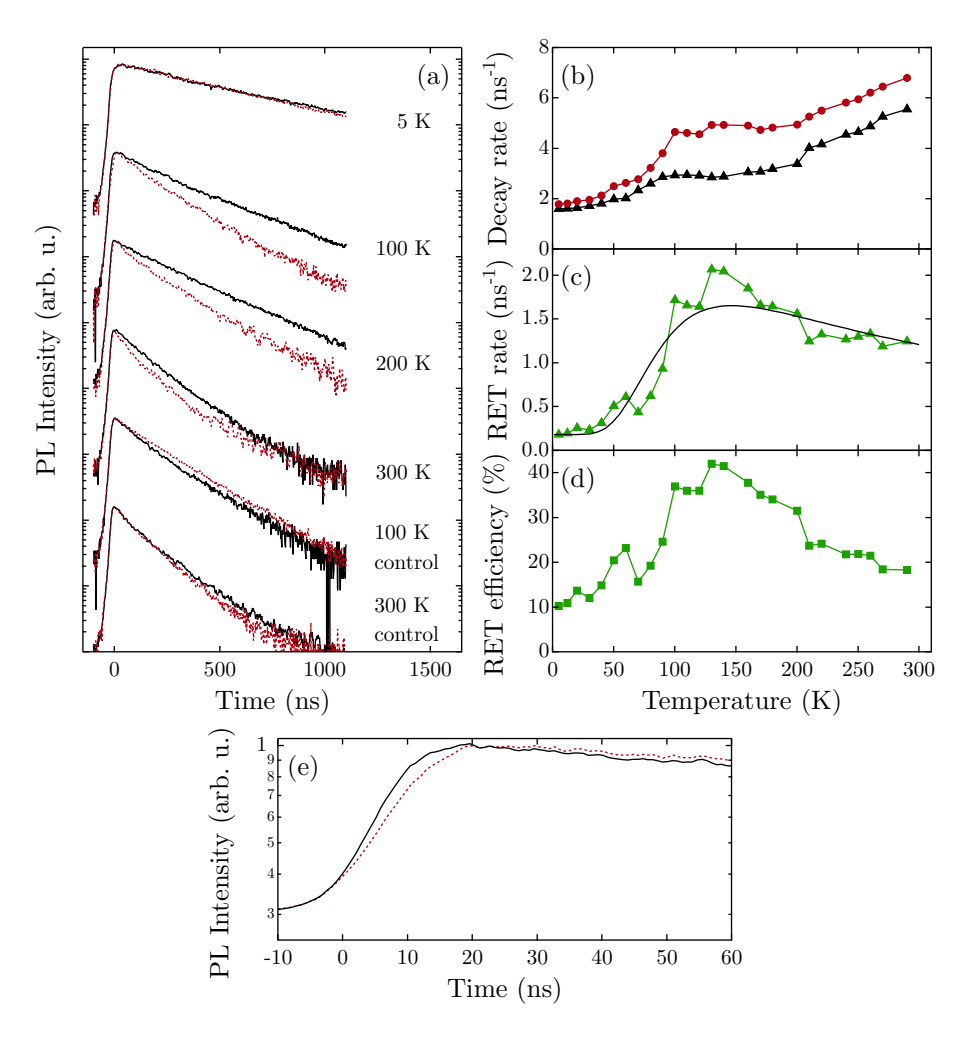


Figure 4.2 – Evidence for resonance energy transfer in the photoluminescence from the QW. (a) Photoluminescence decay of the QW before (black curves) and after (red curves) deposition of the polyfluorene at various temperatures. (b) Temperature dependence of the exciton recombination rate in the QW before (black triangles) and after (red circles) deposition of F8BT. (c),(d) Energy transfer rate and efficiency at different temperatures. The black line in (c) is the energy transfer rate calculated according to the model described in the text. (e) Photoluminescence transient of the polyfluorene deposited on samples with a 4 (red dotted line) and 9 nm (black line) capping layer.

it is also directly excited and only a small difference in the buildup of the polyfluorene's PL dynamics is expected. Indeed, Fig. 4.2(e) reveals a slightly longer rise time for the sample where resonance energy transfer is enabled. Resonant back-transfer of energy from the F8BT to the QW cannot occur because the excited state relaxation time in the polyfluorene is much shorter than the characteristic energy transfer time of a few hundred ps and, hence, the interaction occurs in the weak coupling regime [70]. However, other material systems and geometries, for example microcavities, can support the strong coupling regime where hybrid excitonic states are formed when energy is coherently exchanged between the Wannier-Mott excitons in the QW and Frenkel excitons in the organic constituent [71]. As evidenced in the presentation of Fig. 4.2(a) the PL of the QW obeys an exponential decay law and can be accurately characterised by a decay

rate  $\Gamma_{\text{tot}}$ . Different decay mechanisms contribute to the decay of the exciton population and in absence of the polyfluorene the total decay rate can be written as the sum of radiative and other non-radiative rates intrinsic to the QW,  $\Gamma_{\text{tot}} = \Gamma_{\text{rad}} + \Gamma_{\text{non-rad}}$ . When energy transfer is enabled in the presence of the polyfluorene layer the rate of RET can be quantified from the increased decay rate of the QW PL,  $\Gamma_{\text{RET}} = \Gamma_{\text{tot,hybrid}} - \Gamma_{\text{tot,bare}}$ , where the subscripts *hybrid* and *bare* denote the QW with and without the layer respectively. Given the rate of resonance energy transfer,  $\Gamma_{\text{RET}}$ , the efficiency of the process is defined as  $\eta_{\text{RET}} = \frac{\Gamma_{\text{RET}}}{\Gamma_{\text{tot,hybrid}}}$ . The temperature dependence of the total decay rates of the bare and hybrid QW, the rate of energy transfer, and the efficiency of energy transfer is summarised in Figs. 4.2(c)-(e).

The increase of the total PL decay rate of the bare QW with temperature is attributed to the temperature dependence of non-radiative recombination channels, intrinsic to the QW. This includes carrier trapping and non-radiative recombination at defect states at dislocations or AlGaN/GaN interfaces. Consequently, the quantum yield  $QY_{QW}$ , estimated from the PL decay rate, drops monotonously from an assumed 100 % at 5 K to less than 30 % at room temperature. It is found that the rate and efficiency of energy transfer do not follow a monotonous trend, but show a pronounced maximum around 130 K where the transfer of excitons from the QW to the organic material reaches a maximal efficiency of 43 % (Fig. 4.2(c),(d)). Our group has previously performed similar experiments over a smaller temperature range up to 130 K on a QW that was coated with QDs instead of an organic material [72]. Also in these experiments it was found that the energy transfer rate keeps increasing up to 130 K but it remained undecided how the energy transfer rate changes above this temperature.

# 4.2 Resonance energy transfer dynamics of quantum well excitons

In this section we will develop the ansatz to understand the experimentally observed non-monotonous temperature dependence of energy transfer. Starting point is a review of the theory of energy transfer from QW excitons developed by Basko et al.. At first, let us recollect Förster's original theory from which it follows that the rate of resonance energy transfer is not explicitly temperature dependent but that it is proportional to the fluorescence decay rate of the donor and the sixth power of the donor's quantum yield [46]. Any particular, non-monotonous temperature dependence of the energy transfer rate and efficiency would originate from non-monotonous changes of the donor's fluorescence properties with increasing temperature. As this is not seen in our experiment, another theoretical framework is needed to describe the energy transfer process. Förster's theory of energy transfer considers electronic excitations in the form of bound Frenkel excitons at individual molecular sites. In contrast, the electronic excitations found in a crystalline inorganic semiconductor QW are propagating Wannier-Mott excitons characterised by

a wave vector  $\mathbf{k}$ . With regard to the planar configuration of a QW and an organic overlayer it is known that the dipolar coupling between two planes separated by distance d scales with

$$V(k,d) \propto ke^{-kd},\tag{4.1}$$

where k is the magnitude of the relative in-plane wave vector  $\mathbf{k}$  [29]. Basko et al. showed that the resulting non-monotonic dependence of the dipolar coupling on the wave vector gives rise to a strong dependence of energy transfer on exciton localisation in real space. The general approach to calculate the rate of energy transfer for a donor-acceptor system was outlined in chapter 2.6. Following the theoretical approach by Basko et al. the rate of energy transfer from QW excitons in the linear regime to a bulk epilayer of organic molecules [29] or QDs [73] is calculated by applying Fermi's golden rule to the interaction of the electric field produced by the QW polarisation with the polarisability of the polyfluorene. For that purpose the polyfluorene's properties can be summarised by the macroscopic complex dielectric function which originates from the detailed electronic level structure of the organic molecules. It can be shown that either can be used to calculate the rate of energy transfer [29].

#### 4.2.1 Free excitons

Let us first consider a free exciton, subject only to the confinement in the growth direction and moving freely in the QW plane. The exciton's centre of mass motion is then characterised by an in-plane wave vector k that depends on the kinetic energy of the exciton and the exciton's envelope wave function has the form of a plane wave. The exciton is further described by the 2D in-plane exciton Bohr radius  $a_{\rm X,B,2D}$  and the exciton's optical properties are summarised by the dipole moment between the conduction and valence band  $d_{vc}$ . From equation 4.1 it can be understood that the energy transfer rate for a free exciton is expected to be small for both very small and large wave vectors while it is maximum for some intermediate value of  $k = |\mathbf{k}|$ . The explicit dependence of the RET rate on the magnitude of the exciton wave vector shall not be reproduced here because the shape of the resulting curve is not apparent from the equation alone. The derivation of the explicit expression is explained in great detail in the original work by Basko et al. [29]. However, it is instructive to look at the plot of the wave vector dependence of the energy transfer rate for a free exciton in our material system as it is shown in Fig. 4.3. The behaviour from the two plane model is indeed reproduced and it can be seen on the double logarithmic plot that the dependence is non-monotonous, non-linear and that the energy transfer rate drops rapidly for large wave vectors. This can be qualitatively understood by considering that for large wave vectors the evanescent field of the exciton polarisation decays very fast, and thus little interaction with the overlayer can be expected. The behaviour for very small wave vectors originates from the fact that the exciton charge density serves as a source term for the polarisation. A slow in-plane oscillation of the exciton charge density yields a small gradient and thus

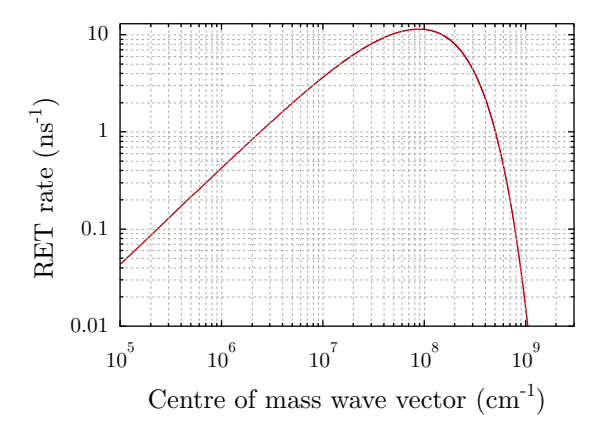


Figure 4.3 – Dependence of the energy transfer rate on the exciton wave vector. The graph is calculated with the parameters of the AlGaN/GaN and F8BT material system used for study in this chapter.

a small polarisation, which in turn results in a low interaction strength for resonance energy transfer.

For an ideal QW it would suffice to consider the Boltzmann distribution of a thermalised ensemble of free excitons to obtain a non-monotonous dependence of the energy transfer rate on temperature. At both low and high temperatures the majority of excitons occupies states below or above the wave vector that yields efficient energy transfer. Real world QWs suffer from imperfections in the QW potential, especially when made of AlGaN/GaN. As a result, a substantial fraction of excitons can be trapped in the potential disorder of the QW and, as we will see in the next paragraph, their energy transfer dynamics will be distinctly different from their free counterparts.

#### 4.2.2 Localized excitons

Localised excitons in a QW are effectively zero-dimensional and have more similarity with QD excitons than with free 2D excitons. However, their in-plane wavefunction can be decomposed into plane waves with an average wave vector of zero. Figure 4.4 shows schematically the potential disorder along with the wave functions of a localised and free exciton. For simplicity, the in-plane potential trap experienced by a localised exciton is approximated as being harmonic and isotropic. The in-plane wavefunction of the ground state is then a gaussian function, which in turn yields a gaussian function for the Fourier decomposition into plane waves of different wave vectors. The localisation length  $L_{\rm loc}$  is a measure for the spatial extent of the exciton wave function in the QW plane and, evidently, a small localisation length goes along with a broad distribution of wave vectors. As a consequence from the discussion in the previous paragraph, the dependence of the energy transfer rate on the localisation length  $L_{\rm loc}$  is non-monotonic and shows a distinct resonance. The explicit expression for the dependence of the energy transfer rate on the localisation length is not reproduced here. It is discussed thoroughly in Ref. [29].

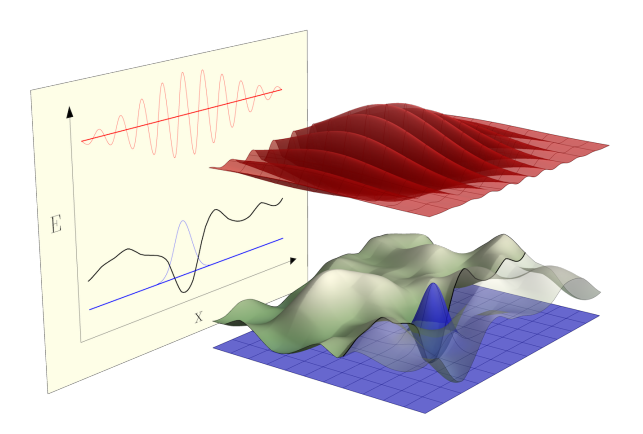


**Figure 4.4** – Schematic of the potential landscape experienced by excitons in an imperfect QW. The potential landscape is drawn in shaded green. Also shown are the wavefunctions of an exciton trapped in a local minimum (blue) and a free moving exciton at a higher energy (red). Resonance energy transfer from excitons in the quantum well to an overlayer of organic dyes is governed by the excitons' dimensionality.

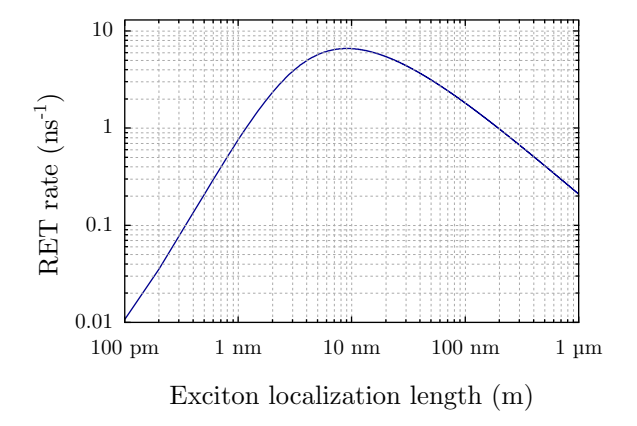


**Figure 4.5** – Dependence of the energy transfer rate on the exciton localisation length. The graph is calculated with the parameters of the AlGaN/GaN and F8BT material system used for study in this chapter.

Instead, we refer to Fig. 4.5 for a plot of the dependence for our material parameters. Note that localisation lengths well below a few nanometres are not physically relevant, because the respective confinement energy makes them energetically unfavourable. In order to link the populations of localised and free excitons we introduce a typical potential trap depth  $V_{\rm trap}$  that acts as a threshold energy which a localised exciton has to overcome to propagate freely. With increasing temperature we can expect a transition from localised to free excitons and a signature in the temperature dynamics of resonance energy transfer. The occurrence of localised excitons will depend on the potential disorder and hence some characterisation of the random potential disorder is required. An accurate description of the potential disorder and its origins goes beyond the scope of this thesis and cannot be given without further knowledge, but an approximation can be attempted. We assume that the potential disorder can be described by three characteristic parameters: the typical localisation length  $L_{\rm loc}$  (which in the case of a distribution of localisation lengths takes the place of an average localisation length), the

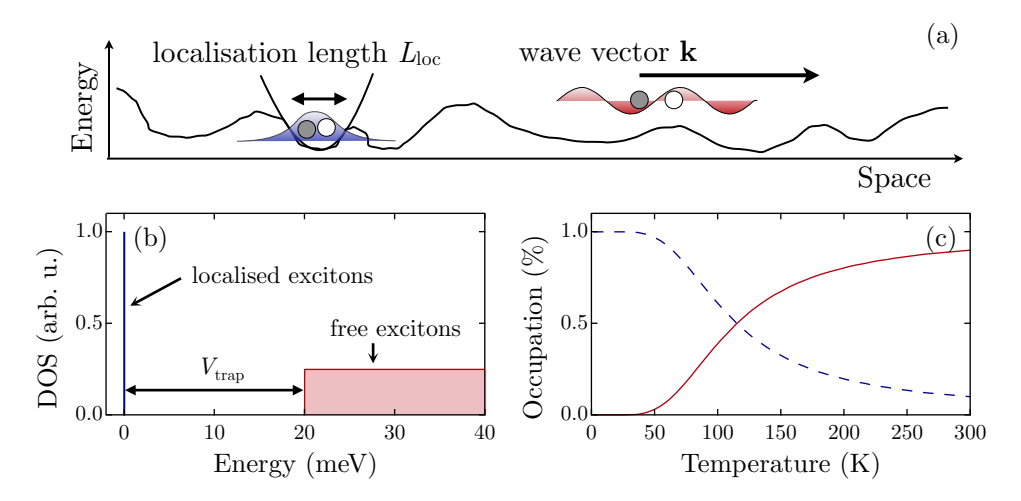


**Figure 4.6** – Distribution of excitonic states in the imperfect QW. (a) Schematic of the potential fluctuations experienced by excitons in the QW. (b) Density of states composed of a delta function at low energies for localised excitons and a flat contribution above an energy threshold for free excitons (relative contributions not drawn to scale). (c) Relative population of localised (blue interrupted line) and free (red line) excitons vs temperature.

typical potential trap depth  $V_{\text{trap}}$  and the area density  $\rho_{\text{trap}}$  of traps in the QW plane. In the next section it will be shown how these parameters determine the temperature dependence of resonance energy transfer.

#### 4.2.3 Energy transfer in the exciton ensemble

After excitation with the laser pulse the exciton population thermalises and the distribution of excitons among localised and free states is determined by the Boltzmann factor and the density of states (DOS). Localised and free excitonic states contribute differently to the DOS: free exciton states contribute with a constant DOS above  $V_{\rm trap}$ , whereas localised exciton states contribute with a weighted delta function at E=0. In this approximation only the first subband with the lowest quantum number in respect to the vertical confinement is considered. Figure 4.6(a)+(b) show a schematic plot of the potential landscape and the resulting DOS. The absolute value of the DOS for free excitons is given by eq. 2.4 while the weight of the delta function representing the localised states is determined by the area density  $\rho_{\rm trap}$  of potential traps. Energy transfer from free electrons and holes is not included in our model because at this low excitation density their population is very small and thermalisation of electrons and holes into excitonic states occurs within their characteristic energy transfer time [29]. Moreover, the large exciton binding energy in GaN (23 meV in bulk and 92 meV in an infinitely thin QW) prohibits exciton dissociation at the temperatures from our experiments.

For the exciton ensemble we define an average rate of energy transfer at temperature T as [1]

$$\langle \Gamma_{\text{RET}} \rangle (T) = \frac{1}{Z(T)} \int_0^\infty \Gamma_{\text{RET}}(E) DOS(E) e^{-\frac{E}{k_{\text{B}}T}} dE,$$
 (4.2)

where Z(T) is the partition function,  $k_{\rm B}$  is Boltzmann's constant, and the integration is performed over energy. For the computation of the integral  $\Gamma_{RET}$  is calculated for localised and free excitons as outlined above. Because the control sample with a 6 nm thick capping layer did not show PL quenching upon addition of the F8BT layer, it is justified to approximate the 15 nm thick F8BT layer found on our samples as an infinitely thick polarisable layer in line with the formalism from Ref. [29]. Energy transfer from excitons in the QW is mediated via the excitonic dipole moment both in (L) and out (Z) of the QW plane. The corresponding rates differ at most by a factor of 3 and here their average is taken. The energy transfer rate  $\Gamma_{RET}$  depends on a number of material parameters that are briefly summarised in the following. The dipole moment  $d_{vc}$  for the transition between the conduction and valence band goes into the energy transfer rate with its magnitude squared. It is obtained from the Kane energy via the relation  $|d_{vc}|^2 = e^2 \hbar^2 E_0 / (2m_0 E_{gap}^2)$ , where  $E_0 = 14 \text{eV}$  is the Kane energy,  $E_{\rm gap} = 3.502 \; {\rm eV} - 0.79 \times 10^{-3} \; {\rm eV/K} \times T^2 / (T + 1000 \, {\rm K})$  is the temperature dependent band gap of GaN,  $m_0$  is the free electron mass and e the electron charge [74]. For a GaN QW embraced by AlGaN barriers the dipole moment  $d_{vc}$  is reduced due to the internal electric field in the heterostructure [75]. In a single QW we account for this effect by the reduction of the dipole moment by a factor of  $\sqrt{0.63}$ , a smaller correction than that expected for a superlattice according to Ref. [75]. The exciton Bohr radius in the QW is approximated at  $a_{X,B} = 3$  nm [76], and the translational mass of the exciton is taken as the sum of the effective masses of the electron  $(m_e = 0.2 \cdot m_0)$ and hole  $(m_h = 1.3 \cdot m_0)$  [74]. The dielectric constant of GaN is set to 9.5, and the optical properties of the F8BT at the resonance energy of the QW are approximated to be independent of temperature and isotropic. They are described with the dielectric function  $\epsilon_{350\text{nm}} = 2.9 + 0.5i$  [77]. It has been reported that thin films of F8BT indeed show birefringence due to alignment of the long molecules parallel to the surface [77], but this effect can be neglected for the non-resonant excitation at 350 nm considered here because it is only dominant at the  $\pi - \pi^*$  transition. In certain cases, for example when the organic overlayer is crystalline or the transition energy lies close to the resonance of the organic material the anisotropy of the material has to be considered. Kawka and La Rocca have provided a specialisation of the formalism from Basko et al. that accounts for anisotropy in the optical properties of the organic layer [78].

## 4.2.4 Comparison between experiment and simulation

Equipped with an expression for the average rate of resonance energy transfer in the exciton ensemble at a given temperature and the relevant material parameters we are in a position to compute equation 4.2 and compare the result directly with the experimentally observed temperature dependence from Fig. 4.2. The three parameters that remain unknown a priori and are thus allowed to be adjusted to yield a good match are the characteristic parameters which together describe the potential disorder: the localisation

length  $L_{\rm loc}$ , the potential depth  $V_{\rm trap}$  and the number of potential traps per area,  $\rho_{\rm trap}$ . The best matching simulated curve is shown as a solid line along the experimental data in Fig. 4.2(c). The simulated curve reproduces well the characteristics of the experimental data: at low temperatures up to 50 K the energy transfer rate remains nearly constant and depends solely on the localisation length of the localised excitons. The energy transfer rate peaks at 130 K where the efficiency of the process reaches 43 %before it decreases again for higher temperatures. At room temperature the efficiency of energy transfer is approximately 18 %. Figure 4.6(c) shows the calculated occupation probability for localised and free excitons over the entire temperature range. It can be seen that below 50 K the majority of excitons are localised, which is in agreement with an unchanging energy transfer rate in this temperate range. A small value of  $L_{\rm loc} = 0.9$ nm yields a corresponding energy transfer rate of 0.23 ns<sup>-1</sup>. Given an in-plane lattice constant for GaN of 0.32 nm, this localisation length corresponds to approximately 9 lattice sites in the QW plane, and suggests that excitons are trapped in the potential disorder and not at individual impurity sites. According to calculations by Gallart et al., the estimated value for  $L_{loc}$  is comparable to the average spacing between Al atoms in the AlGaN barriers ( $\approx 2 \text{ nm}$ )[76]. When the temperate is elevated to 50 K or greater a substantial fraction of excitons acquires adequate thermal energy to overcome the energy threshold for escaping the traps and undergoes energy transfer with a rate depending on their wave vector. With a trap depth of  $V_{\text{trap}} = 20 \text{ meV}$  and an area density of potential traps of  $\rho_{\rm trap} = 4 \cdot 10^{11} \ {\rm cm}^{-2}$  the simulation reproduces accurately the characteristic increase and peak of the energy transfer rate above 50 K (see again Fig. 4.2(c)). The calculated relative occupation of the localised and free exciton states reveals that at 130 K, where the rate of energy transfer is maximum, the fractions of localised and free excitons are approximately equal (see Fig. 4.6(c)). Above this temperature the exciton ensemble is dominated by free excitons and the rate of energy transfer decreases again because their wave vectors become too large for efficient dipolar coupling.

#### 4.2.5 Comparison of radiative and non-radiative energy transfer

The discussion of energy transfer in the hybrid organic-inorganic device would be incomplete if we only considered non-radiative resonance energy transfer. In addition, radiative energy transfer also offers a channel for transferring electronic excitations from the QW to the organic layer. This process relies on the emission of a photon from the QW and subsequent absorption of the same to finally yield an electronic excitation in the organic overlayer. In contrast to non-radiative energy transfer, the efficiency of radiative energy transfer scales with the quantum yield  $QY_{\rm QW}$  of the QW. In the experiment we have observed that the quantum yield drops dramatically with increasing temperature, and this will be reflected in the efficiency of radiative energy transfer  $\eta_{\rm rad}$ . The latter is the product of the probability for the emission of a photon from the QW and absorption of the same photon by the polyfluorene layer,  $\eta_{\rm rad} = QY_{\rm QW}P_{\rm F8BT}$ , where the factor  $P_{\rm F8BT}$ 

takes into account isotropic emission from the QW, Fresnel reflection of the emitted light at the GaN/F8BT interface (3.6 %), and absorption of light in the 15 nm thick polyfluorene layer. Based on these values the efficiency for radiative energy transfer at room temperature is estimated to be 2 orders of magnitude lower than the efficiency observed for non-radiative resonance energy transfer, 0.15 % vs. 22 %. This large discrepancy in the efficiencies is in agreement with the findings from another similar study by Itskos et al. [20]. These results prove that for thin film geometries non-radiative resonance energy transfer is the dominating energy transfer mechanism that easily outperforms radiative pumping of the colour converting layer. It can be exploited in hybrid organic-inorganic microcavities which can feature the hybridisation between excitons in the organic and inorganic constituents and allow coupling of the high oscillator strength and binding energy of Frenkel excitons with the optical non-linearities and high mobility of Mott-Wannier excitons [79]. However, for the application in LEDs a thin capping layer on the QW will substantially limit current injection and hinder efficient thermal management of the device. This aspect will be discussed in detail in the next section. We note, that radiative pumping of the colour converter is fundamentally limited by the low light extraction efficiencies from GaN based substrates and even a macroscopically thick layer of polyfluorene on the order of a few microns can only absorb the few photons that are leaving the solid state substrate. As mentioned in chapter 3 one common approach to improve light extraction from an LED is to impose a photonic crystal structure on the surface which effectively couples the waveguided light modes with free space modes. In chapter 3 it was shown that such a LED design with thick current injection layers and a photonic crystal can be used in conjunction with energy transfer pumping of a colour converter deposited into the holes of the photonic crystal. However, resonance energy transfer is only enabled when the holes of the photonic crystal penetrate sufficiently deep through the multiple QWs and reveal an interface with the QWs [21]. Because this process is detrimental to the quantum yield of the QWs, enabling resonance energy transfer comes at the cost of lower device performance.

## 4.3 Optimization of resonance energy transfer

In this section we will explore a few possibilities to optimise resonance energy transfer in planar geometries for the application in hybrid LEDs. According to Förster's theory of resonance energy transfer between molecules the coupling depends crucially on the separation distance and scales with  $\frac{1}{r^P}$  where r is the distance between energy transfer donor and acceptor, and P=6 for two molecules represented as point dipoles. The exponent reduces to P=4 for the case of a point dipole that couples to a plane of acceptors and for two planes of dipoles coupling to each other the exponent reduces further to P=2. Although the application of this formalism to QW excitons and an organic layer is crude and incomplete, it has been reported that the best match with

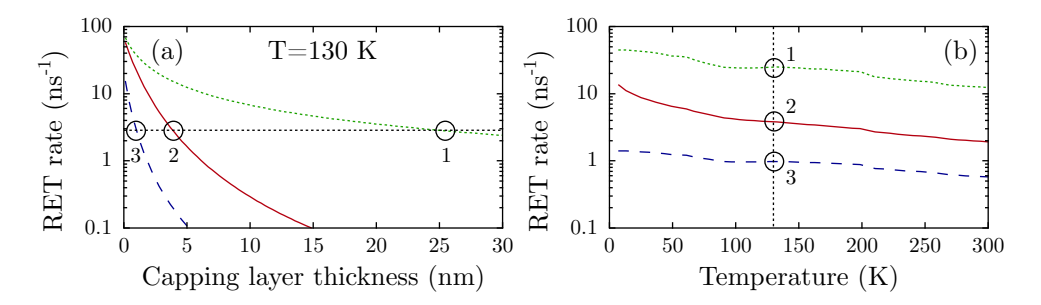


Figure 4.7 – Förster radii of QW excitons. (a) Calculated energy transfer rate for localised excitons (blue interrupted line) and free excitons (red line) at 130 K for varying thickness of the capping layer. The dotted green line corresponds to the energy transfer rate of an exciton with the optimum wave vector for each capping layer thickness. The thin horizontal line marks the exciton decay rate  $\Gamma_{tot}$  at 130 K without energy transfer. (b) Temperature dependence of the Förster radii of localised (blue interrupted line), free (red line) and excitons with the optimum wave vector (green dotted line).

experimental data from a configuration similar to the one considered here was found for P=2, indicative of plane-to-plane coupling in terms of the Förster theory [20]. The distance where the energy transfer rate equals the sum of all other decay rates is traditionally referred to as Förster radius and we shall employ the same definition here. For molecular optical dipoles the Förster radius is usually between 1 and 5 nm, rendering energy transfer inefficient for larger separation distances. However, we find that under certain conditions QW excitons can feature Förster radii up to several tens of nanometres. The actual dependency of the rate of energy transfer on the separation between the QW plane and the organic material cannot be described with a simple expression like the one above. Instead, the more accurate framework outlined throughout this chapter should be applied. To underline the effect of the exciton dimensionality on the Förster radius, we split the exciton ensemble into two sub ensembles of localised and free excitons and calculate their Förster radii separately. Moreover, we also calculate for each capping layer thickness the energy transfer rate of an exciton with the optimum wave vector that yields the highest rate. The results are shown in Fig. 4.7(a) where the sub ensemble of free excitons is considered at a temperature of 130 K. It can be seen that the energy transfer rate for localised excitons drops faster with increasing capping layer thickness than for free excitons. Moreover, the resonant excitons sustain a high energy transfer rate for much thicker capping layers. Figure 4.7(a) also indicates the decay rate of the exciton ensemble at 130 K by a horizontal interrupted line. The Förster radii for the different cases are found at the intersections between the graphs and the horizontal line. At a temperature of 130 K where  $\langle \Gamma_{RET} \rangle$  (the average rate of energy transfer in the exciton ensemble) is the highest the Förster radii for the three cases are: 1 nm for localised excitons, 4 nm for the sub ensemble of free excitons and 25 nm for excitons with the optimum wave vector. The same procedure is used to compute the complete temperature dependence of the Förster radii. It is shown in Fig. 4.7(b) where it can be seen that the optimally tuned excitons yield a Förster radius of 12 nm at room temperature. This value is one order of magnitude larger than for a complete exciton ensemble at 130 K which consists of 50 % free excitons with a Förster radius of 4 nm and 50 % localised excitons with a Förster radius of 1 nm. In order to exploit the advantageous energy transfer properties of the excitons with a optimised wave vector the DOS needs to be enhanced for this particular wave vector and resonant excitons need to be produced within the exciton ensemble. In principal, this could be achieved by optical injection via a coupling grating configuration which also acts a a periodic potential modulation for the QW potential. Such a device, which is tuned to resonance with the optimum exciton wave vector, might hold the potential to resolve the compromise between a thick and a thin capping layer; the former can support a reasonable electrical current, but yields a low energy transfer rate, and the latter is too thin to carry substantial current, but yields a high transfer rate. Admittedly, this finding might be difficult to implement in commercial applications like the LED wafers studied in chapter 3.

Another possibility to improve the efficiency of energy transfer under the operating conditions of a real world device is to manipulate the balance between localised and free excitons. We saw that by enabling the excitons to move freely and with the optimum wave vector the rate of energy transfer can be increased by over an order of magnitude compared to point-like localised excitons. In devices this can be exploited by variation of the potential trap depth  $V_{\rm trap}$ , the density  $\rho_{\rm trap}$  and the localisation length  $l_{\rm loc}$  of such traps. In general, more and deeper potential traps will increase the temperature at which excitons start to move freely. As a result, the maximum of the graph in Fig. 4.2(c) could be shifted from 150 K to higher temperatures. Indeed, this trend can be identified in the computed graphs from Figs. 4.8(a) and (b) where the effect of the parameters  $V_{\text{trap}}$  and  $\rho_{\text{trap}}$  on the average energy transfer rate  $\langle \Gamma_{\text{RET}} \rangle (T)$  is shown for different temperatures. In addition, Fig. 4.8(c) shows how the average rate of energy transfer at room temperature,  $\langle \Gamma_{\text{RET}} \rangle (T = 300 \text{ K})$ , is affected when  $V_{\text{trap}}$  and  $\rho_{\text{trap}}$  are varied. It can be seen that as long as  $\rho_{\text{trap}}$  is sufficiently low, i.e. equal or less than in these samples,  $\langle \Gamma_{RET} \rangle (T = 300 \text{ K})$  reaches an approximately constant plateau over a range of trap depths because the dominating fraction of excitons becomes free at 300 K. Consequently, energy transfer can be controlled by the use of high purity materials and long annealing phases during the epitaxial growth of the heterostructure. A pronounced and high maximum in the temperature dependence of the energy transfer rate can only be achieved for relatively flat and neat potential landscapes and occurs around 30 K. However, such a nearly perfect potential landscape is not needed to yield a reasonably high energy transfer rate and efficiency at room temperature. Figure 4.8(c) shows that for a wide range of potential trap depths and trap densities an efficiency of around 23 %can be maintained. This is similar to the observed energy transfer efficiency of 18 % at room temperature for our sample.

Chapter 4 Conclusions

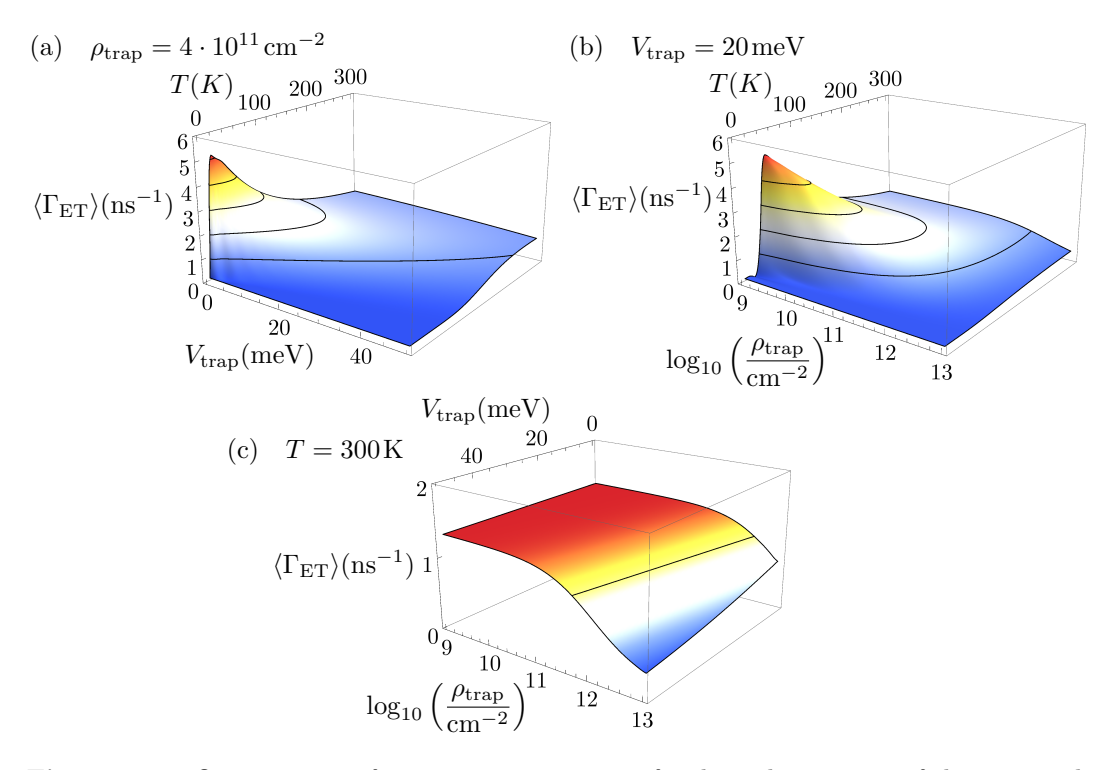


Figure 4.8 – Optimisation of resonance energy transfer through variation of the potential landscape. (a) Dependence of the average rate of resonance energy transfer in the exciton ensemble,  $\langle \Gamma_{\text{RET}} \rangle$ , on the temperature and the trap depth  $V_{\text{trap}}$ . (b) Dependence of  $\langle \Gamma_{\text{RET}} \rangle$  on the temperature and the trap density  $\rho_{\text{trap}}$ . (c) Dependence of  $\langle \Gamma_{\text{RET}} \rangle (T=300 \text{ K})$  on  $V_{\text{trap}}$  and  $\rho_{\text{trap}}$ .

## 4.4 Conclusions

In summary, we have studied the dependence of resonance energy transfer from QW excitons to a polyfluorene overlayer on exciton dimensionality. Localised and free excitons show different energy transfer dynamics which are determined by their localisation length and wave vector, respectively. In the AlGaN/GaN QW under investigation the potential landscape experienced by excitons in the QW features a considerable density of potential traps that capture excitons at temperatures below 50 K. In our experiments the ratio between localised and free excitons is controlled by tuning the temperature of the exciton ensemble. With increasing temperature the fraction of excitons which escape traps in the potential landscape and become free increases. We find a maximum efficiency of resonance energy transfer of 43 % at 130 K. At room temperature the efficiency drops to 22 %, which is still 2 orders of magnitude larger than the efficiency of radiative energy transfer for this configuration. The temperature dependence of resonance energy transfer is effectively determined by three characteristic parameters which describe the potential disorder in the QW: the characteristic exciton localisation length  $L_{\rm loc}$  for localised excitons, the trap depth  $V_{\rm trap}$  that localised excitons have to overcome to move freely, and the density  $\rho_{\text{trap}}$  of such traps in the QW. In principle, these parameters can be influenced by the growth conditions. Based on simulations we present

examples how this could be exploited to yield higher energy transfer efficiencies at a defined temperature. Energy transfer can be further enhanced by tuning specifically the exciton wave vector through manipulation of the density of states and a resonant excitation scheme. This approach exploits the fact that for a optimum wave vector excitons undergo energy transfer on a length scale of tens of nanometres, whereas it is only a few nanometres for localised excitons. Each of these approaches, or even the combination, could be used to enable energy transfer in LEDs where a too thin capping layer would prohibit the electrical injection of carriers, and a too thick capping layer would prohibit efficient transfer. Our findings encourage the experimental realisation of a hybrid LED or microcavity structure that is designed to support the propagation of excitons at the wave vector which yields the optimum resonance energy transfer rate. The findings and conclusions about the wave vector dependence in this chapter rely on the indirect experimental evidence obtained through the temperature dependence and on the results of the simulation. Because the wave vector dependence of resonance energy transfer has not been explicitly measured, yet, we pursued this aim in a rigorous experimental approach of which the results and conclusions will be given in the next chapter.

#### 4.5 The author's contribution

The measurements with the streak camera discussed in this chapter were performed by Dr. Galia Pozina at the University of Linköping. My own contribution to the acquisition of the experimental data was the coating of the QW samples with F8BT. The ansatz for the physical model concerning the temperature activation of free excitons and all simulations in this chapter were developed and tested by me, Jan Junis Rindermann.



# Dependence of Resonance Energy Transfer on Exciton Wave Vector

In the previous chapter we studied resonance energy transfer from a thermalised exciton ensemble in a GaN quantum well to an overlayer of the polyfluorene F8BT. This chapter covers the continuation of the project with a rigorous attempt to probe directly the dependence of the rate of resonance energy transfer on the magnitude of the exciton wave vector. In contrast to the experiment from the previous chapter, here, we do not rely on the thermalisation of the exciton ensemble to study the *average* rate of energy transfer based on the temperature dependent occupation of excitonic states with different wave vectors. We rather design and perform a pump probe experiment that potentially allows to measure directly changes of the rate of energy transfer with increasing magnitude of the exciton wave vector. Moreover, angle resolved photoluminescence is employed in an attempt to obtain the desired dependency.

#### 5.1 Materials and methods

#### 5.1.1 Single AlGaAs/GaAs quantum well

The sample used for this series of experiments is the sample NU2601 fabricated by Prof. Mohamed Henini at the University of Nottingham. It is a single GaAs quantum well of 6.5 nm thickness with Al<sub>0.35</sub>Ga<sub>0.65</sub>As barriers, where the widths of the inner and outer barrier is approx. 20 nm and 7.5 nm, respectively. The heterostructure is grown on top of a 500 nm thick GaAs buffer layer on a (100) GaAs substrate. Other pieces of this sample were successfully used in a previous study on resonance energy transfer by my predecessor Dr. Soontorn Chanyawadee [56, 68]. In the previous study it was

proven that the relatively thin outer barrier of the QW enables efficient resonance energy transfer from the QW to an organic overlayer on the sample.

#### 5.1.2 PbS quantum dots

For this experiment we chose to use PbS QDs instead of an organic absorber as the energy transfer acceptor. This is due to the difficulty to obtain and prepare an organic material that can strongly absorb in the infrared and hence support strong resonance energy transfer from this QW. For this QW the transition of the heavy hole exciton lies at 796 nm at 10 K. The PbS QDs provide both, a strong absorption coefficient at this energy and an easy sample preparation by spin coating a thin film onto the QW sample. In contrast to organic materials, the QDs were readily available from other experiments in the research group, like the ones performed by Dr. Peristera Andreakou [80]. The particles were synthesised in the group of Prof. Gerasimos Konstantatos from The Institute of Photonic Sciences, Barcelona following the recipe and procedure from Ref. 81.

#### 5.1.3 Pump-probe reflection technique

The understanding and discussion of the potential as well as difficulties of the experiments in this chapter requires familiarity with the so called pump-probe reflection technique. This variation of pump-probe spectroscopy allows to measure the temporal evolution of a population of photo-excited excitons in the quantum well. It is based on the measurement of a change in reflection of a laser pulse (probe) from the sample induced by a population of excitons created by a preceding laser pulse (pump). The absorption and reflection of the second pulse is determined by the number of carriers that have already undergone an interband transition into the conduction band due to absorption of the pump pulse. The temporal evolution of the exciton population is obtained by changing the delay between the pump and probe pulses, where the temporal resolution is given by the pulse length or the accuracy of the delay stage, whichever is smaller. For our experimental realisation we use the output beam of a regenerative amplifier operating at 250 kHz which is seeded from a mode locked Ti:sapphire oscillator with a repetition rate of 80 MHz. The resulting pulses have a duration of  $\sim 250$  fs and a band width corresponding to 14 meV. The laser is tuned to the energy of the exciton transition around 796 nm which was estimated from photoluminescence measurements with a streak camera. The output beam of the amplifier is split into two parts with vertical and horizontal polarisation which represent the pump and probe, respectively. The probe beam passes through a delay stage in form of a retroreflector mounted onto a linear translation stage before both beams are brought to a cryostat containing the sample. For most of the measurements in this chapter the sample was cooled to 10 K using liquid helium in a cold finger cryostat. One pump-probe measurement was performed at 50 K. Figure 5.1 shows a schematic of the experimental setup. The prism

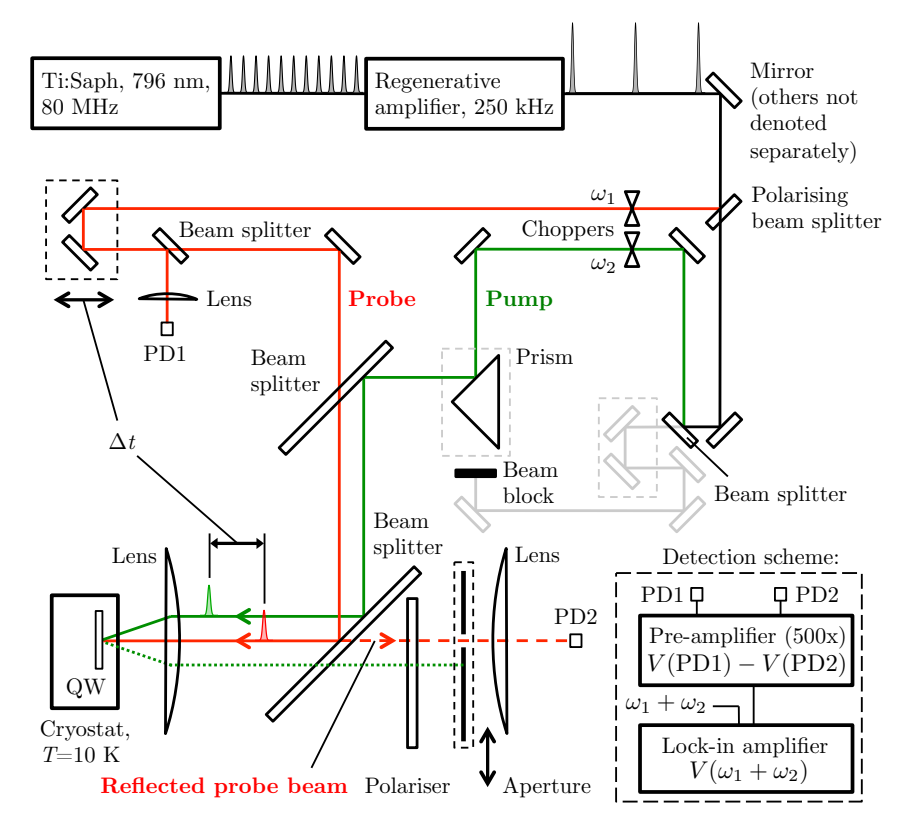


Figure 5.1 – Pump probe reflection setup. Components without individual annotation represent mirrors. PD1 and PD2 denote two identical photodiodes. The dotted line represents the undesired reflection of the pump beam, while the dashed line represents the reflected probe beam. The grayed out components are irrelevant for this experiment. They belong to the transient grating setup which will be explained in the next section.

is coated with silver and at this stage acts like an ordinary mirror. A large aspherical lens  $(f = 10 \text{ cm}, \varnothing = 10 \text{ cm})$  is used to focus the pump and probe beams onto the sample with overlapping spots of the size 75  $\mu$ m and 25  $\mu$ m, respectively, where the spot size of the probe beam is adjusted by means of a telescope in the beam path (telescope not shown in schematic). The excitation energy density per pulse is  $90 \ \mu \text{J/cm}^2$  and  $81 \mu J/cm^2$  for the pump and probe beams, respectively. A camera with a zoom lens was used to monitor the overlap of the different beams on the sample surface. The probe beam is guided on the centre axis of the lens whereas the pump beam enters the lens on an off-centre axis. In this way the two beams are spacially separated after the reflection from the sample surface. The same lens is also used to collect and collimate the probe beam after reflection and the probe beam is separated from the reflected pump beam with an aperture as well as a polariser. Finally, the reflected probe beam is focussed with an identical aspherical lens onto a photodiode. Because the change in the sample's reflectivity induced by the pump pulse is generally very small, the signal is typically measured employing a detection scheme with a lock-in amplifier in combination with two balanced detectors. This scheme requires two identical photodiodes to measure the probe beam before and after the reflection, as well as the modulation of the probe and pump beams with two phase locked optical choppers at different frequencies  $\omega_1$  and  $\omega_2$ .

Here, the modulation frequencies lie in the range of a few kHz. The intensity of the probe beam on the photodiodes is adjusted with neutral density filters such that both detectors yield equal output voltages in absence of the pump beam. A preamplifier is used to obtain the difference of the two signals and to amplify the resulting signal by a factor of 500. Finally, the pre-amplified differential voltage goes as input to a lock-in amplifier that demodulates the signal at the sum frequency  $\omega_1 + \omega_2$  and yields a signal which is proportional to the change of reflectivity induced by the presence of the pump beam. The change of reflectivity directly corresponds to the population of the state that is being probed. Because the lock-in amplifier operates at the sum frequency, the detection scheme is only sensitive to a change of light intensity on PD2 that is caused by the arrival of the pump beam on the sample, but not by room light or laser light scattered from optical components.

#### 5.1.4 Transient grating spectroscopy

The experimental setup explained in the previous paragraph was effectively implemented as a part of another experimental configuration that provides the main tool for the studies in this chapter: transient grating spectroscopy. This technique, also referred to as transient four wave mixing, is another pump-probe technique where the interference pattern of two laser beams creates a periodic modulation of the carrier density in the sample which effectively acts as a diffraction grating for a third incoming laser beam. It has been employed in different configurations since the 1980s to study carrier and spin diffusion as well as coherence phenomena in AlGaAs/GaAs heterostructures with subpicosecond resolution [82–94]. Reference [86] is of particular relevance as it is the first demonstration of the experimental configuration we employ. Since the 1980s the general interest in the technique has faded away with a few exceptions [95–97]. The pioneering work undertaken by a few individuals, namely the spectroscopists A. Miller, L. Schultheis, A. Honold and K. Leo, proved to be the most valuable resource when we set up our own experiment. Although the laser systems and electronics that were available at that time were inferior to our current equipment their work has set a very high standard that we are seeking to match.

#### 5.1.4.1 Population grating

The first variation of the transient grating technique employs a population grating that diffracts the probe beam. By performing the experiment with a pulsed laser and a variable retardation between the two *pump* beams that produce the periodic modulation of the carrier density and the *probe* beam that gets diffracted, the decay dynamics of the effective grating can be obtained. The longer the delay between the probe beam and the pump beams, the more carriers have recombined or diffused from regions of high to

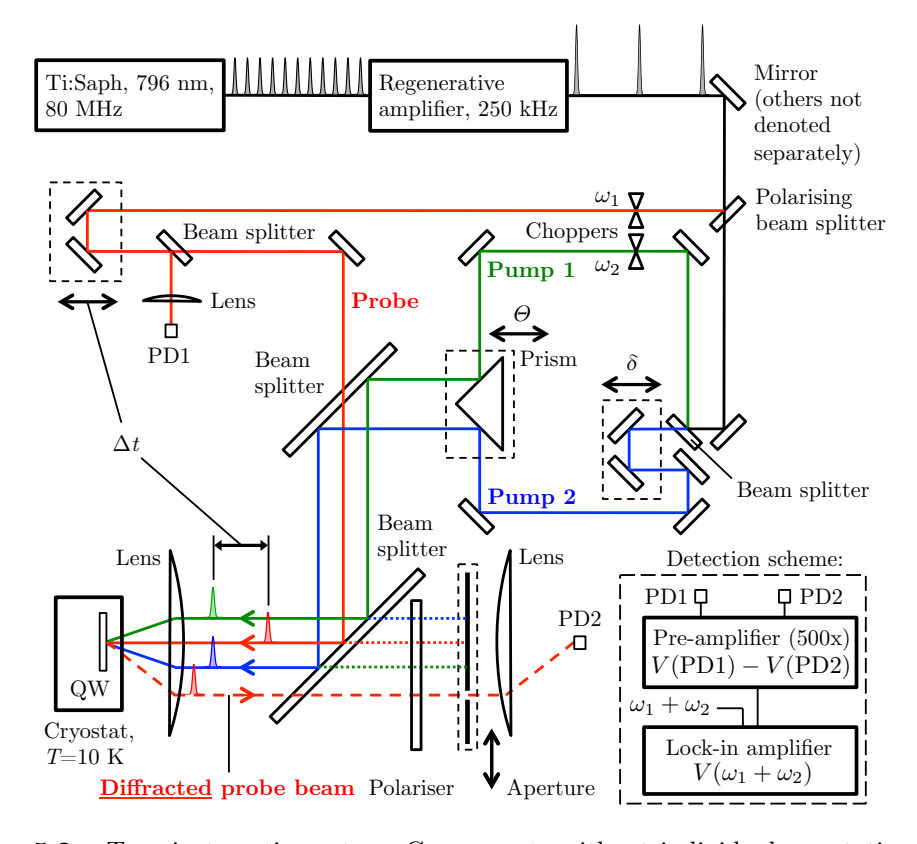


Figure 5.2 – Transient grating setup. Components without individual annotation represent mirrors. PD1 and PD2 denote two identical photodiodes. The dotted lines represent undesired reflections, while the dashed line represents the diffracted probe beam.

low population, reducing the contrast and thus the efficiency of the grating. The decay rate of the carrier concentration grating is given by the expression

$$\Gamma = \frac{4\pi^2 D_{\rm a}}{\Lambda^2} + \frac{1}{\tau_{\rm X}},\tag{5.1}$$

where  $D_{\rm a}$  is the ambipolar (combined electron and hole) diffusion coefficient whose magnitude is dominantly determined by the hole mobility and  $\tau_{\rm X}$  is the exciton recombination time. It should be noted that the intensity of the diffracted signal in transmission and reflection, the FWM signal, decreases with a rate of  $2\Gamma$  because the magnitude of the diffracted electric field, not the intensity, decreases with the decay rate of the concentration grating. Our experimental configuration (shown in Fig. 5.2) measures the diffracted signal in the reflection geometry because this does not require the removal of the substrate from the sample.

The process that we just described as diffraction can also be thought of as an incoherent four wave mixing experiment: here there are three input photons from the two pump beams and the probe beam and one output photon corresponding to the diffracted beam. The energy and direction of the generated FWM photon can be obtained by applying

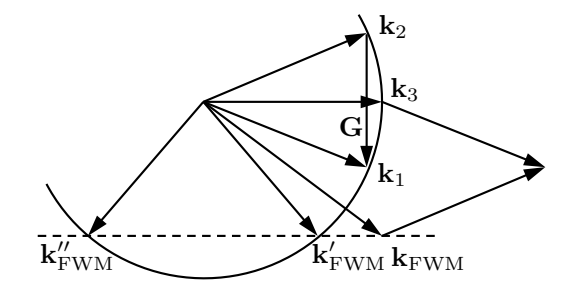


Figure 5.3 – FWM vector diagram. The two pulsed pump beams with wave vectors  $\mathbf{k}_1$  and  $\mathbf{k}_2$  interfere to create a grating with periodicity vector  $\mathbf{G} = \mathbf{k}_1 - \mathbf{k}_2$ . The probe pulse with wave vector  $\mathbf{k}_3$  diffracts off the transient grating induced by the pump pulses and propagates into the  $\mathbf{k}_1 - \mathbf{k}_2 + \mathbf{k}_3 = \mathbf{k}_{\text{FWM}}$  direction. This wave vector is not energy-conserving and gets projected back along the growth direction (dotted line) onto the energy-conserving sphere (solid circle). The new resulting direction is  $\mathbf{k}'_{\text{FWM}}$  or also  $\mathbf{k}''_{\text{FWM}}$  for a backwards propagating version. (Figure according to Ref. [96].)

the laws of energy and momentum conservation:

$$E_{\text{FWM}} = E_1 - E_2 + E_3 \tag{5.2}$$

$$\mathbf{k}_{\text{FWM}} = \mathbf{k}_1 - \mathbf{k}_2 + \mathbf{k}_3 \tag{5.3}$$

However, the wave vector  $\mathbf{k}_{\mathrm{FWM}}$  is not energy conserving and gets projected back onto the energy conserving sphere such that the in plane wave vector is conserved, but not the out of plane wave vector (see Fig. 5.3). This is due to the lack of translational symmetry in the direction normal to the QW plane. The projection of  $\mathbf{k}_{\mathrm{FWM}}$  gives rise to two possible directions of the outgoing photon:  $\mathbf{k}'_{\mathrm{FWM,F}}$  and  $\mathbf{k}''_{\mathrm{FWM,B}}$  for the forward and backward propagating diffracted photon. According to Heisenberg's uncertainty principle these two possible wave vectors are permitted because the interaction length in the direction normal to the QW plane,  $\Delta z$ , is small and, hence, the uncertainty in the momentum in this direction, the  $\Delta \mathbf{k}_z$ , must be correspondingly large. This technique allows one to probe a distinct exciton wave vector  $\mathbf{k}_{\mathrm{X,\parallel}}$  which is equivalent to the grating vector and the in plane momentum of the diffracted photons,  $\mathbf{k}_{\mathrm{X,\parallel}} = \mathbf{k}'_{\mathrm{FWM,\parallel}} = \mathbf{G} = 2\pi/\Lambda \cdot \mathbf{e}_{\parallel}$ , where  $\Lambda$  is the grating period and  $\mathbf{e}_{\parallel}$  is the unit vector parallel to the surface and across the interference pattern.

#### 5.1.4.2 Spin grating

Before we focus on the details of the experiment we briefly summarise another variation of this technique that allows measurement of the electron spin diffusion coefficient in contrast to the ambipolar carrier diffusion coefficient. This is achieved by producing a so called spin grating from the interference between two pump beams with perpendicular polarisations and equal intensity. Both pump beams and the probe beam are tuned to the heavy-hole exciton transition. The resulting interference pattern on the sample has uniform intensity, but the vector of the electric field is spatially modulated from linear

to circular to orthogonally linear to circular of the opposite sense and back to linear polarisation. In GaAs QWs the degeneracy between the light and heavy hole bands is lifted and hence the polarisation sensitive selection rules for interband transitions determine the spin statistics of the electrons and holes after absorption of polarised light. Absorption of circularly polarised light by the QW yields 100 % spin-polarised electron-hole pairs where the hole spin relaxes much faster than the electron spin due to band mixing and the mixed spin character of the valence states [94]. Hence, the polarisation grating effectively produces a spatial modulation of electron spins in the semiconductor. As a consequence, an incoming probe beam gets diffracted from this spin grating similarly to the case of the population grating discussed above. The spin grating then decays through carrier diffusion and spin relaxation and the dynamics of the process can be time resolved with a retarded probe beam as described before. Also in this case the decay rate of the spin grating can be described by an expression equivalent to eq. 5.1 where the ambipolar diffusion coefficient is replaced by the electron diffusion coefficient and the exciton recombination time is replaced by the spin relaxation time. A direct comparison of the different typical parameters for a population and spin grating in GaAs QWs can be found in Refs. 94 and 96.

#### 5.1.5 Effect of energy transfer on the FWM signal

The measurement of the QW's photoluminescence decay from chapter 4 provides a typical example for the characterisation of energy transfer in the time domain. Alternatively, the transient dynamics of the exciton population can be measured by the pump-probe reflection technique. In both cases an increased decay rate of the exciton population in the QW along with certain control experiments provide strong evidence for the occurrence of resonance energy transfer. However, these techniques measure the decay of the entire exciton population and one of the main conclusions of the previous chapter was that this gives access only to the average rate of energy transfer in the thermalised exciton ensemble. According to the theory, excitons with different wave vectors undergo energy transfer at different rates and the ensemble constantly thermalises while photoluminescence is only observed from excitons near the band edge and within the light cone. We are seeking a means to probe the energy transfer rate for an excitonic state with a distinct wave vector. When the transient grating technique is employed this wave vector is given by the grating vector **G** which in turn is determined by the wavelength of the incident pump beams and the angle between them. Hence, the resonant wave vector can be adjusted by the angle  $\phi$  between the two incoming pump beams according to the relation [88]

$$\mathbf{k}_{\mathrm{X},\parallel} = \mathbf{G} = \frac{2\pi}{\Lambda} \mathbf{e}_{\parallel} = \frac{2 \cdot 2\pi \sin(\phi/2)}{\lambda} \mathbf{e}_{\parallel}.$$
 (5.4)

Evidently, this is the main parameter that is varied in our experiment (see Fig. 5.2). The periodically modulated carrier population created by the interference pattern of the two

pump beams acts as a grating to the incoming probe beam. The created charge density collectively transfers momentum to the incoming beam such that it gets diffracted in transmission and reflection. This produces an outgoing light beam with an in-plane wave vector **G** that itself can interact with the QW before it exits the sample. Therefore, the FWM signal, namely the diffracted beam, carries information about the interaction with excitonic states of a particular wave vector G. The intensity of the FWM signal for a particular angle  $\phi$  will be reduced by the amount of light that gets absorbed by the exciton state with the corresponding wave vector. The absorption by this state in turn is enhanced if resonance energy transfer contributes to its depletion. Since resonance energy transfer is a wave vector dependent process, the direct comparison of the FWM signal intensity with and without energy transfer for different wave vectors potentially yields the desired wave vector dependence. In the experiment this is achieved by performing separate measurements with two QW samples, one bare sample and one which is covered with a thin layer of QDs to enable resonance energy transfer. This gives rise to a great experimental challenge because the measurement and comparison of absolute intensities between different samples is more difficult than the measurement of only the decay rate of a signal as it is the case for the pump probe technique or time resolved photoluminescence measurements.

#### 5.1.6 Wave vector and time resolved photoluminescence

The proposed FWM technique to measure the wave vector dependence of resonance energy transfer is novel and experimentally challenging. In order to have some indication for the validity of the results we also performed wave vector and time resolved photoluminescence measurements with a streak camera (the basic principle of a streak camera was explained in chapter 3.2.3.2). The required setup is routinely used in this research group to study the dynamics of exciton polaritons in semiconductor microcavities and relatively little effort was required to yield the desired result [98, 99]. The setup (depicted in Fig. 5.4) employs a 100x far field objective with NA 0.7 to focus the excitation laser onto the sample and collect the photoluminescence. A lens behind the objective transforms the real space image of the sample to the Fourier representation and this transformed image is then projected onto the entry slit of the streak camera. The slit is aligned with the image such that the cross section includes the  $\mathbf{k}=0$  point of the dispersion. Reflected and scattered laser light is filtered out from the detection arm by suitable long pass filters.

#### 5.1.7 Angle resolved pump probe technique

Another technique that holds the potential to yield the desired wave vector dependence of resonance energy transfer should be briefly mentioned here. The angle resolved pump

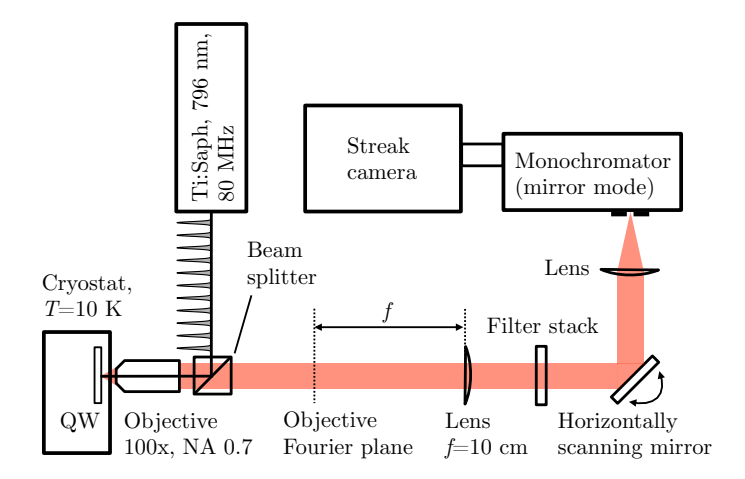


**Figure 5.4** – Wave vector resolved photoluminescence setup with a streak camera.

probe technique is effectively a pump probe configuration as described above where the angle of the incident pump beam is adjusted to a distinct wave vector. However, the technique is limited in the sense that although excitons are injected into the QW with the wave vector of the pump beam exciton scattering will quickly populate excitonic states with other wave vectors, making it impossible to probe the evolution of the resonant state isolated and directly. The absorption of the resonant pump beam by a specific exciton state will be enhanced if this state is depleted more efficiently by energy transfer and only a few excitons will scatter into other wave vectors which together are probed by the probe beam. In this way the wave vector dependence of energy transfer can be probed only indirectly. It can be thought of an equivalent of photoluminescence excitation spectroscopy in terms of the parameters of a pump probe experiment: the pump beam is scanned over different incident angles and for each angle the signal amplitude and the decay rate of the pump probe signal is recorded to yield a dependence on the incident angle. After the other techniques gave compatible results this experiment was omitted from this study. Nevertheless, ongoing research in the group will continue to design and implement novel ways to probe the wave vector dependence of resonance energy transfer.

#### 5.1.8 Comparison of the different techniques

Each of the different techniques discussed so far has its respective advantages and short-comings. The transient grating technique promises to be particularly sensitive as four wave mixing is a non-linear process and the intensity of the outgoing diffracted beam is directly affected by energy transfer. However, for a single QW the signal level is so low that it is challenging to detect the signal at all, especially with an acceptable signal to noise ratio. The main drawback of the angle resolved pump probe technique is that it only indirectly probes the energy transfer process via the resonantly pumped exciton state which undergoes efficient energy transfer. Excitons that do not directly undergo energy transfer will be thermalised to other wave vectors and only the total

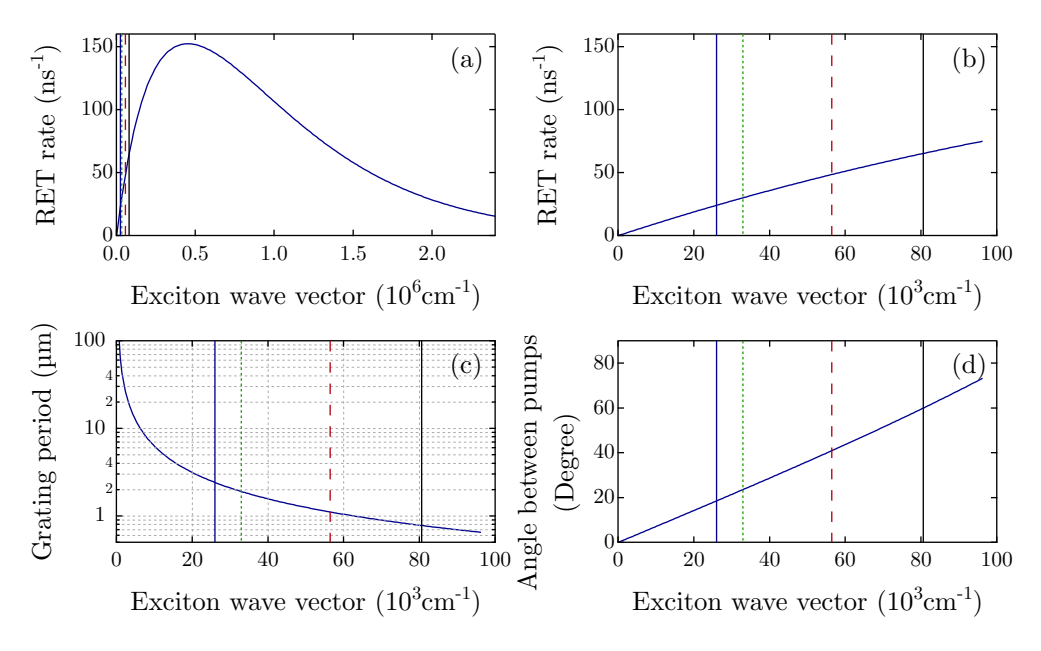


Figure 5.5 – Range of exciton wave vectors accessible by different spectroscopy techniques. (a) and (b): Calculated dependence of the energy transfer rate on the exciton wave vector (according to the model from chapter 4). (c) and (d) show which grating period and angle between the pump beams is required to access different wave vectors with the transient grating technique. The vertical lines represent the maximum wave vector accessible by different techniques (from left to right): FWM (blue solid line), conventional pump probe with the same lens for all beams (green dotted line) and angle resolved photoluminescence with the streak camera (red interrupted line). The rightmost black line corresponds to the wave vector at the edge of the light cone.

exciton population can be detected by the probe beam. The angle resolved photoluminescence measurement holds the potential to yield the complete wave vector dependence of resonance energy transfer in two shots with the streak camera, one for the reference sample and one for the sample covered with QDs. In comparison with the pump probe techniques the time resolution of the streak camera is fundamentally limited not by the duration of the laser pulses used for excitation, but by the internals of the streak camera. The resulting time resolution was estimated to be  $\approx 80$  ps, which is two orders of magnitude greater than the resolution of the pump probe techniques which is given by the pulse length ( $\approx 0.2$  ps). The final important criteria for comparing the different techniques is the range of wave vectors that can be probed. The maximum wave vector that can be accessed by each of the different techniques is presented graphically in Fig. 5.5. The figure also shows the rate of energy transfer that according to the previously used model by Basko et al. is to be expected over this range of wave vectors [1, 29]. It can be seen that none of the techniques allows one to reach the wave vectors where the energy transfer rate is maximal but that all of them allow to cover wave vectors for which energy transfer becomes significant in relation to the decay rate of the QW excitons. The setup with the streak camera and the 100x objective allows to cover the greatest range of wave vectors.

#### 5.2 Results and discussion

#### 5.2.1 Evidence for energy transfer in the exciton ensemble

Let us start the results section with some evidence that energy transfer does indeed occur in the GaAs QW/PbS QD material system to justify all the other experiments performed for this study. In the presence of the QD overlayer on the sample an accelerated depletion of the exciton population is observed in pump probe experiments for small angles of incidence of the pump and probe beams. The decay of the exciton population without and with the QD layer is presented in Fig. 5.6. It can be seen that not only the decay rate inherent to the QW excitons is different for 10 K and 50 K but also the rate of energy transfer varies. At 10 K and 50 K the observed exciton lifetimes are 170 ps and 3670 ps and the average efficiency of energy transfer from the exciton ensemble is 18 % and 63 %, respectively. The longer carrier recombination time observed at 50 K is a consequence of the increased thermal energy of the excitons. With increasing temperature an increasing fraction of excitons occupies states with wave vectors which lie outside of the light cone while exciton recombination can only occur from excitons within the light cone. The entire exciton ensemble effectively shares the oscillator strength of the interband transition at  $\mathbf{k} \approx 0$  and thus the lifetime of the exciton recombination process increases as the temperature and the homogenous broadening of the exciton ensemble increases [100]. The increased rate of energy transfer at 50 K is also temperature related and is explained by the freeze out of excitons at low temperatures. At 10 K a considerable fraction of excitons remains trapped in local potential fluctuations or bound to impurity atoms and any free excitons occupy only states with small wave vectors where energy transfer is very slow. At higher temperatures the localised excitons become free and according to Boltzmann's statistics excitonic states with higher wave vectors are occupied such that

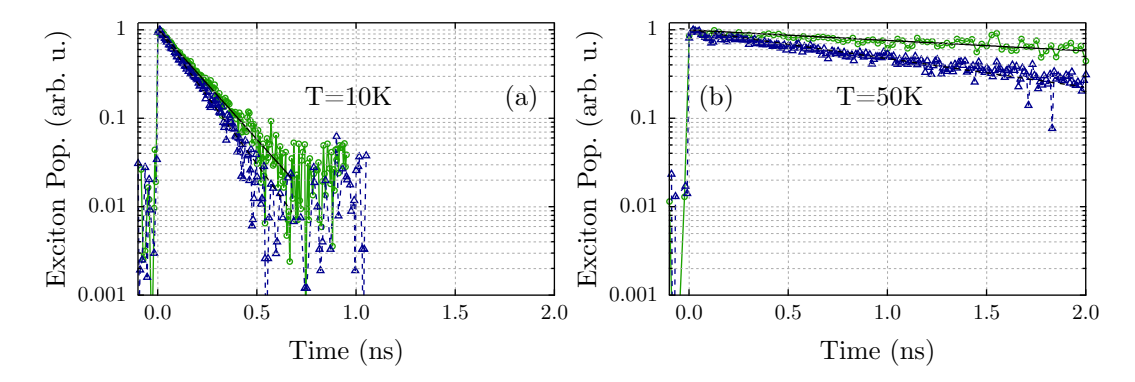


**Figure 5.6** – Evidence for resonance energy transfer from excitons in the GaAs QW to an overlayer of PbS QDs. (a) and (b) show the temporal evolution of the exciton population measured with the pump probe technique at 10 K and 50 K, respectively. The green circles and blue triangles represent the evolution in absence and presence of the QD overlayer, respectively. The overlaid black lines are fitted exponential decays.

efficient energy transfer is enabled. The temperatures that yield wave vectors which are too high for efficient energy transfer lie above the 50 K used for this experiment.

#### 5.2.1.1 Constructing a suitable model function for fitting the data

In order to achieve accurate data fitting of the transient FWM data a model function f(t) was constructed. As it will be shown shortly, the experimental data features a constant background level which reveals itself for both negative probe delays and very long positive probe delays. This is accounted for by the inclusion of a constant background B in f(t). The population grating decays exponentially with a decay rate of  $\Gamma$  and hence the FWM signal decays exponentially with a rate of  $\Gamma_{\rm FWM} = 2 \cdot \Gamma$ . The characteristic timescale of the decaying FWM signal approaches the temporal width of the laser ( $\delta \approx 250$  fs) and therefore it is good practice to employ the convolution of an exponential decay with a gaussian excitation pulse rather than just an exponential decay when fitting the FWM signal. The resulting contribution to the fitting function is the convolution

$$\left[A_{\text{FWM}} \cdot e^{-\Gamma_{\text{FWM}} \cdot (t - t_{\text{FWM}})} \cdot \Theta(t - t_{\text{FWM}})\right] * \left[\frac{1}{\sqrt{2\pi}\delta} \cdot e^{-\frac{t^2}{2\delta^2}}\right], \tag{5.5}$$

where the star symbol (\*) denotes the convolution,  $A_{\rm FWM}$  is the initial amplitude of the FWM signal,  $t_{\rm FWM}$  is the time where the FWM signal begins and  $\Theta(t-t_{\rm FWM})$  is the unit step function. When looking at the experimentally obtained transient FWM signal (the reader may take a preview on Fig. 5.8) it is apparent that each of the recorded decays is preceded by a very short peak with a large negative amplitude. This peak of opposite sign to the actual signal is of comparable amplitude for the measurements with different grating periods and closer examination of the same reveals that for all measurements it has the temporal width  $\delta$  of the laser pulse. We interpret this peak as an coherent artefact that occurs at time  $t_0$  when all three beams hit the sample simultaneously and it is accounted for in the model function by the subtraction of a gaussian pulse, i.e.

$$-\frac{A_{\text{CA}}}{\delta\sqrt{2\pi}} \cdot e^{-(t-t_0)^2/2\delta^2}.$$
 (5.6)

The resulting function f(t) that is used for fitting the transient FWM signals is then given by

$$f[A_{\text{FWM}}, \Gamma_{\text{FWM}}, t_{\text{FWM}}, A_{\text{CA}}, t_0, \delta, B](t) = \frac{A_{\text{FWM}}}{2} e^{\Gamma_{\text{FWM}} \left(\Gamma_{\text{FWM}} \delta^2 / 2 - (t - t_{\text{FWM}})\right)} \times \left[1 - \text{erf}\left(\frac{\Gamma_{\text{FWM}} \delta^2 - (t - t_{\text{FWM}})}{\sqrt{2}\delta}\right)\right] - \frac{A_{\text{CA}}}{\delta \sqrt{2\pi}} \cdot e^{-\frac{(t - t_0)^2}{2\delta^2}} + B,$$

$$(5.7)$$

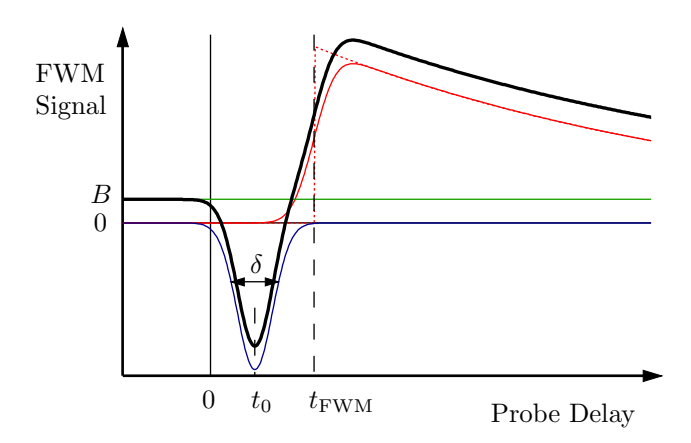


Figure 5.7 – Different contributions to the model function for the FWM signal. The model function is plotted as a black curve, while the different contributions are plotted separately in various colours: the exponential decay of the transient FWM amplitude is shown before and after convolution with the laser pulse as a red dotted and solid curve, respectively. The coherent artefact that occurs when all three beams hit the sample is represented as a blue gaussian pulse. The green horizontal line corresponds to a constant voltage offset when measuring the FWM amplitude. See Eq. 5.7 for the mathematical definition of the symbols and curves.

where the parameters of f(t) are listed inside the square brackets and the result of the convolution is explicitly given in terms of the error function. In the experimental realisation of this experiment the position corresponding to "0" delay between the probe pulse and the two pump pulses shifts along the delay stage as the prism position is varied. We choose to only approximate this shift and plot the data against a horizontal axis where "0" may occur a few ps before the coherent artefact. Accurate data fitting is ensured by allowing for an offset  $t_0$  for the coherent artefact. The different contributions to the model function are visualised in Fig. 5.7.

#### 5.2.2 Determination of the ambipolar diffusion coefficient

It was mentioned above that the measurement of the wave vector dependence of energy transfer by means of FWM relies on the measurement and comparison of the amplitude of the FWM signal from the QW without and with the QD overlayer, but not the decay rate of the signal. Along with the measured amplitude we naturally also obtained the grating decay rate and this data should be briefly discussed here as it yields the ambipolar carrier diffusion coefficient. Equipped with the fitting function f(t) from eq. 5.7 the different features of the transient FWM data can be well reproduced and the decay rate of the signal is extracted with high accuracy. The transient of the FWM signal for different grating periods along with the best fit curves superimposed is shown in Fig. 5.8. Evidently, the grating decay accelerates as the period of the grating becomes smaller. When the decay rate of the FWM signal is plotted against  $\frac{8\pi^2}{\Delta^2}$  the slope of the resulting graph corresponds to the ambipolar carrier diffusion coefficient  $D_a$  while

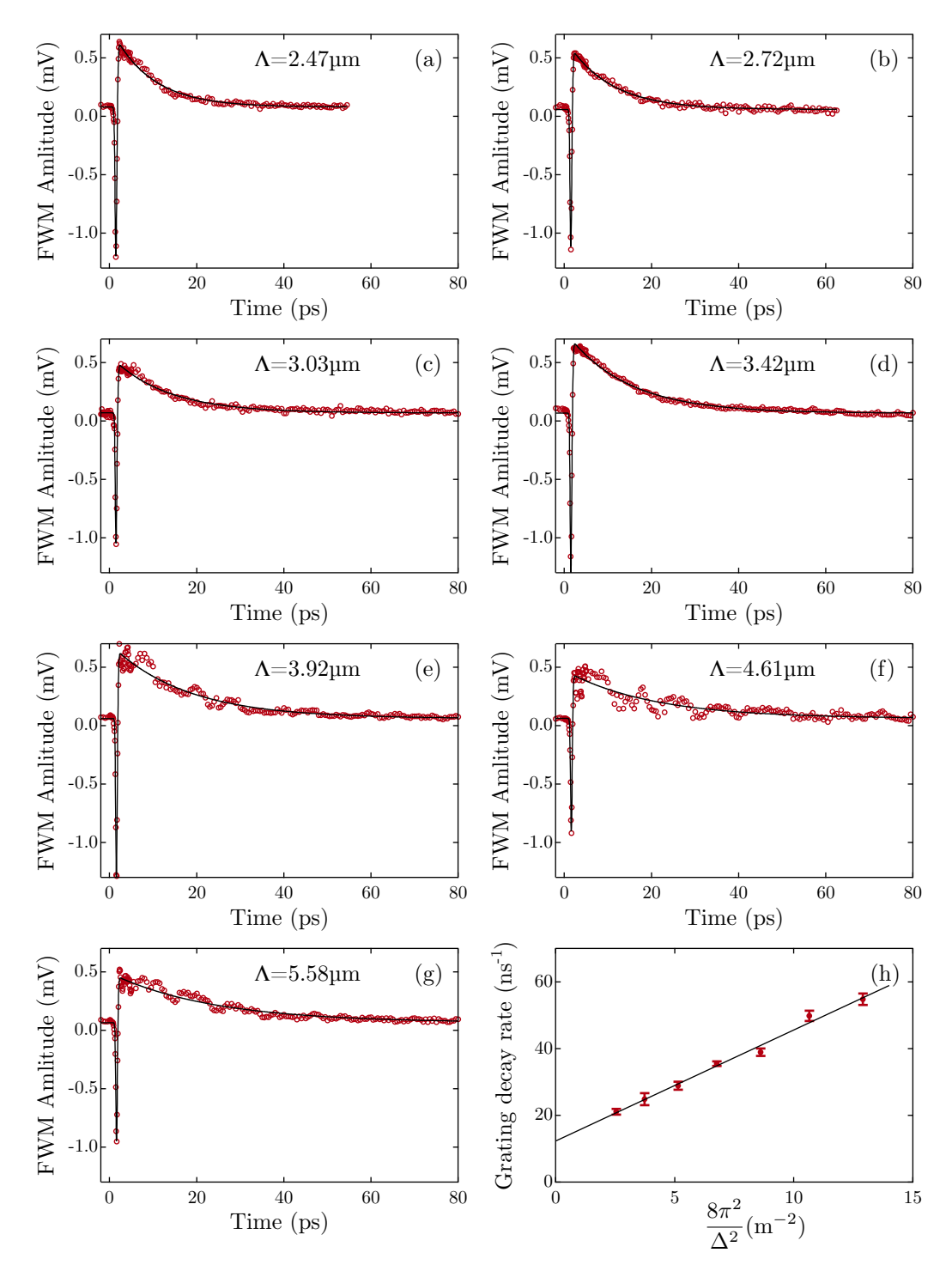


Figure 5.8 – Determination of the ambipolar diffusion coefficient from transient grating experiments. Figures (a)-(g) show the decay of the FWM amplitude with increasing probe delay for different grating periods. The black lines are fitted model curves according to equ. 5.7. (f) shows the grating decay rate plotted vs  $\frac{8\pi^2}{\Lambda^2}$ , where  $\Lambda$  is the grating period. The slope of the line gives the ambipolar diffusion coefficient  $D_a$  while the exciton recombination time can be estimated from the offset on the y-axis.

the offset with the y-axis gives  $2/\tau_X$  where  $\tau_X$  is the exciton recombination time. By performing a least square fit with a line of variable slope and offset the ambipolar diffusion coefficient was determined as  $D_a = 33 \text{ cm}^2/\text{s}$ . This value is about three times larger than the value of  $13 \text{ cm}^2/\text{s}$  observed in Ref. 94 for room temperature for MQWs of the same thickness. Our larger value for the ambipolar diffusion coefficient at 10 K in comparison with the value at room temperature is consistent with the observation of a monotonic decrease of the diffusion coefficient with temperature as it was observed for bulk GaAs [101]. The carrier recombination time was extracted from the offset of the graph on the x-axis as  $\tau_X = 163$  ps, which is in very good agreement with the value of 170 ps obtained from the pump probe experiment at the same temperature. After these warm-up experiments have yielded satisfying results the study continues with the more challenging comparative measurement of the amplitude of the FWM signal.

## 5.2.3 FWM signal with and without energy transfer for different grating periods

The difficulty in this part of the study arises from the fact that the amplitude, not the decay rate, of the FWM signal has to be compared for the samples without and with the QD layer in independent measurements. The amplitude of the signal is measured by a photodiode and naturally any misalignment of the (invisible) diffracted beam on the photodiode will result in an apparent lower signal. The crucial alignment of the sample surface relative to the incoming beams was done by guiding the reflection of the probe beam from the sample through an iris. The apparent amplitude of the signal will also crucially depend on the spacial overlap between the three beam. Any directional fluctuation of the output beam from the regenerative amplifier will result in a decreased spacial overlap because the three beams travel along different paths and pass differently aligned retroreflectors. It was found that a CMOS camera sensor in the focal plane of the focusing lens can be used as a reliable tool to calibrate and correct the drift of the three beams such that all beams remain centred when the prism is moved to change the grating period (see Fig. 5.2). During the measurements another camera with a zoom lens permanently monitors the overlap and helps to identify excessively large movements and vibrations of the cryostat when the floating optical table is disturbed. In principal these measurements are identical to the ones performed for the measurement of the ambipolar diffusion coefficient. However, because the scanning of the probe delay is time consuming and the actual time dependence of the FWM signal is not of interest here, the delay line is only scanned over a range of 5 ps for each grating period to capture the rise and initial amplitude of the FWM signal. A computer program is used to control the movement of the translation stages that mount the prism and the delay line of the probe beam while the amplified and filtered voltage from the photodiodes is recorded. In this way four datasets are measured for each the reference sample without QDs and the energy transfer enabled sample with QDs. Each of these datasets contains

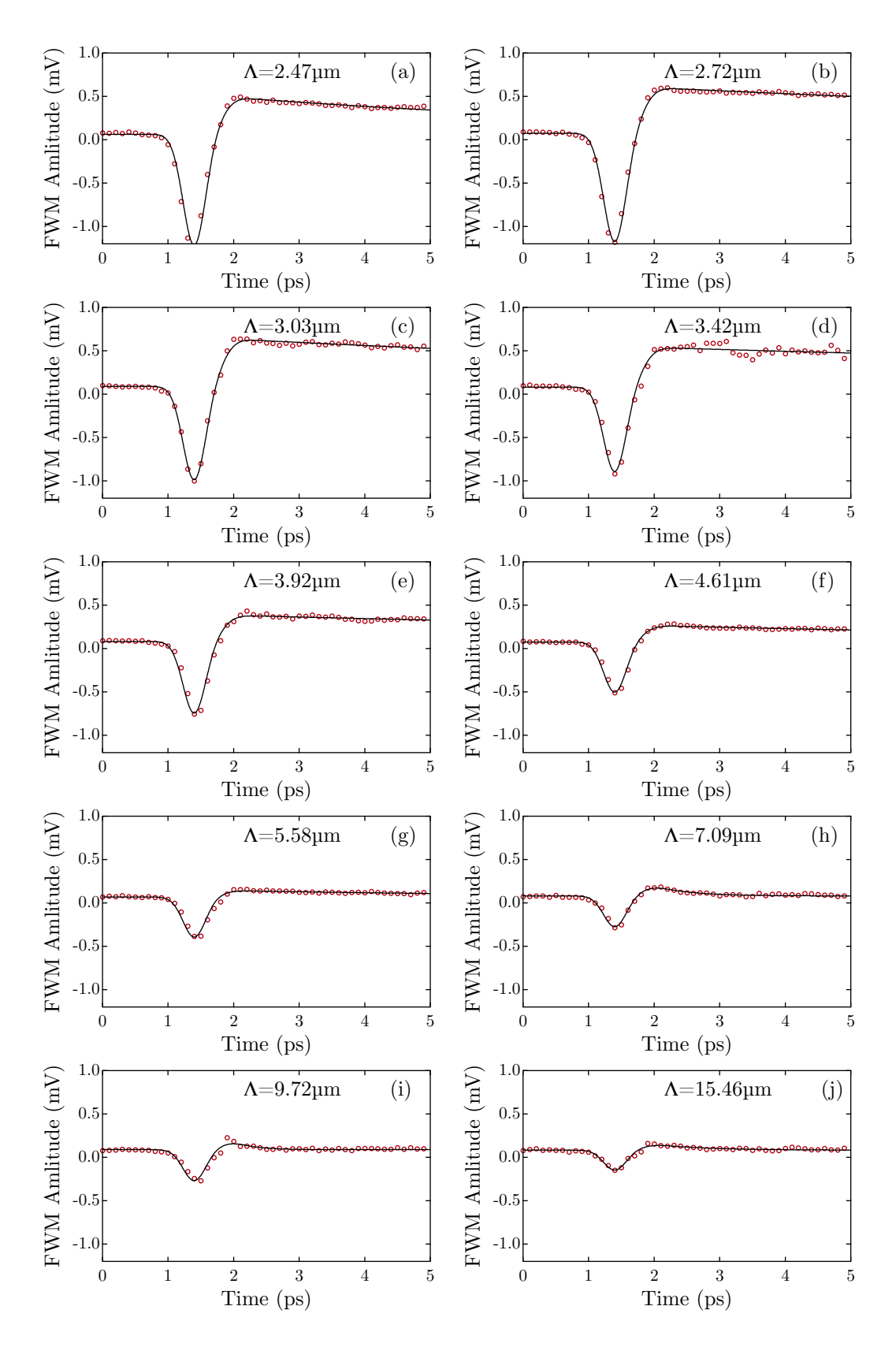
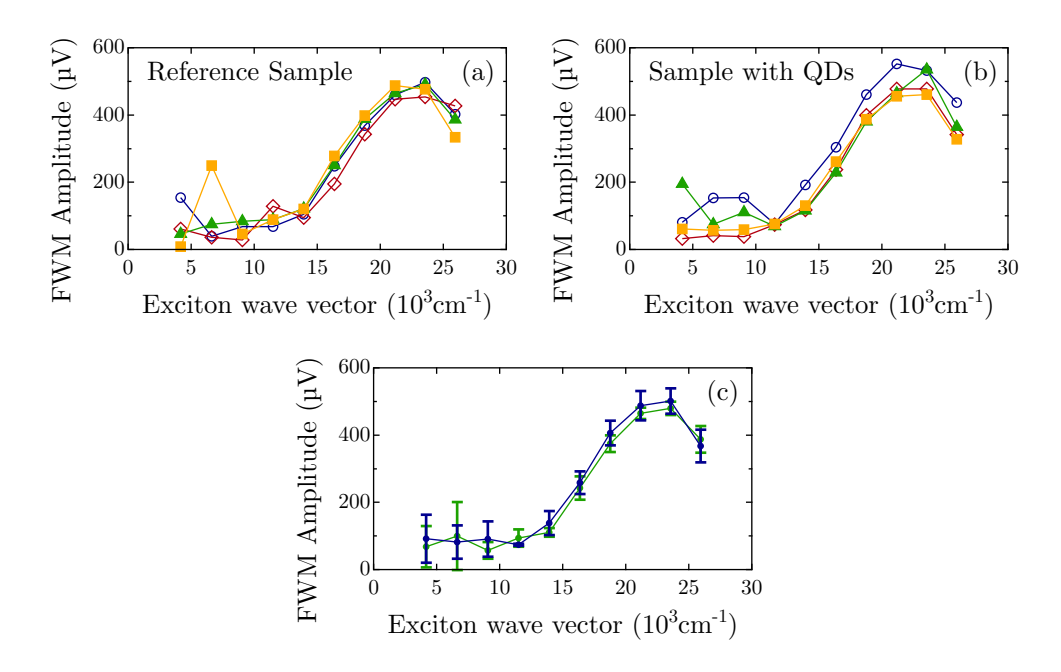


Figure 5.9 – One exemplary full dataset used to determine the amplitude of the FWM signal for different grating periods. (a)-(j) show the transient of the diffracted probe beam for a 5 ps range of delay times. The black lines are the best fits when using the function fitting f(t) as defined in equ. 5.7.



**Figure 5.10** – Amplitude of the FWM signal for different resonant wave vectors. (a),(b) Data from independent measurements on the reference sample without QDs and the sample covered with QDs, respectively. (c) The green and blue curves correspond to the average of the curves from (a) and (b), respectively.

data in the same format as the one shown exemplary in Fig. 5.9. When one dataset is analysed a global fitting is applied such that the parameters  $\delta$ ,  $(t_{\rm CA} - t_0)$  are constrained to be identical for all FMW decays in the dataset. This decreases the uncertainty of these parameters and their influence onto the values of the FWM amplitudes  $A_{\text{FWM},i}$ , where the index i denotes the i-th grating period during the scan. The evolution of the amplitudes  $A_{\text{FWM},i}$  for increasing grating period, measured four times for the reference sample and the sample with the QD layer, is shown in Fig. 5.10. All curves follow the same trend: the magnitude of the FWM signal increases as the grating period decreases and the last two data points lie at a slightly lower level. The position of the maximum is a result of the alignment and calibration procedure. Because the rate of energy transfer increases monotonous over the range of wave vectors that can be probed in this experiment we expect the difference in the FWM amplitudes to increase as the wave vector increases. The best temporal alignment between the two pump beams is adjusted for a prism position corresponding to large wave vectors such that features on the right hand end of the graph can be identified more easily. In theory there should not be any drift in the temporal overlap between the two pump beams when the prism is moved but here we face the experimental reality where the alignment of the beams, translation stages and optical elements can only be performed with limited accuracy. Despite the calibration related shape of the curve, the different measurements for the bare and hybrid sample do not show any obvious trend in the change of the relative FWM amplitude with increasing wave vector. From the four individual scans the mean values and the corresponding standard variance was calculated. The data is shown in

Fig. 5.10. Unfortunately, also the combined data does not reveal any trend on the change of the FWM amplitude when energy transfer is enabled in the QD covered sample. The difference between the two curves is less than 5 % and is clearly within the standard variance of the values. In short, the accelerated depletion of the excitonic state with the wave vector corresponding to the grating period does not affect (visibly) the amplitude of the diffracted beam. A possible explanation for why it is not possible to observe an effect of resonance energy transfer on the intensity of the FWM signal relates to the fast thermalisation of the exciton ensemble. When all exciton states are coupled to each other via fast thermalisation, it is impossible to measure energy transfer from an isolated state via photoluminescence or absorption measurements. This is because the characteristic time scale of the resonance energy transfer process is orders of magnitude slower than that of exciton scattering which occurs on the order of hundreds of femtoseconds. fast thermalisation makes the energy transfer process from a selected exciton state invisible to our measurements.

#### 5.2.4 Wave vector resolved photoluminescence

These experiments are performed with the same excitation density as the pump-probe and FWM measurements. We also investigate the effect for an excitation density that is 10 times larger. In the configuration that is used for this experiment the full angle dependence of the photoluminescence is not covered by a single image from the streak camera, but by three overlapping segments in k-space. This allows more accurate binning of the data for different wave vectors over smaller areas and yields less noise in the photoluminescence decays that are extracted for the different wave vectors. The streak images from the measurement on the reference sample without QDs are shown in Fig. 5.11. No trend can be identified from the images alone. A closer look at the extracted photoluminescence decays reveals a moderate quenching of the photoluminescence decay in the presence of the QDs, typical for the occurrence of energy transfer (Fig. 5.12). Figure 5.13 summarises all results of the experiment and shows the wave vector dependence of the photoluminescence decay rates of the QW without and with the QDs. Two observations can be made: over the complete range of wave vectors covered in this experiment the photoluminescence decay is accelerated in the presence of the QD overlayer, but a distinct wave vector dependence of energy transfer cannot be observed.

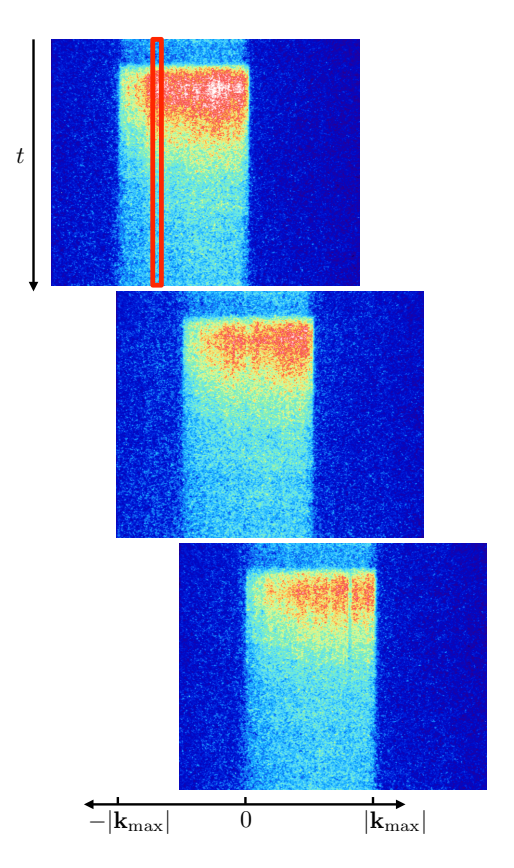


**Figure 5.11** – Time and wave vector resolved photoluminescence of the QW. The three streak images overlap in **k**-space. The red rectangle indicates the binning of vertical lines to extract a photoluminescence decay for a specific wave vector.

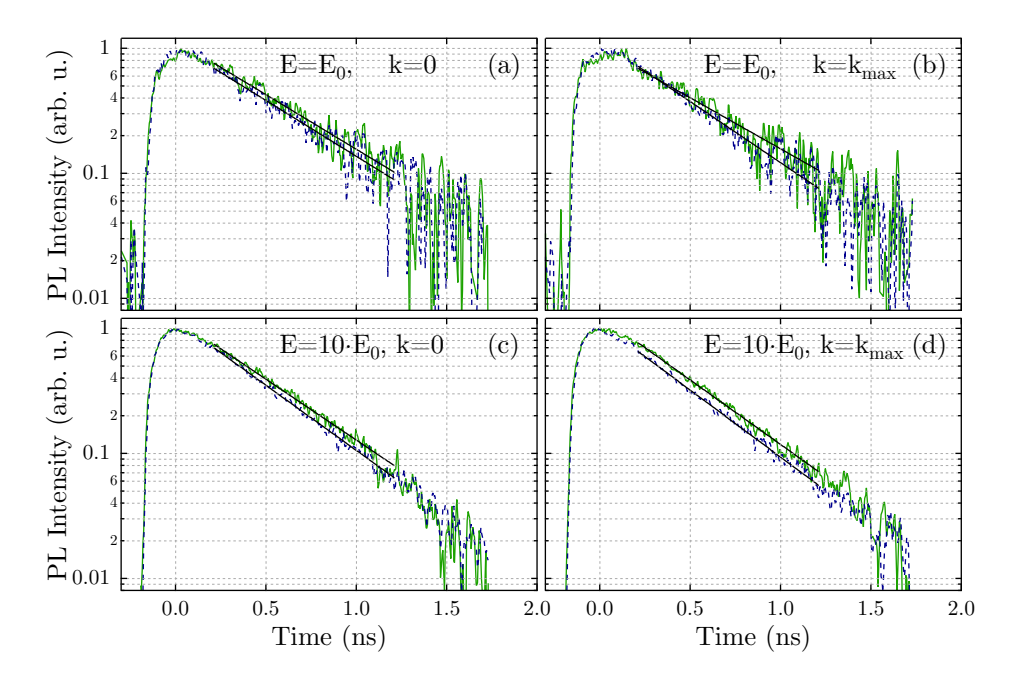


Figure 5.12 – Time resolved photoluminescence of the QW. (a), (b): Time resolved photoluminescence of the QW without (green line) and with the QD overlayer (blue dashed line) for  $\mathbf{k} = 0$  and the largest accessible wave vector, respectively. The excitation energy density  $E_0$  is the same as in the FWM experiment. (c), (d) show the same data for an excitation energy density which is ten times higher. The black lines are fitted exponential decays.

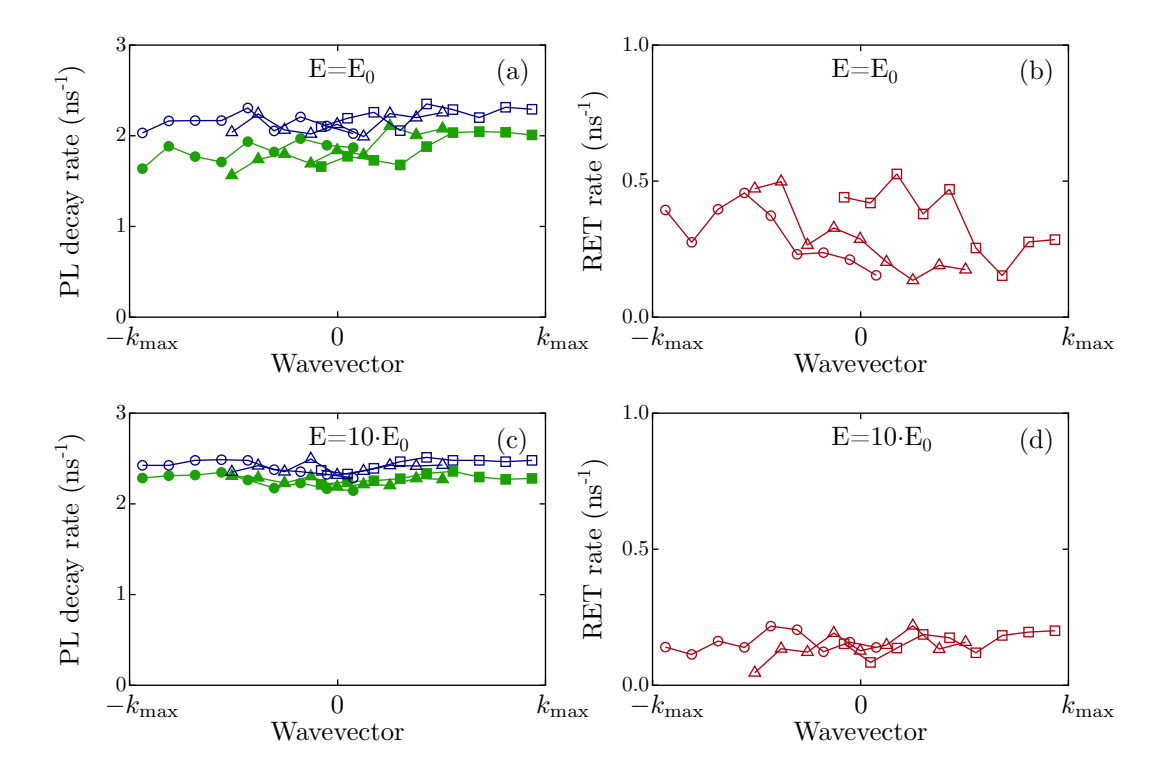


Figure 5.13 – Photoluminescence decay rate of the QW exciton for different wave vectors. (a) and (b) show the decay rates without and with the QD overlayer for the same excitation energy density  $E_0$  as in the FWM experiment. (c) and (d) show the same data for an excitation energy density which is ten times higher. Connected data points are extracted from the same streak image.

Chapter 5 Conclusions

#### 5.3 Conclusions

In summary, an extensive range of techniques and experiments was employed to measure the dependence of resonance energy transfer on the wave vector of QW excitons. The pump-probe reflection technique as well as time resolved photoluminescence measurements prove the occurrence of energy transfer from excitons in the GaAs QW to an overlayer of PbS colloidal nanocrystals. The pump-probe experiment provides evidence that the average efficiency of energy transfer in the exciton ensemble at 10 K reaches nearly 20 %. Also the time and wave vector resolved photoluminescence measurements indicate the occurrence of energy transfer. The ultimate goal to obtain experimentally the explicit dependence of resonance energy transfer on the exciton wave vector was reached neither by the use of the transient grating technique nor by performing angle resolved photoluminescence measurements. In conclusion, the dynamics of energy transfer from an exciton state with a defined wave vector are shielded to our optical measurements because exciton thermalisation occurs much faster than the energy transfer process. Due to the thermalisation within hundreds of femtoseconds only the average rate of the energy transfer dynamics in the exciton ensemble can be probed by our measurements.

#### 5.4 The author's contribution

I am grateful to Dr. Chunyong Li, University of Southampton, who has introduced me to the pump probe reflection technique used in this chapter. Together, we have designed, built and tested the setup for the transient grating technique, a technique that was new for both of us. It is not possible to separate our contributions to the work in the lab and data acquisition. The data analysis and calculations presented in this chapter were done by me alone, Jan Junis Rindermann. Occasionally, Dr. Li performed his own calculations to find agreement between our results.



# Resonance Energy Transfer from PbS Quantum Dots to Silicon

In the introduction to this work (chapters 1 and 2) it was noted why and, in terms of technology, how our societies seek to reduce their carbon footprint. Research on semiconductors in the fields of LEDs as energy saving light sources as well as photovoltaic cells for the direct production of electricity from sun light promise to return sustainable solutions. The majority of the work in this thesis covers the former, but in view of the support that I received from the Reiner Lemoine Stiftung<sup>1</sup> the scope of this thesis is completed by the summary of my initially planned research and the results concerning solar cells.

In this chapter we investigate energy transfer from PbS QDs to a silicon slab by means of a finite element method (FEM) simulation. The study will unveil important design constraints for the implementation of this scheme in real world solar cells. The focus lies on the dependence of the energy transfer rate on the thickness of a spacing layer separating the QDs from the absorptive silicon. In practice this layer is an anti-reflection coating and/or a passivation layer or a transparent electrode on top of a p-n junction.

<sup>&</sup>lt;sup>1</sup> "Reiner Lemoine, \*1949, †2006, was a German entrepreneur in the the field of Renewable Energy. During his studies of aerospace engineering he co-founded Wuseltronik, a socialistic collective for engineering based in Berlin-Kreuzberg. In 1996 he co-founded Solon AG, followed in 1999 by the solar cell manufacturer Q-Cells. In 2005 he was awarded as "Entrepreneur of the year" together with Anton Milner for Q-Cells. Shortly before this death in December 2006 he founded the Reiner Lemoine Foundation which offers stipends for Ph.D. candidates in the area of renewable energies. On 20th of August 2008 the German Minister of Environment Sigmar Gabriel inaugurated the Reiner-Lemoine-Research Center at Q-Cells SE." Source: Wikipedia [102]. The author was generously funded by the Reiner Lemoine Foundation for the work on his Diploma and Ph.D. theses. More information about the Reiner Lemoine Foundation and the Reiner Lemoine Institute can be found on their websites [103, 104].

### 6.1 Background

#### 6.1.1 An earlier paper by Dexter

Although not always credited for his idea, Dexter was the first to envision hybrid solar cells which employ strongly absorbing organic dye molecules painted on top of an otherwise poorly absorbing silicon solar cell. In combination the solar cell's absorption is enhanced which in turn yields an improved efficiency [30, 36]. In this scheme light is efficiently absorbed by the organic molecules on the surface of the solar cell from where electronic excitations in the dye molecules can be transferred over short distances to the silicon by means of non-radiative resonance energy transfer. Naturally, the scheme can be extended to more complex configurations where the organic coating contains different interacting species optimised for the absorption of light by the first kind and energy transfer from the second. Exciton diffusion in both the organic material and the semiconductor can possibly increase the effective range of this transfer mechanism from a few to hundreds of nanometres, but this shall not concern us here as the actual value will depend on the specific organic material used. This effect can be added to the simulation at a later stage. The energy transfer mechanism is the same as the one which pumps the QD (or polymer) colour converter deposited onto the different QWs studied in chapters 3, 4 and 5, but here it is employed in the reverse direction. Also, here the donor is a small QD which, to some extent, can be thought of as a point dipole.

#### 6.1.2 Quenching of a dipole in close vicinity of a semiconductor

The underlying mechanism for energy transfer and quenching of a dipole emitter (experimentally realised in a molecule or ion) placed in the vicinity of inorganic materials has been investigated for numerous years before and after Dexter's paper without notice of the particular application in solar cells. This includes metallic, insulating or semiconducting materials and in the case of metals the work lead to an experimental confirmation of the Purcell effect, i.e. the change of the spontaneous emission rate depending on the photon mode density at the position of an emitter [105, 106]. The observed oscillatory modulation of the radiative decay rate of the dipole emitter with increasing distance to a metal surface originates from the constructive/destructive interference between the dipole emission and the field reflected from the metal surface. For very small distances which are smaller than  $\lambda/2$  absorption effects dominate and lead to a steep increase of the decay rate with decreasing separation. The review paper by Agranovich on "Hybrid resonant organic-inorganic nanostructures for optoelectronic applications" points out the works which are historically most relevant in respect to non-radiative energy transfer to a semiconductor slab [35, 107, 108]. These studies focus on the macroscopic treatment of the field produced by a dipole surrounded by medium 1 and placed at distance d to an interface with medium 2. For applications in solar cells

medium 1 is the matrix containing the organic material or the absorbing material itself, and medium 2 is the semiconductor slab. The most important result relates the dipole's radiative decay rate in vacuum,  $\Gamma_{r,vac}$ , to the rate of non-radiative energy transfer into medium 2,  $\Gamma_{nr}$ :

$$\frac{\Gamma_{\rm nr}}{\Gamma_{\rm r,vac}} \approx \left(\frac{\lambda}{2\pi d}\right)^3 \frac{\epsilon_2''}{|\epsilon_1 + \epsilon_2|^2}.\tag{6.1}$$

Here,  $\lambda$  is the wavelength corresponding to the transition and  $\epsilon_i$  refers to the frequency dependent complex dielectric function of the medium i,  $\epsilon_i(\omega) = \epsilon'_i(\omega) + i\epsilon''_i(\omega)$ . The expression for the rate of energy transfer recovers the power law dependence which was given in eq. 2.12 for the interaction between one donor dipole and an array of acceptor dipoles. As expected for tis geometry we find n=3. The first factor in the expression on the right side gives an idea of the order of magnitude for the effectiveness of nonradiative energy transfer over short distances. Consider a dipole with a transition at 2 eV (corresponding to  $\lambda \approx 600$  nm) placed at a distance of 1 nm near medium 2. In this case the factor is on the order of 10<sup>6</sup>. The actual enhancement is smaller than this due to the dielectric screening: typically the denominator  $|\epsilon_1 + \epsilon_2|^2$  is on the order of  $10^2-10^3$ . The absorptive strength  $\epsilon''$  in the semiconductor is also energy dependent and varies greatly between direct and indirect transitions. For silicon  $\epsilon''$  at 2 eV is about 0.17 [109], resulting in an energy transfer rate that is two order of magnitude larger than the radiative decay rate in vacuum. At higher energies, at the offset for direct transitions in silicon around 3.4 eV, the rate of energy transfer to silicon increases by another order of magnitude [110]. It can be seen that a dipole will be strongly quenched near a semiconductor interface and transfer energy non-radiatively to the absorbing medium. However, the expression from eq. 6.1 should be seen only as a crude estimate for the actual energy transfer rate because  $\epsilon(\omega)$  can only successfully describe the medium response for nearly uniform and plane electromagnetic fields. The near-zone field within a few nanometres of the dipole is highly non-uniform and contains a multitude of planar wave vector components, an effect that becomes increasingly important for very small distances. In this case the range of relevant wave vectors  $(\mathbf{k} \approx \frac{1}{d})$  can become substantial in comparison with the Brillouin zone of the absorbing medium and quantitative agreement between experiments and calculations can only be recovered by the use of the wave vector dependent dielectric tensor  $\epsilon(\omega, \mathbf{k})$  [35, 51, 111]. In other words, the optical response described by the dielectric function  $\epsilon(\omega)$  can only account for the excitation of electron-hole pairs in a "vertical" transition between the valence and the conduction band, while the dipolar field in the near-zone can also excite them "non-vertically". For this reason resonance energy transfer promises to be of great use to pump excitations into solar cells made of the indirect band gap semiconductor silicon.

It should be added that beside the macroscopical treatment of the problem another approach exists for the case of a dipole near to a semiconducting half space: Stavola, Dexter and Knox presented a calculation that considers the excitation of electronic transitions near the band edge by the dipole near-field in the effective mass approximation [112].

Their approach distinguishes explicitly between direct and indirect band gap materials. For indirect semiconductors it was found that the phonon-less excitation of the semiconductor by the dipole field of a nearby molecular exciton can be more efficient than the phonon-assisted process. Later, Agranovich concludes in his review: "This effect may make prospects of non-radiative energy transfer into Si substrates even better."

#### 6.1.3 Experimental demonstrations of energy transfer to a semiconductor

The few existing experimental studies on energy transfer from organic materials (or QDs) to a semiconductor will be summarised here before our own results are put into context. Along with the author names also the year of their publications will be given to show how interest in this old idea has been paused for a few decades. Nevertheless, theoretical work on the topic has been published during this time by Agranovich and co-authors. Presumably new fabrication techniques and new ideas for applications were required to justify further experimental investigations. Alivisatos et al. (1983 & 1987) demonstrated energy transfer from thin films of pyridine to GaAs and from pyrene films to an underlying silicon slab [110, 113]. In both studies they used spacer layers of variable thickness to proof that the observed quenching is indeed dependent on the distance to the absorptive semiconductor material. When working with silicon as an acceptor they observed a clear increase of the energy transfer rate at the offset for direct transitions. In their work from 1987 they underline the importance of phonon-less and non-vertical transitions when the dipole emitter comes very close to the semiconductor, in line with the theoretical findings from Stavola, Dexter and Knox (1985) [112]. Gowrishankar et al. (2008) studied another type of hybrid organic-inorganic solar cells where efficient charge separation at the interface between amorphous-silicon (a-Si:H) on one side and MEH-PPV and P3HT on the other side occurs. More importantly for our purposes, they found that this material combination supports very efficient non-radiative energy transfer from the MEH-PPV and P3HT to the amorphous silicon with efficiencies greater than 80% and 30%, respectively. Lu et al. (2007) proved energy transfer from a layer of PbS QDs to an InGaAs QW buried under the surface of a slab of GaAs [114]. This experiment is the analogue to the study from chapter 5 but with a reversed direction of energy transfer. Dr. Soontorn Chanyawadee, my predecessor, and coworkers (2009) were the first to proof that energy transfer pumping of a semiconductor can indeed be utilised to enhance the photocurrent of a photodiode or solar cell [115, 116]. pin-diodes were successfully sensitised by the addition of CdSe/CdS and CdTe QDs. The diodes were specially prepared by the etching of deep vertical channels into their surface by use of a focussed ion beam. Colloidal QDs covering the surface of the etched channels absorb light efficiently and the created electron-hole excitations are then nonradiatively transferred directly into the depletion zone of the diode where the charges can be separated by the built in electric field. Their conclusions about energy transfer were based on the measurement of the photocurrent and time resolved fluorescence of the QDs.

These studies employed pin photodiodes made of a AlGaAs/GaAs QW heterostructure or bulk GaAs and in practice the etching process they used is destructive in nature and not suitable for the preparation of actual devices. More details on the deterioration of the devices during the etching process itself can be found in my Diploma thesis and a corresponding publication [69, 117]. The technologically more relevant material silicon was studied by Lu et al. (2009). They used again PbS QDs to sensitise the absorption of light by a planar array of silicon nano wires and observed the effect of both radiative and non-radiative transfer of excitations from the QDs to the adjacent silicon nano wires. Time-resolved photocurrent measurements indicate a contribution of carrier injection into the silicon from the QDs. A recent study by Nguyen et al. (2011) deals again with silicon as a substrate, sensitised by a layer of CdSe QDs on the surface. In agreement with the older study by Alivisatos on silicon as an acceptor quenching of the donor was observed when the thickness of the spacing layer between the QDs and the silicon was reduced. This study was limited on the spectroscopic characterisation of the energy transfer process. So far, the electrical measurements on energy transfer sensitised photodiodes (solar cells) were performed under illumination with monochromatic laser light, which presumably lead to a larger enhancement as if a broadband spectrum had been used because of resonances in the absorption of the employed QDs. In fact, my previous work from Refs. [69, 117] shows that the power conversion efficiency of the bulk GaAs diodes under illumination with a solar simulator is only marginally enhanced when they are sensitised with QDs. The diodes were treated with the FIB fabrication procedure from Refs. [115, 116].

The careful reader will have noticed that this overview omitted reports where semiconductor colloidal QDs (or, alternatively, organic semiconductors) are employed as energy transfer acceptors in the context of LEDs. This has two reasons: from the physical point of view the problem there is reduced again to an array of dipole-like acceptors because electronic states are not delocalised but strongly bound to individuals sites. Moreover, these works are so close to the main topic of this thesis that they were already summarised in the introduction.

#### 6.1.4 Work towards a sensitised silicon solar cell

After our research group has gained expertise with the design and preparation of sensitised photodiodes it was sought after to produce such a device made of silicon, the most commonly used material for solar cells. For this purpose collaborations with the leading german solar cell manufactorers at that time were initiated. Solarworld AG, Bonn, Germany supplied wafers of amorphous silicon which had been prepared with a shallow lying pn-junction which features a deletion zone within the first 200 nm. It was thought that e-beam lithography or nano imprint lithography in combination with reactive ion etching could be used to produce fine channels similar to the ones in the

Chapter 6 Methods

GaAs photodiodes. In another step electrical contacts would have been added to allow electrical measurements. However, the fabrication facilities and processes available did not allow the manufacturing of such devices.

Another collaboration with Q-Cells AG, Bitterfeld-Wolfen, Germany gave us access to mono crystalline silicon wafers with the doping profile of their commercial solar cells. These wafers yield a power conversion efficiency above 12% when they are equipped with the optimised electrodes from the Q-Cells production line. Delays and faults in the clean room facilities at the Southampton Nanofabrication Centre at the University of Southampton kept delaying the activities on this project and just at the point of writing an internal collaboration is set up to maintain continuous work in the future.

A parallel strand of activities in the research group performed by Mael Brossard covers photoconductivity measurements on silicon substrates equipped with electrodes and PbS QDs on the top. In this configuration enhanced absorption of light by the device due to the layer of strongly absorbing QDs on the surface and subsequent radiative and non-radiative energy transfer of excitations to the silicon can be proved directly by electrical measurements without the need for nanofrabrication processes or fine tuning of the doping profile of the device.

#### 6.2 Methods

#### 6.2.1 Definition of the problem

Due to its simplicity Dexter's idea leaves out many details on the actual implementation of the scheme in real world devices. Some of the questions that have to be considered are: What is the optimum thickness of the sensitising layer (such that it does not absorb too much light without transferring energy to the silicon)? What is the optimum depth of the depletion zone under the surface of the solar cell? What is the critical distance between the sensitising layer and the silicon at which energy transfer brakes down? While all of these questions are equally important for the design of a device, one could argue that the last question serves best as a starting point. The answer will provide an upper boundary for the characteristic layer thicknesses that are expected in a device in order to benefit from energy transfer at all.

The problem that is studied here concerns the rate of energy transfer from a PbS QD (represented as a point dipole) which is lying on top of a silicon slab, separated from the silicon by a silicon oxide (SiO<sub>2</sub>) layer of variable thickness. Figure 6.1 shows a schematic of the geometry. The rate of energy transfer is determined by computing the expressions from eqs. 2.16 and 2.17. This requires knowledge of the dipole near field which is determined by the boundary conditions and material constants of the particular geometry. Note, that this geometry is *not* equivalent with the one leading

Chapter 6 Methods

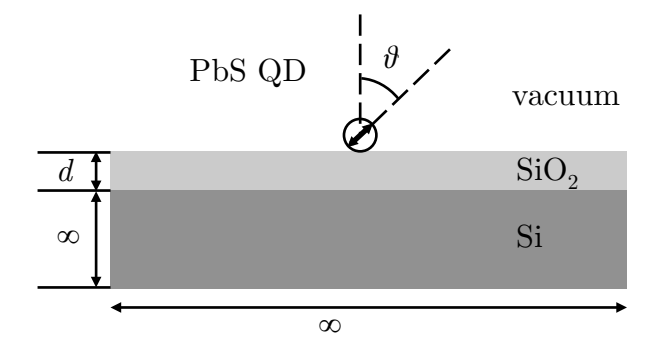


Figure 6.1 – Geometry of the scheme for energy transfer from a PbS QD to a silicon slab. The thickness of the  $SiO_2$  is the variable parameter in the FEM simulation. The simulation requires to average over all possible orientations  $\theta$  of the dipole moment in the QD. The silicon slab extends to infinity. See text for the approximation of infinity in the simulation.

to the expression from eq. 6.1, because of the distinction between the material that separates the dipole and the absorber and the other material that lies above the dipole.

#### 6.2.2 Finite element analysis

The electric field distribution of the dipole is computed numerically by means of finite elements analysis with the software COMSOL. The simulation discretises the spacial dimensions, approximates the derivatives of the electric field numerically and solves the differential equations given by Maxwell's equations and the Poisson equation for the electric field. One of the most common errors when using FEM software is to consider only an insufficiently large volume to approximate infinity. The numerical solution will only be accurate if the fields and potentials decrease to zero far enough from the area of interest, and are not constrained by the particular geometry of the bounding box of the simulation. This was ensured by a) varying the size of the bounding box until a minimum value was found above which the result does not change and b) the actual simulation extends to infinity beyond the size of the bounding box by the use of a geometrical transformation. The simulation presented here does not result in the absolute value of the energy transfer rate from the dipole because the values contain one overall scaling factor to account for the shielding of the dipole field due to the different refractive indices of the QD and its sourrounding. The QD is represented by a point dipole which, by definition, does not have any spacial features. In reality, however, the QD has a diameter of 10 nm, a size that is comparable with the thickness of the silicon oxide spacer layer. In this case it is not sufficient to place the point dipole in the centre of a sphere made of PbS to determine the shielding factor. Although this approach would indeed account for the screening of the electric field due to the high dielectric constant of the sourrounding PbS sphere ( $\epsilon = 17$ ) [118], it constitutes a misleading combination of a microscopic and macroscopic representation of the geometry. If a truly microscopic representation is desired, the actual charge densities would need to be calculated from the different wave functions in the QD. This task is omitted here

for simplicity. In this way Basko et al. have computed analytically the rate of energy transfer for a a geometry with spherical symmetry where a spherical QD is surrounded by a homogeneous absorbing medium [119, 120]. The authors proceed very carefully by considering separately the different excited states in the different confinement regimes. Due to the break of symmetry in our planar arrangements their results cannot be directly applied here.

#### 6.3 Results and discussion

The results from the FEM simulation for the variation of the energy transfer rate with the thickness of the silicon oxide layer are shown in Fig. 6.2. As expected, the energy

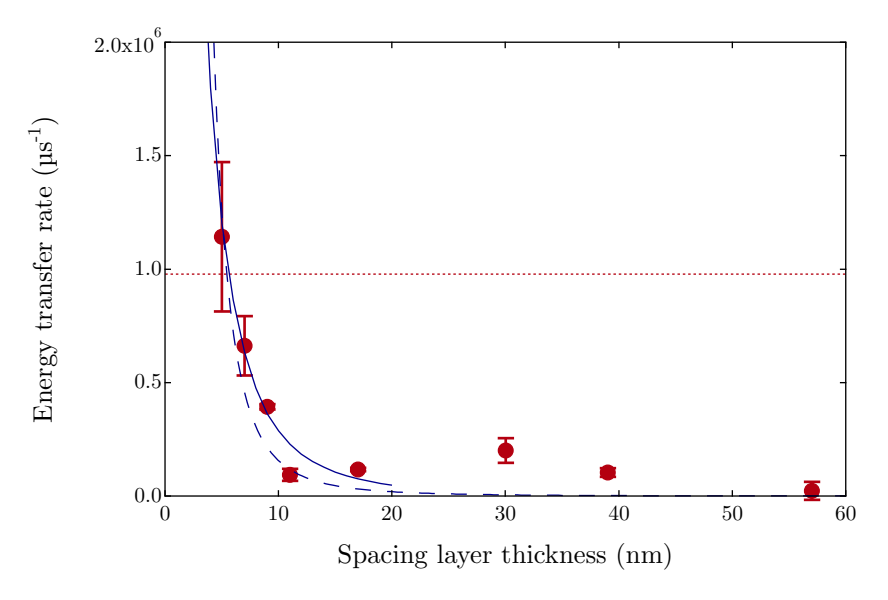


**Figure 6.2** – Simulated energy transfer rate for different thicknesses of the spacing layer (blue solid line). The experimental data from Ref. [80] is also shown (red circles) along with a fit of a power law with n=3 according to eq. 6.1 (blue interrupted line). The horizontal line corresponds to the experimentally determined radiative decay rate of the QDs.

transfer rate drops steeply with increasing spacer thickness and for a thickness above approximately 15 nm it nearly vanishes. This characteristic value corresponds well with experimental data observed by Dr. Peristera Andreakou for the same geometry and material combination [80]. Note, that the blue solid curve in Fig. 6.2 was scaled with an overall scaling factor to provide visual correspondence between the simulated and experimental data. For the experimental study by Andreakou et al. undoped silicon was covered with silicon oxide of various thicknesses between 5 and 55 nm before it was covered with PbS QDs. Time-resolved spectroscopy was performed with a streak camera to quantify the quenching of the lowest lying exciton state in the QD due to non-radiative energy transfer to the underlying silicon slab. The actual uncertainty in the thickness of the spacer layer is unknown and varies with the thickness of the layer. Also, a systematic error is likely because of formation of a native oxide between processing

Chapter 6 Conclusions

steps. Although these error sources are substantial the resulting error bars in the x-direction of the graph are omitted because they are not discussed in the original source of the data [80]. From discussions with the author I learned that the measurements were performed on a QD ensemble which was highly dispersed on the surface. Hence, effects of inter particle interactions can be ruled out and the scenario of an isolated dipole holds true. It is instructive to compare the energy transfer rate with the radiative decay rate, the latter not determined by the FEM simulation, but directly from the experiment. It can be seen from Fig. 6.2 that already for a spacing layer that is only 5.5 nm thick the efficiency of energy transfer is reduced to 50 % in the experiment. The radiative decay rate is determined from a measurement with an "infinitely thick" spacer layer which is around 100 nm thick. Figure 6.2 also shows a fit to the experimental data according to the power law with n=3 from eq. 6.1. In direct comparison, the power law drops faster than the numerically calculated curve. Especially between 8 and 15 nm the power law curve underestimates the energy transfer rate.

#### 6.4 Conclusions

The finite element simulation results in a realistic shape for the distance dependence of energy transfer from a dipole emitter to an absorbing semiconductor half space. It is found that when the thickness of the spacer layer between the dipole and the absorber exceeds 10-15 nm non-radiative energy transfer breaks down. This value is in good agreement with the findings from Refs. [80, 110] where silicon was sensitised with an organic dye or PbS QDs on top of a spacer layer of various thickness. We conclude that the design of a sensitised solar cell requires careful treatment of the surface in order to prevent the suppression of energy transfer in the presence of native oxides, anti reflection coatings or passivating coatings. Only when the donor species is brought into close proximity to the absorber energy can be efficiently transferred by means of nonradiative resonance energy transfer. For a common solar cell made of mono crystalline silicon the depletion zone of the pn-junction lies several hundreds of nanometres deep and excitations will never be injected directly into this zone by non-radiative energy transfer. Nevertheless, materials with a high exciton diffusion coefficient can still benefit from energy transfer pumping as long as they allow diffusion of excitons from the first 10 nm to the the underlying depletion zone. (A very accurate method for the determination of the exciton diffusion coefficient is described in chapter 5). The critical distance of 10 nm has also consequences for the optimum thickness of the sensitising layer: if the material on the top does not allow efficient exciton diffusion within the layer itself, then energy transfer to the silicon will only occur from the first few nanometres of the layer adjacent to the substrate, limiting the effectiveness of the scheme substantially. From the discussion in chapter 2 it can be seen that the strong oscillator strength and absorption found in organic dyes, semiconducting polymers and QDs originates from the Chapter 6 Conclusions

confinement and localisation of carriers in the materials. Naturally, this is contradictory with efficient exciton diffusion, unless the material supports mechanisms for effective exciton migration and hopping between different molecules or polymer segments. The well studied organic semiconductors possess diffusion coefficients of 5-20 nm for singlet excitons [121–126]. For triplet excitons a larger range of values between 10 and more than 100 nm, depending on the material, can be found in the literature [127–129]. The higher diffusion length of the long living triplet states could possibly be employed for this scheme. A few examples exist where the weakened optical transitions in triplet states contribute substantially to the photoluminescence and energy transfer dynamics of a material [130, 131]. The effect of carrier diffusion on the effective range of energy transfer can also be studied with simulation methods and is the logical next step following the basic investigation presented here.



## Conclusions and Future Work

#### 7.1 Conclusions

Within this thesis a range of experiments and theoretical considerations was executed to investigate the conditions for effective resonance energy transfer. The primary system under study consists of excitons in QWs as energy transfer donors and absorptive organic material layers as acceptors. QW excitons posses quantum mechanical properties like a wave vector or the spacial extent of the wave function that give rise to effects beyond the scope of the point dipole approximation that is commonly exerted in the context of resonance energy transfer. For the QW-polyfluorene combination it was also investigated in detail how the rate of energy transfer changes with the distance between the QW and the organic material layer. This material combination bears some potential for the application in LEDs where the rich colours of organic materials render them good candidates as colour converters on top of UV or blue-emitting LED wafers instead of conventional phosphors.

The scheme of energy transfer for colour conversion was tested on blue emitting LED wafers supplied by a LED manufacturer (chapter 3. It was found that the polymer F8BT is an ideal partner for this particular LED to yield high quality white light. Nevertheless, the alterations to the LED design which are required to enable resonance energy transfer to the F8BT are detrimental and outweigh by far the benefit of the more efficient pumping of the colour converter that potentially could be achieved. In conclusion, it seems more viable to be leave the LED design unchanged and embed a sufficiently thick layer of the colour converting material in the same way as it is done for current state of the art white LEDs using either traditional phosphors or QD phosphors. Realistically, for commercial applications where only the output power vs. input electrical power and cost is considered it is not worth to pursue the resonance energy transfer scheme. This was implicitly confirmed by the dying interest of the LED

Chapter 7 Conclusions

manufacturer in the project. Due to the constraints on the availability of the rare earths colour conversion materials like organic semiconductors and colloidal QDs can serve as a cost efficient replacement and are expected to become increasingly important for a large scale introduction of LED lighting [1, 17–26, 32, 33].

One of the reasons why the resonance energy transfer scheme is not commercially attractive for LED manufacturers is the close proximity on the order of only a few nanometres that is required between the QW and the absorptive medium. Evidently, this is incompatible with the need for thick material layers for the injection and spreading of currents of a few hundred mA in a high power LED. From the simulations and experiments in chapter 4 we found that the balance between localised and free exceptions governs the energy transfer dynamics in the technologically important GaN, AlGaN and InGaN material systems. In comparison with other technologically relevant materials like GaAs these materials posses relatively high densities of localised excitons and a high exciton binding energy such that excitons, both localised and free, play a key role at room temperature. We propose a scheme to make use of the high rate of resonance energy transfer for a distinct, resonant wave vector such that energy transfer is enabled over a length scale one order of magnitude longer than the characteristic length scale for the process. The scheme employs fine tuning of the material and interface quality of the heterostructure to achieve the desired fraction and wave vector for free excitons in the exciton ensemble. However, to my judgement this limited degree of freedom is insufficient to enable efficient resonant energy transfer in real world devices and to make them feasible for LED manufacturers.

Not many conclusions can be drawn from the experiments in chapter 5 because after all they did not result in the observation of the desired wave vector dependence of resonance energy transfer. It was thought that in a transient grating experiment energy transfer from a selected wave vector state will enhance the absorption of light by this state so much, that the intensity of the diffracted beam will decrease measurably. However, doe to the fast thermalisation of the exciton ensemble it is not possible to probe the much slower energy transfer processes of one isolated exciton state alone. Instead, within hundreds of fs all excitons interact with each other via direct scattering or phonons which effectively shields the evolution of the selected state from our experiment.

In chapter 6 the result of a computational thought-experiment following the idea of Dexter was presented. A finite element analysis simulation was set up to compute the distance dependence of resonance energy transfer from a PbS QD to a slab of silicon. A layer of silicon oxide with variable thickness was placed between the two, representing any technologically required passivation or anti reflection layers on a real world silicon solar cell. It was observed that the rate of energy transfer drops rather rapidly with increasing spacer thickness such that for a thickness above 10 nm the effect nearly vanishes. This observation matches recently performed experiments on this material

Chapter 7 Future work

combination and I conclude that the scheme is of little use to enhance the efficiency of a real world device [80].

In conclusion, these findings underline that resonance energy transfer is an inherently short ranged mechanism that is not compatible with real world LEDs or solar cells. In inherently thin layered structures, like they are found in planar microcavities, it may provide useful as an efficient pathway for the transfer of excitations between inorganic and organic constituents, orders of magnitude more effective than radiative energy transfer.

#### 7.2 Future work

Future work on resonance energy transfer in QWs will have a focus on the fundamental physics of the process, not applications. For example, different theoretical models exist about the role of free carriers for energy transfer in QWs, but it remains to be seen if, or if they are not, contributing substantially to the transfer of excitations to the acceptor [64, 132]. Also, hybrid inorganic/organic microcavities are predestinated to employ resonance energy transfer and experimental efforts will eventually catch up with the theoretical work on the topic. Beyond QWs, the process is technologically important because it is occurring in blends of organic polymers, dyes and QDs, as they are found for example in organic photovoltaic cells, organic light emitting diodes or in LEDs for colour conversion. In organic polymers energy transfer competes with non-radiative recombination and effectively contributes to exciton diffusion, two effects that need to be understood to achieve efficient organic optoelectronic devices.

## References

- [1] J. J. RINDERMANN, G. POZINA, B. MONEMAR, L. HULTMAN, H. AMANO, and P. G. LAGOUDAKIS, Dependence of resonance energy transfer on exciton dimensionality, *Physical Review Letters* **107**, 236805 (2011).
- [2] J. J. RINDERMANN, G. POZINA, B. MONEMAR, L. HULTMAN, H. AMANO, and P. G. LAGOUDAKIS, The effect of exciton dimensionality on resonance energy transfer: advances for organic color converters in hybrid inorganic/organic LEDs, in: B. WITZIGMANN, M. OSINSKI, F. HENNEBERGER, and Y. ARAKAWA (editors), Proc. SPIE: Physics and Simulation of Optoelectronic Devices XX, volume 8255, 82550I, SPIE-Int. Soc. Optical Engineering, Bellingham, USA (2012).
- [3] S. SOLOMON, D. QIN, M. MANNING, Z. CHEN, M. MARQUIS, K. B. AVERYT, M. TIGNOR, and H. L. MILLER (editors), IPCC, 2007: Climate Change 2007: The Physical Science Basis. Contribution of Working Group I to the Fourth Assessment Report of the Intergovernmental Panel on Climate Change, Cambridge University Press, Cambridge, United Kingdom and New York, N.Y., USA, 1st edition (2007).
- [4] M. L. PARRY, O. F. CANZIANI, J. P. PALUTIKOF, P. J. VAN DER LINDEN, and C. E. HANSON (editors), IPCC, 2007: Climate Change 2007: Impacts, Adaptation and Vulnerability. Contribution of Working Group II to the Fourth Assessment Report of the Intergovernmental Panel on Climate Change, Cambridge University Press, Cambridge, United Kingdom and New York, N.Y., USA, 1st edition (2008).
- [5] B. Metz, O. R. Davidson, P. R. Bosch, R. Dave, and L. Meyer (editors), IPCC, 2007: Climate Change 2007: Mitigation of Climate Change. Contribution of Working Group III to the Fourth Assessment Report of the Intergovernmental Panel on Climate Change, Cambridge University Press, Cambridge, United Kingdom and New York, N.Y., USA, 1st edition (2007).
- [6] C. W. TEAM, R. K. PACHAURI, and A. REISINGER (editors), IPCC, 2007: Climate Change 2007: Synthesis Report. Contribution of Working Groups I, II and III to the Fourth Assessment Report of the Intergovernmental Panel on Climate

- Chance, Intergovernmental Panel on Climate Change, WMO and UNEP, Geneva, Switzerland (2008).
- [7] O. EDENHOFER, R. PICHS-MADRUGA, Y. SOKONA, K. SEYBOTH, S. KADNER, T. ZWICKEL, P. EICKEMEIER, G. HANSEN, S. SCHLÖMER, and C. VON STECHOW, Renewable Energy Sources and Climate Change Mitigation: Special Report of the Intergovernmental Panel on Climate Change, Cambridge University Press, New York, N.Y., USA (2011).
- [8] International Energy Agency, International energy agency statistics, http://www.iea.org/stats/index.asp (2012).
- [9] International Energy Agency, 2010 Key World Energy Statistics, International Energy Agency, Paris, France (2010).
- [10] L. Brown, World on the Edge: How to Prevent Environmental and Economic Collapse, W. W. Norton & Company, New York, N.Y., USA (2011).
- [11] I. NAVIGANT CONSULTING, Energy savings potential of solid-state lighting in general illumination applications, Technical report, US Department of Energy. Office of Energy Efficiency and Renewable Energy. Buildings Technologies Program. Solid-State Lighting Program., Washington, DC, USA (2012).
- [12] E. F. Schubert, Light-Emitting Diodes, Cambridge University Press, New York, N.Y., USA (2006).
- [13] CREE, Cree news: Cree sets new R&D performance record with 254 lumen-per-watt power LED, http://www.cree.com/news-and-events/cree-news/press-releases/2012/april/120412-254-lumen-per-watt (2012).
- [14] E. MILLS, Why we're here: the \$230-billion global lighting energy bill, in: Right Light 5, Proceedings from the 5th European Conference on Energy Efficient Lighting, held in Nice, France, 29–31, The European Council for an Energy Efficient Economy, Stockholm, Sweden (2002).
- [15] Semiconductor Today, Packaged LED market to grow from \$11.4bn in 2012 to \$17.1bn in 2018, http://www.semiconductortoday.com/news\_items/2012/AUG/LED\_090812.html (2012).
- [16] Strategies Unlimited, Worldwide LED market grew 9.8% to \$12.5 billion in 2011 with 44% growth in LED lighting according to strategies unlimited, http://www.strategies-u.com/articles/2012/02/worldwide-led-market-grew-98-to-125-billion-in-2011-with-44-growth-in-led-lighting-according-to-strategies-unlimited.html (2012).
- [17] S. PIMPUTKAR, J. S. SPECK, S. P. DENBAARS, and S. NAKAMURA, Prospects for LED lighting, Nature Photonics 3, 180 (2009).

- [18] EDITORIAL, The new oil?, Nature Photonics 5, 1 (2011).
- [19] T. Erdem and H. V. Demir, Semiconductor nanocrystals as rare-earth alternatives, *Nature Photonics* 5, 126 (2011).
- [20] G. Itskos, G. Heliotis, P. Lagoudakis, J. Lupton, N. Barradas, E. Alves, S. Pereira, I. Watson, M. Dawson, J. Feldmann, R. Murray, and D. Bradley, Efficient dipole-dipole coupling of mott-wannier and frenkel excitons in (Ga,In)N quantum well/polyfluorene semiconductor heterostructures, *Physical Review B* 76, 035344 (2007).
- [21] S. CHANYAWADEE, P. G. LAGOUDAKIS, R. T. HARLEY, M. D. B. CHARLTON, D. V. TALAPIN, H. W. HUANG, and C.-H. LIN, Increased color-conversion efficiency in hybrid light-emitting diodes utilizing non-radiative energy transfer, Advanced Materials 22, 602 (2010).
- [22] C. R. Belton, G. Itskos, G. Heliotis, P. N. Stavrinou, P. G. Lagoudakis, J. Lupton, S. Pereira, E. Gu, C. Griffin, B. Guilhabert, I. M. Watson, A. R. Mackintosh, R. A. Pethrick, J. Feldmann, R. Murray, M. D. Dawson, and D. D. C. Bradley, New light from hybrid inorganic-organic emitters, Journal of Physics D: Applied Physics 41, 094006 (2008).
- [23] G. Itskos, C. R. Belton, G. Heliotis, I. M. Watson, M. D. Dawson, R. Murray, and D. D. C. Bradley, White light emission via cascade förster energy transfer in (Ga,In)N quantum well/polymer blend hybrid structures, *Nanotechnology* **20**, 275207 (2009).
- [24] M. Achermann, M. A. Petruska, S. Kos, D. L. Smith, D. D. Koleske, and V. I. Klimov, Energy-transfer pumping of semiconductor nanocrystals using an epitaxial quantum well, *Nature* **429**, 642–646 (2004).
- [25] M. Achermann, M. A. Petruska, D. D. Koleske, M. H. Crawford, and V. I. Klimov, Nanocrystal-based light-emitting diodes utilizing high-efficiency nonradiative energy transfer for color conversion, *Nano Letters* 6, 1396 (2006).
- [26] H. V. Demir, S. Nizamoglu, T. Erdem, E. Mutlugun, N. Gaponik, and A. Eychmüller, Quantum dot integrated LEDs using photonic and excitonic color conversion, *Nano Today* **6**, 632 (2011).
- [27] V. AGRANOVICH, R. ATANASOV, and F. BASSANI, Hybrid interface excitons in organic-inorganic quantum wells, Solid State Communications 92, 295 (1994).
- [28] V. AGRANOVICH, G. LA ROCCA, and F. BASSANI, Efficient electronic energy transfer from a semiconductor quantum well to an organic material, Journal of Experimental and Theoretical Physics Letters 66, 748 (1997).

[29] D. BASKO, G. C. LA ROCCA, F. BASSANI, and V. M. AGRANOVICH, Förster energy transfer from a semiconductor quantum well to an organic material overlayer, The European Physical Journal B-Condensed Matter and Complex Systems 8, 353 (1999).

- [30] V. Agranovich, D. Basko, G. La Rocca, and F. Bassani, New concept for organic LEDs: non-radiative electronic energy transfer from semiconductor quantum well to organic overlayer, *Synthetic Metals* **116**, 349 (2001).
- [31] D. BASKO, V. AGRANOVICH, and G. BASSANI, Energy transfer from a semiconductor nanostructure to an organic material and a new concept for light-emitting devices, in: Electronic Excitations in Organic Nanostructures, volume 31, 447, Academic Press (2003).
- [32] S. Blumstengel, S. Sadofev, C. Xu, J. Puls, and F. Henneberger, Converting wannier into frenkel excitons in an inorganic/organic hybrid semiconductor nanostructure, *Physical Review Letters* 97 (2006).
- [33] S. Blumstengel, S. Sadofev, J. Puls, and F. Henneberger, An inorgan-ic/organic semiconductor "Sandwich" structure grown by molecular beam epitaxy, *Advanced Materials* **21**, 4850 (2009).
- [34] Q. Zhang, T. Atay, J. R. Tischler, M. S. Bradley, V. Bulović, and A. V. Nurmikko, Highly efficient resonant coupling of optical excitations in hybrid organic/inorganic semiconductor nanostructures, *Nature Nanotechnology* 2, 555 (2007).
- [35] V. M. AGRANOVICH, Y. N. GARTSTEIN, and M. LITINSKAYA, Hybrid resonant organic—inorganic nanostructures for optoelectronic applications, *Chemical Reviews* 111, 5179 (2011).
- [36] D. Dexter, Two ideas on energy transfer phenomena: Ion-pair effects involving the OH stretching mode, and sensitization of photovoltaic cells, *Journal of Luminescence* 18-19, 779 (1979).
- [37] E. ROSENCHER and B. VINTER, Optoelectronics, Cambridge University Press, Cambridge, UK (2002).
- [38] C. KITTEL, Introduction to Solid State Physics, John Wiley & Sons, 8th edition (2004).
- [39] G. Bastard, Wave mechanics applied to semiconductor heterostructures, Les Éditions de Physique (1988).
- [40] E. Kane, Band structure of indium antimonide, Journal of Physics and Chemistry of Solids 1, 249 (1957).

- [41] S. M. Sze, Physics of Semiconductor Devices, Wiley Eastern Limited (1981).
- [42] G. H. Wannier, The structure of electronic excitation levels in insulating crystals, *Physical Review* **52**, 191 (1937).
- [43] P. Harrison, Quantum Wells, Wires and Dots: Theoretical and Computational Physics of Semiconductor Nanostructures, John Wiley & Sons (2011).
- [44] J. Frenkel, On the transformation of light into heat in solids. I, *Physical Review* 37, 17 (1931).
- [45] D. L. Dexter, A theory of sensitized luminescence in solids, *The Journal of Chemical Physics* **21**, 836 (1953).
- [46] T. FÖRSTER, Energiewanderung und Fluoreszenz, Die Naturwissenschaften 33, 166 (1946).
- [47] T. FÖRSTER, Zwischenmolekulare Energiewanderung und Fluoreszenz, Annalen der Physik 437, 55–75 (1948).
- [48] H. Kuhn, Classical aspects of energy transfer in molecular systems, *The Journal of Chemical Physics* **53**, 101 (1970).
- [49] M. Lunz, A. Bradley, V. Gerard, S. Byrne, Y. Gun'ko, V. Lesnyak, and N. Gaponik, Concentration dependence of förster resonant energy transfer between donor and acceptor nanocrystal quantum dot layers: Effect of donor-donor interactions, *Physical Review B* 83 (2011).
- [50] H. Haug and S. W. Koch, Quantum Theory of the Optical and Electronic Properties of Semiconductors, World Scientific (2004).
- [51] L. D. LANDAU, E. M. LIFSHITZ, and L. P. PITAESVSKII, Electrodynamics of continuous media, Butterworth-Heinemann, 2nd edition (1984).
- [52] W. Shockley and H. J. Queisser, Detailed balance limit of efficiency of p-n junction solar cells, *Journal of Applied Physics* **32**, 510 (1961).
- [53] NATIONAL RENEWABLE ENERGY LABORATORY, NATIONAL CENTER FOR PHOTOVLOTAICS, NREL: national center for photovoltaics home page, http://www.nrel.gov/ncpv/ (2012).
- [54] M. GRAETZEL, R. A. J. JANSSEN, D. B. MITZI, and E. H. SARGENT, Materials interface engineering for solution-processed photovoltaics, *Nature* 488, 304 (2012).
- [55] H. A. ATWATER and A. POLMAN, Plasmonics for improved photovoltaic devices, Nature Materials 9, 205 (2010).

[56] S. Chanyawadee, Resonant Energy Transfer in Light Harvesting and Light Emitting Applications, Ph.D. thesis, University of Southampton, Southampton, UK (2009).

- [57] A. Z. Khokhar, K. Parsons, G. Hubbard, F. Rahman, D. S. Macintyre, C. Xiong, D. Massoubre, Z. Gong, N. P. Johnson, R. M. D. L. Rue, I. M. Watson, E. Gu, M. D. Dawson, S. J. Abbott, M. D. Charlton, and M. Tillin, Nanofabrication of gallium nitride photonic crystal light-emitting diodes, *Microelectronic Engineering* 87, 2200 (2010).
- [58] A. Z. Khokhar, K. Parsons, G. Hubbard, I. M. Watson, F. Rahman, D. S. Macintyre, C. Xiong, D. Massoubre, Z. Gong, E. Gu, N. P. Johnson, R. M. De La Rue, M. D. Dawson, S. J. Abbott, M. D. B. Charlton, and M. Tillin, Emission characteristics of photonic crystal light-emitting diodes, *Applied Optics* 50, 3233 (2011).
- [59] J. J. RINDERMANN, Y. AKHTMAN, J. RICHARDSON, T. BROWN, and P. G. LAGOUDAKIS, Gauging the flexibility of fluorescent markers for the interpretation of fluorescence resonance energy transfer, Journal of the American Chemical Society 133, 279 (2011).
- [60] J. Baumberg, A. Kavokin, S. Christopoulos, A. Grundy, R. Butté, G. Christmann, D. Solnyshkov, G. Malpuech, G. Baldassarri Höger von Högersthal, E. Feltin, J.-F. Carlin, and N. Grandjean, Spontaneous polarization buildup in a room-temperature polariton laser, *Physical Review Letters* 101 (2008).
- [61] A. VELTEN, T. WILLWACHER, O. GUPTA, A. VEERARAGHAVAN, M. G. BAWENDI, and R. RASKAR, Recovering three-dimensional shape around a corner using ultrafast time-of-flight imaging, *Nature Communications* 3, 745 (2012).
- [62] Y. C. Shen, G. O. Mueller, S. Watanabe, N. F. Gardner, A. Munkholm, and M. R. Krames, Auger recombination in InGaN measured by photoluminescence, Applied Physics Letters 91, 141101 (2007).
- [63] M. Zhang, P. Bhattacharya, J. Singh, and J. Hinckley, Direct measurement of auger recombination in InGaN/GaN quantum wells and its impact on the efficiency of InGaN/GaN multiple quantum well light emitting diodes, Applied Physics Letters 95, 201108 (2009).
- [64] Y. GLADUSH, C. PIERMAROCCHI, and V. AGRANOVICH, Dynamics of excitons and free carriers in hybrid organic-inorganic quantum well structures, *Physical Review* B 84, 205312 (2011).
- [65] M.-H. Kim, M. F. Schubert, Q. Dai, J. K. Kim, E. F. Schubert, J. Piprek, and Y. Park, Origin of efficiency droop in GaN-based light-emitting diodes, *Applied Physics Letters* 91, 183507 (2007).

[66] S. Hammersley, D. Watson-Parris, P. Dawson, M. J. Godfrey, T. J. Bad-Cock, M. J. Kappers, C. McAleese, R. A. Oliver, and C. J. Humphreys, The consequences of high injected carrier densities on carrier localization and efficiency droop in InGaN/GaN quantum well structures, *Journal of Applied Physics* 111, 083512 (2012).

- [67] A. CADBY, R. DEAN, R. a. L. JONES, and D. G. LIDZEY, Suppression of energy-transfer between conjugated polymers in a ternary blend identified using scanning near-field optical microscopy, Advanced Materials 18, 2713 (2006).
- [68] S. CHANYAWADEE, P. LAGOUDAKIS, R. T. HARLEY, D. LIDZEY, and M. HENINI, Nonradiative exciton energy transfer in hybrid organic-inorganic heterostructures, *Physical Review B* 77 (2008).
- [69] J. J. RINDERMANN, Resonant Energy Transfer in Nanostructures, Diploma thesis, Universität Hamburg, Hamburg, Germany (2009).
- [70] M. Ariu, M. Sims, M. Rahn, J. Hill, A. Fox, D. Lidzey, M. Oda, J. Cabanillas-Gonzalez, and D. Bradley, Exciton migration in beta-phase poly(9,9-dioctylfluorene), *Physical Review B* **67** (2003).
- [71] V. M. AGRANOVICH, G. C. LA ROCCA, F. BASSANI, H. BENISTY, and C. WEISBUCH, Hybrid frenkel-wannier-mott excitons at interfaces and in microcavities, *Optical Materials* **9**, 430–436 (1998).
- [72] S. Rohrmoser, J. Baldauf, R. T. Harley, P. G. Lagoudakis, S. Sapra, A. Eychmu?ller, and I. M. Watson, Temperature dependence of exciton transfer in hybrid quantum well/nanocrystal heterostructures, *Applied Physics Letters* **91**, 092126 (2007).
- [73] D. Basko, G. La Rocca, F. Bassani, and V. Agranovich, Interaction of quantum well excitons with a resonant localized excitation, *Physical Review B* **71** (2005).
- [74] I. VURGAFTMAN, J. R. MEYER, and L. R. RAM-MOHAN, Band parameters for III-V compound semiconductors and their alloys, *Journal of Applied Physics* 89, 5815 (2001).
- [75] G. TRAETTA, R. CINGOLANI, A. DI CARLO, F. DELLA SALA, and P. LUGLI, Many-body effects on excitons properties in GaN/AlGaN quantum wells, Applied Physics Letters 76, 1042 (2000).
- [76] M. GALLART, A. MOREL, T. TALIERCIO, P. LEFEBVRE, B. GIL, J. ALLÈGRE, H. MATHIEU, N. GRANDJEAN, M. LEROUX, and J. MASSIES, Scale effects on exciton localization and nonradiative processes in GaN/AlGaN quantum wells, *Physica Status Solidi (a)* 180, 127 (2000).

[77] C. M. RAMSDALE and N. C. GREENHAM, The optical constants of emitter and electrode materials in polymer light-emitting diodes, *Journal of Physics D: Applied Physics* **36**, L29 (2003).

- [78] S. KAWKA and G. LA ROCCA, Role of anisotropy in the förster energy transfer from a semiconductor quantum well to an organic crystalline overlayer, *Physical Review B* **85** (2012).
- [79] V. Agranovich, H. Benisty, and C. Weisbuch, Organic and inorganic quantum wells in a microcavity: Frenkel-wannier-mott excitons hybridization and energy transformation, *Solid State Communications* **102**, 631 (1997).
- [80] P. Andreakou, Hybrid Nanomaterials for Novel Photonic Devices, PhD thesis, University of Southampton, Southampton, UK (2012).
- [81] M. Hines and G. Scholes, Colloidal PbS nanocrystals with size-tunable near-infrared emission: Observation of post-synthesis self-narrowing of the particle size distribution, *Advanced Materials* **15**, 1844 (2003).
- [82] D. A. B. MILLER, Degenerate four-wave mixing in room-temperature GaAs/-GaAlAs multiple quantum well structures, *Applied Physics Letters* **42**, 925 (1983).
- [83] L. SCHULTHEIS, J. KUHL, A. HONOLD, and C. W. Tu, Picosecond phase coherence and orientational relaxation of excitons in GaAs, *Physical Review Letters* 57, 1797 (1986).
- [84] L. Schultheis, A. Honold, J. Kuhl, K. Köhler, and C. W. Tu, Optical dephasing of homogeneously broadened two-dimensional exciton transitions in GaAs quantum wells, *Physical Review B* **34**, 9027 (1986).
- [85] L. Schultheis, J. Kuhl, A. Honold, and C. W. Tu, Ultrafast phase relaxation of excitons via exciton-exciton and exciton-electron collisions, *Physical Review Letters* 57, 1635 (1986).
- [86] A. HONOLD, L. SCHULTHEIS, J. KUHL, and C. W. Tu, Reflected degenerate fourwave mixing on GaAs single quantum wells, Applied Physics Letters 52, 2105 (1988).
- [87] R. Manning, D. Crust, D. Craig, A. Miller, and K. Woodbridge, Transient-grating studies in GaAs/GaAlAs multiple quantum wells, *Journal of Modern Optics* **35**, 541 (1988).
- [88] A. MILLER, R. J. MANNING, P. K. MILSOM, D. C. HUTCHINGS, K. WOODBRIDGE, ET AL., Transient grating studies of excitonic optical nonlinearities in GaAs/Al-GaAs multiple-quantum-well structures, *Journal of the Optical Society of America B* 6, 567 (1989).

[89] A. HONOLD, L. SCHULTHEIS, J. KUHL, and C. W. Tu, Collision broadening of two-dimensional excitons in a GaAs single quantum well, *Physical Review B* 40, 6442 (1989).

- [90] K. Leo, T. C. Damen, J. Shah, E. O. Göbel, and K. Köhler, Quantum beats of light hole and heavy hole excitons in quantum wells, *Applied Physics Letters* 57, 19 (1990).
- [91] K. Leo, J. Shah, E. O. Göbel, T. C. Damen, K. Köhler, and P. Ganser, Tunneling in semiconductor heterostructures studied by subpicosecond four-wave mixing, *Applied Physics Letters* **56**, 2031 (1990).
- [92] K. Leo, E. O. Göbel, T. C. Damen, J. Shah, S. Schmitt-Rink, W. Schäfer, J. F. Müller, K. Köhler, and P. Ganser, Subpicosecond four-wave mixing in GaAs/AlGaAs quantum wells, *Physical Review B* 44, 5726 (1991).
- [93] K. Leo, J. Shah, E. O. Göbel, T. C. Damen, S. Schmitt-Rink, W. Schäfer, and K. Köhler, Coherent oscillations of a wave packet in a semiconductor double-quantum-well structure, *Physical Review Letters* **66**, 201 (1991).
- [94] A. R. CAMERON, P. RIBLET, and A. MILLER, Spin gratings and the measurement of electron drift mobility in multiple quantum well semiconductors, *Physical Review Letters* 76, 4793 (1996).
- [95] J. DAVIS, J. WATHEN, V. BLANCHET, and R. PHILLIPS, Time-resolved four-wavemixing spectroscopy of excitons in a single quantum well, *Physical Review B* 75, 035317 (2007).
- [96] W. J. H. LEYLAND, Spin Transport and Relaxation in Semiconductor Heterostructures, PhD thesis, University of Cambridge, Cambridge, UK (2007).
- [97] P. ELDRIDGE, W. LEYLAND, P. LAGOUDAKIS, O. KARIMOV, M. HENINI, D. TAYLOR, R. PHILLIPS, and R. T. HARLEY, All-optical measurement of rashba coefficient in quantum wells, *Physical Review B* 77 (2008).
- [98] E. Kammann, On the Dynamics of Spinor Condensates in Microcavities, Ph.D. thesis, University of Southampton, Southampton, UK (2012).
- [99] E. KAMMANN, H. OHADI, M. MARAGKOU, A. V. KAVOKIN, and P. G. LAGOUDAKIS, Crossover from photon to exciton-polariton lasing, New Journal of Physics 14, 105003 (2012).
- [100] J. Feldmann, G. Peter, E. O. Göbel, P. Dawson, K. Moore, C. Foxon, and R. J. Elliott, Linewidth dependence of radiative exciton lifetimes in quantum wells, *Physical review letters* **59**, 2337 (1987).

[101] B. A. RUZICKA, L. K. WERAKE, H. SAMASSEKOU, and H. ZHAO, Ambipolar diffusion of photoexcited carriers in bulk GaAs, Applied Physics Letters 97, 262119 (2010).

- [102] WIKIPEDIA, Reiner Lemoine (2012), page Version ID: 279633443.
- [103] REINER LEMOINE INSTITUT, Reiner Lemoine Institut. Wir forschen an Lösungen zum Einsatz Erneuerbarer Energie, http://www.reiner-lemoine-institut.de (2012).
- [104] Reiner Lemoine Stiftung, Reiner Lemoine Stiftung, http://www.reiner-lemoine-stiftung.de/ (2012).
- [105] E. M. Purcell, Spontaneous emission probabilities at radio frequencies, *Physical Review* 69, 681 (1946).
- [106] K. Drexhage, Influence of a dielectric interface on fluorescence decay time, *Journal of Luminescence* **1–2**, 693 (1970).
- [107] R. R. CHANCE, A. PROCK, and R. SILBEY, Molecular fluorescence and energy transfer near interfaces, in: I. PRIGOGINE and S. A. RICE (editors), Advances in Chemical Physics, 1–65, John Wiley & Sons, Inc. (2007).
- [108] L. NOVOTNY and B. HECHT, Principles of Nano-Optics, Cambridge University Press, Cambridge, UK (2006).
- [109] D. E. ASPNES and A. A. STUDNA, Dielectric functions and optical parameters of Si, Ge, GaP, GaAs, GaSb, InP, InAs, and InSb from 1.5 to 6.0 eV, *Physical Review B* 27, 985 (1983).
- [110] A. P. ALIVISATOS, M. F. ARNDT, S. EFRIMA, D. H. WALDECK, and C. B. HARRIS, Electronic energy transfer at semiconductor interfaces. I. Energy transfer from twodimensional molecular films to Si(111), The Journal of Chemical Physics 86, 6540 (1987).
- [111] V. M. AGRANOVICH and V. L. GINZBURG, Crystal optics with spatial dispersion, and excitons, Springer-Verlag (1984).
- [112] M. STAVOLA, D. L. DEXTER, and R. S. KNOX, Electron-hole pair excitation in semiconductors via energy transfer from an external sensitizer, *Physical Review B* 31, 2277 (1985).
- [113] P. M. Whitmore, A. P. Alivisatos, and C. B. Harris, Distance dependence of electronic energy transfer to semiconductor surfaces: 3n pi\* pyrazine/GaAs(110), *Physical Review Letters* **50**, 1092 (1983).
- [114] S. Lu and A. Madhukar, Nonradiative resonant excitation transfer from nanocrystal quantum dots to adjacent quantum channels, *Nano Letters* 7, 3443 (2007).

[115] S. Chanyawadee, R. Harley, M. Henini, D. Talapin, and P. Lagoudakis, Photocurrent enhancement in hybrid nanocrystal quantum-dot p-i-n photovoltaic devices, *Physical Review Letters* **102** (2009).

- [116] S. CHANYAWADEE, R. T. HARLEY, D. TAYLOR, M. HENINI, A. S. SUSHA, A. L. ROGACH, and P. G. LAGOUDAKIS, Efficient light harvesting in hybrid CdTe nanocrystal/bulk GaAs p-i-n photovoltaic devices, *Applied Physics Letters* **94**, 233502 (2009).
- [117] J. J. RINDERMANN, M. HENINI, and P. G. LAGOUDAKIS, In-situ electrical characterisation of a photodiode during nano-structuring with a focussed ion beam, *Applied Physics A* **110**, 935 (2012).
- [118] B. L. Wehrenberg, C. Wang, and P. Guyot-Sionnest, Interband and intraband optical studies of PbSe colloidal quantum dots, *The Journal of Physical Chemistry B* **106**, 10634 (2002).
- [119] V. M. AGRANOVICH and D. M. BASKO, Resonance energy transfer from a semiconductor quantum dot to an organic matrix, *Journal of Experimental and Theoretical Physics Letters* **69**, 250 (1999).
- [120] D. M. BASKO, V. M. AGRANOVICH, F. BASSANI, and G. C. L. ROCCA, Energy transfer from a semiconductor quantum dot to an organic matrix, *The European Physical Journal B-Condensed Matter and Complex Systems* 13, 653 (2000).
- [121] D. E. MARKOV and P. W. M. BLOM, Exciton quenching in poly(phenylene vinylene) polymer light-emitting diodes, *Applied Physics Letters* 87, 233511 (2005).
- [122] Y. Terao, H. Sasabe, and C. Adachi, Correlation of hole mobility, exciton diffusion length, and solar cell characteristics in phthalocyanine/fullerene organic solar cells, *Applied Physics Letters* **90**, 103515 (2007).
- [123] P. E. Shaw, A. Ruseckas, and I. D. W. Samuel, Exciton diffusion measurements in poly(3-hexylthiophene), Advanced Materials 20, 3516–3520 (2008).
- [124] O. V. MIKHNENKO, F. CORDELLA, A. B. SIEVAL, J. C. HUMMELEN, P. W. M. BLOM, and M. A. LOI, Temperature dependence of exciton diffusion in conjugated polymers, *The Journal of Physical Chemistry B* **112**, 11601 (2008).
- [125] R. R. Lunt, J. B. Benziger, and S. R. Forrest, Relationship between crystalline order and exciton diffusion length in molecular organic semiconductors, *Advanced Materials* 22, 1233 (2010).
- [126] W. A. Luhman and R. J. Holmes, Investigation of energy transfer in organic photovoltaic cells and impact on exciton diffusion length measurements, *Advanced Functional Materials* **21**, 764 (2011).

[127] M. A. Baldo, D. F. O'Brien, M. E. Thompson, and S. R. Forrest, Excitonic singlet-triplet ratio in a semiconducting organic thin film, *Physical Review B* **60**, 14422 (1999).

- [128] M. Samiullah, D. Moghe, U. Scherf, and S. Guha, Diffusion length of triplet excitons in organic semiconductors, *Physical Review B* 82 (2010).
- [129] H. NAJAFOV, B. LEE, Q. ZHOU, L. C. FELDMAN, and V. PODZOROV, Observation of long-range exciton diffusion in highly ordered organic semiconductors, *Nature Materials* **9**, 938 (2010).
- [130] M. A. Baldo, D. F. O'Brien, Y. You, A. Shoustikov, S. Sibley, M. E. Thompson, and S. R. Forrest, Highly efficient phosphorescent emission from organic electroluminescent devices, *Nature* **395**, 151 (1998).
- [131] V. CLEAVE, G. YAHIOGLU, P. L. BARNY, R. H. FRIEND, and N. TESSLER, Harvesting singlet and triplet energy in polymer LEDs, *Advanced Materials* **11**, 285 (1999).
- [132] S. Kos, M. Achermann, V. Klimov, and D. Smith, Different regimes of förstertype energy transfer between an epitaxial quantum well and a proximal monolayer of semiconductor nanocrystals, *Physical Review B* **71**, 205309 (2005).